Measuring Dynamic Changes in Lung Water Density and Volume Following Supine Body Positioning Using Free-Breathing UTE MRI

by

David Thomas Goodhart

A thesis submitted in partial fulfillment of the requirements for the degree of

Master of Science

Department of Biomedical Engineering

University of Alberta

© David Thomas Goodhart, 2024

Abstract

An excess of extravascular lung water (EVLW) is known as pulmonary edema, and is associated with dyspnea and poor exercise capacity, heart complications, heart failure, and can be a predictor of poor health outcomes. Recent developments in magnetic resonance imaging (MRI) sequencing and hardware capabilities have enabled free-breathing, 3D isotropic images of the lungs. Previous studies have developed methods to overcome the inherent difficulties in lung MRI, which include low SNR, high signal variations across the image space due to B1 field inhomogeneity, artifacts caused by respiratory and cardiac motion, and a need to normalize signal units within the lung parenchyma to units of lung water content. Through these methods, lung water density (LWD) has been shown to be roughly ~25%-30% in healthy subjects, with a well-documented gradient in LWD in the chest-to-back direction (otherwise known as the "Slinky Effect"). Standard MRI protocol calls for a subject to assume a supine position, which has substantial changes to the thoracic cavity; Changes in global LWD, regional LWD, and global lung volumes over time after assuming supine positioning remain relatively unknown.

This thesis has two goals: 1. Refining and improving upon a previously established Free-Breathing "Yarnball" ultrashort echo time (UTE) non-Cartesian k-space trajectory via maximizing trajectory efficiency (balancing image quality and scan time) and introducing a nnU-Net neural network approach to lung parenchyma and lung vasculature segmentation for increased accuracy in relative LWD (rLWD) calculation and 2. Performing a long-time course series (~25 minutes) of lung MRI scans using the above refined trajectory to establish the time-course changes in global rLWD, regional rLWD, global water content and global lung volumes

that occur due to a physiological response triggered by a change in the direction of gravitational forces acting upon the body when supine positioning is assumed. If possible, establishment of the amount of time it takes for the noted “Slinky Effect” to form is a tertiary goal.

The UTE Yarnball k-space trajectory developed by Meadus et al (2021) was optimized by adjusting the key variables of readout time, TR, voxel size, FOV, and number of averages acquired with image quality, image quantification and total imaging time being taken into consideration. It was determined that a sequence with: FOV = 350 mm, TR = 2.72 ms, TE = 100 μs, 1-degree flip angle, readout time = 1.3 ms, Voxel size = 3.5 mm in all directions, 10 averages and 2738 k-space trajectories was most optimal.

At the respiratory phase of functional residual capacity (FRC), minimum lung volume with normal tidal breathing, it was found that global rLWD increased significantly (31.8±5.5% to 34.8±6.8%, $p=0.001$), global lung volumes decreased significantly (2390±620mL to 2130±630mL, $p<0.001$) and total lung water volume decreased slightly (730±125 mL to 706±126 mL, $p=0.028$) over a 25-minute period after supine positioning was assumed. The chest-to-back gradient (20.7±4.6% at the chest to 39.9±6.1% at the back) formed prior to first acquisition (~3:54 minutes), and was significant at all time-points. Tidal volume (lung volume change per respiratory cycle) also decreased significantly over time (474±89mL to 382±91 mL, $p=0.018$) despite respiratory rate remaining constant.

UTE Yarnball MRI was refined to “optimally” balance image quality with total image scan time, featuring an increase in number of averages used alongside a reduction in scan time

with no significant loss to image quality when compared to the preceding iteration. Global and regional rLWD and lung volumes were shown to change over long periods of time after supine positioning, a phenomenon that should be considered in future lung MRI studies. In particular, we have shown, for the first time, that the timing of data acquisition following supine positioning will significantly affect the lung water density values, and thus should be taken into consideration in clinical studies. Furthermore, any free-breathing MRI acquisitions should consider these significant shifts in lung volumes and positions over time following supine positioning (i.e. navigator type sequences would be confounded by the potential drift of lungs, heart and all organs in abdomen over time). Finally, the formation of the chest-to-back gradient was not captured, but can be inferred to occur in < 1 minute, and likely immediately with supine positioning.

Preface

This thesis is an original work by Thomas David Goodhart. This project received ethics approval from the University of Alberta Ethics Board (Changes in MRI-derived lung water content with physiologic challenge, Pro00107997).

Acknowledgments

I would like to express my gratitude to my supervisor for this project, Dr. Richard Thompson, who provided me with constant support, feedback and encouragement throughout this project. The knowledge and expertise he provided proved to be invaluable in the completion of the project. I would also like to thank Dr. Rob Stobbe, Justin Grenier and Peter Seres for their support and expertise regarding Yarnball implementation, troubleshooting and optimization. Thank you to my supervisory committee (Dr. Richard Thompson, Dr. Rob Stobbe, Dr. Alan Wilman) for their advice and feedback.

This research could not have been completed without the financial support provided by the department of Biomedical Engineering, the University of Alberta and the Faculty of Graduate Studies and Research at the University of Alberta. An additional thanks to the Faculty of Graduate Studies and Research for additional traveling financial aid.

Lastly, I would like to extend my gratitude to the friends and family who offered support throughout the duration of this project.

Contents

List of Tables

List of Figures

List of Abbreviations

ABB	Air-Blood Barrier
ARDS	Acute Respiratory Distress Syndrome
CT	Computed Tomography
FOV	Field of View
FRC	Functional Residual Capacity
FRC+TV	Functional Residual Capacity + Tidal Volume
GRE	Gradient Echo
HASTE	Half Fourier Acquisition Single-Shot Turbo Spin Echo
HF	Heart Failure
L	Liters
LWD	Lung Water Density
mL	milliLiters
MRI	Magnetic Resonance Imaging
PE	Pulmonary Edema

RF	Radio-Frequency
rLWD	Relative Lung Water Density
SNR	Signal-to-Noise ratio
SPGR	Spoiled Gradient Echo
T	Tesla
TE	Echo Time
TR	Repetition Time
TSE	Turbo-Spin Echo
TV	Tidal Volume
T1	Longitudinal Relaxation Time
T2	Transverse Relaxation Time
T2*	Observed Transverse Relaxation Time
UTE	Ultra-short Echo Time
YB	Yarnbal

Chapter 1: Introduction

1.1 Thesis Background and Motivation

Measurement of lung water content and lung water density (LWD) has seen increased interest due to elevated LWD being shown to be predictive of health outcomes in pulmonary edema and heart failure[1–4]. Recent advancements in magnetic resonance imaging (MRI) sequencing and hardware capabilities have allowed for 3D isotropic imaging of the lungs, capable of quantifying LWD[5–7]. It has been well established using MRI that there is a distinct chest-to-back gradient in LWD that forms sometime after a subject assumes supine positioning; however, the exact time course of changes that occur within the lungs has yet to be studied[5–7]. Given that a typical MRI study will take place over tens of minutes and requires the subject to assume supine positioning, it is clinically important to establish how the healthy body will dynamically change in response to changing directional forces of gravity when assuming supine positioning.

It is known that the distribution of abdominal organs, lung volume, blood and free water in the body will all depend on body positioning, due to the dependence on gravity[8–11]. As such, it is a reasonable assumption that both whole-lung volume and water content within the lungs will also be dependent upon body positioning, and will continuously adapt over time after assuming supine positioning. The main purpose of this study will be to establish a time-line sequence of events that occurs within the healthy lungs after supine positioning. The changes over time within whole lung and regional (chest-to-back direction) lung volume, lung water content, and LWD will be examined. Both functional residual capacity (FRC), the minimum lung volume, and functional residual capacity + tidal volume (FRC+TV), the maximum lung volume, will be considered with normal tidal breathing (free-breathing). The hypothesis entering this study is that the known increase of 300-500 ml of blood[10,11] to the thoracic cavity after supine positioning will be the main driver behind a steady increase in LWD throughout the lung space over tens of

minutes. It is predicted that both FRC and FRC+TV respiratory phases will behave similarly to each other, with potential for tidal volume (TV) to dynamically adapt to the change in position as well.

This study will use a previously described ultrashort echo-time (UTE) Yarn-Ball (YB)[12] k-space MRI sequence using monitoring of center of k-space as a respiratory navigator signal, chest array coils with coil-combination, and novel signal referencing map to obtain fast and quantitative whole-lung water density 3D-images in a free-breathing environment, as described by Meadus et al (2021)[5]. The sequence will be repeated multiple times (18) over tens of minutes in order to determine the dynamic changes over time in global and regional lung volume, lung water volume, and LWD at FRC and FRC+TV. On a separate day, the same YB experiment will be repeated with the addition of a total lung capacity breath-hold at the half-way time point to evaluate a different physiologic stress related to lung volume changes. Finally, real-time 2D gradient echo (GRE)[13] imaging and a nitrogen washout test (gold standard test for lung volumes)[14] will be used to confirm YB findings of lung volumes at FRC.

A secondary goal of this study will be to further optimize this UTE YB sequence such total scan times are reduced from its predecessor version, while improving visual quality and maintaining accurate rLWD% calculation. Finally, a novel in-house machine learning approach to the segmentation of the lungs will be applied to the reconstructed images in order to get a higher degree of accuracy when segmenting the lung volumes and the small vasculature within the lungs.

1.2: Characterization of the Lungs

1.2.1: Dynamics of Lung Anatomy

The main purpose of the lungs is to provide a sufficient supply of oxygen to the blood. The systems and processes that enable this task is known as the respiratory system. Oxygenated air is drawn into the body via contraction of the diaphragm and intercostal muscles creating a

negative pressure (relative to atmospheric pressure) and increased lung volume within the lung space. The air enters through the trachea, down the bronchus, dividing into the left and right bronchioles and finally into the alveoli. Pulmonary capillaries carrying deoxygenated blood wrap around individual alveolus in order to receive oxygen from the fresh air and expel the carbon dioxide that is naturally produced by the body[15]. The process of gas exchange in the lungs occurs due to simple diffusion, whereby gasses will permeate across the respiratory membrane from an area of high pressure to an area of low pressure; oxygen is drawn out of the alveoli into the capillaries, while carbon dioxide is drawn out of the capillaries into the alveoli, thereby oxygenating the blood.[16]. Gas exchange occurs across a very, very thin space that exists between the thin portion of the capillary endothelial cells and overlaying alveolar epithelial cells. This space is known as the air-blood barrier (ABB)[2], and is typically less than ~0.2 um in thickness is normal lungs[17] (Fig. 1.1.A).

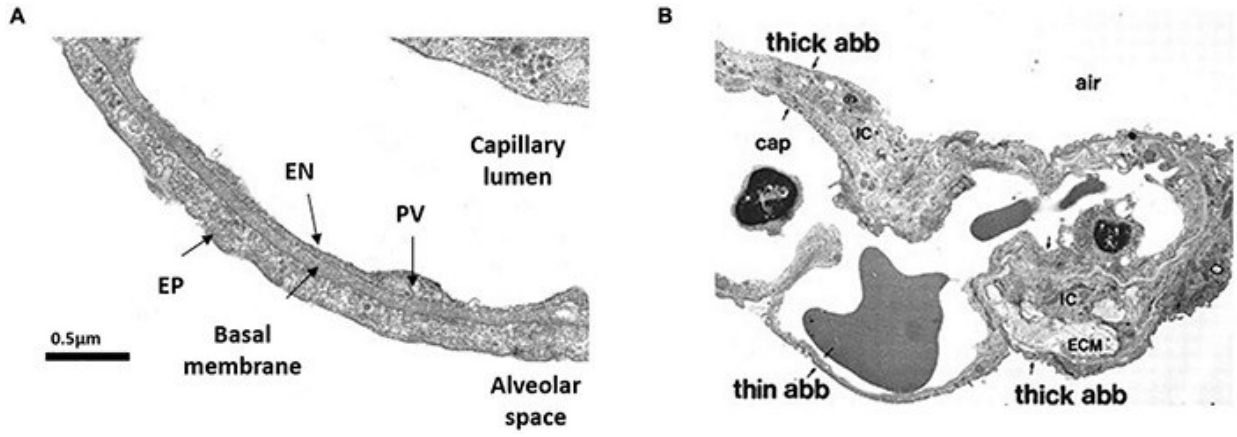

Figure 1.1: *Morphology of the air-blood barrier (ABB).* **(A)** *Thin portion of ABB showing the close apposition between alveolar epithelium (EP) and capillary endothelium (EN). PV is plasmalemmal vesicle.* **(B)** *Microscopy image showing the ABB and its thin and thick portions. Where "ECM" is the extra cellular matrix, "cap" is the lung capillary, and "IC" is the interstitial cell[17].*

The process of lung expansion drawing oxygenated air into the lung space is known as inhalation; conversely, lung contraction expelling CO_2-rich air is known as expiration. At rest, the completion of one inhale and one exhale is one breath in the passive breathing cycle. The volume of the lungs at the end of passive exhalation is the Functional Residual Capacity (FRC), and represents the point of the breathing cycle where the lung tissue elastic recoil and chest wall

outward expansion are balanced and equal; In a normal individual, this is roughly 3L[18]. The amount of air that a person passively inhales (and subsequently exhales) is known as Tidal Volume (TV). TV for the average male is around 500 mL, while it is around 400 mL for the average female[19]. The volume within the lungs at the end of passive inhalation is the Functional Residual Capacity + Tidal Volume (FRC + TV). Fig 1.2 depicts respiratory lung volume metrics, highlighting volume differences that occur between normal tidal breathing (FRC to FRC+TV) vs. maximal inhalation/exhalation and total lung capacity. The highly dynamic nature of the human body means many things can affect the normal operating ranges of the respiratory cycle, including (but not limited to): exercise[20], age[21], height[21], sex[21], weight[22], lung disease[23], and body position[24,25]. Ideally, the amount of air taken into the lungs (ventilation, or V) will match the amount of deoxygenated blood flowing into the lungs (perfusion, or Q) in a 1:1 ratio in all lung tissue; The body has an ability to vary V or Q in response to physical or environmental changes to maintain this ratio (known as "V/Q Matching").[26] Dynamic changes that occur within the lungs after a change in body position, particularly from standing up to supine, are particularly important in regards to magnetic resonance imaging (MRI), as a patient is typically in supine positioning, with imaging starting immediately following the change in body position. These dynamics will be a key focus of this study and discussed further.

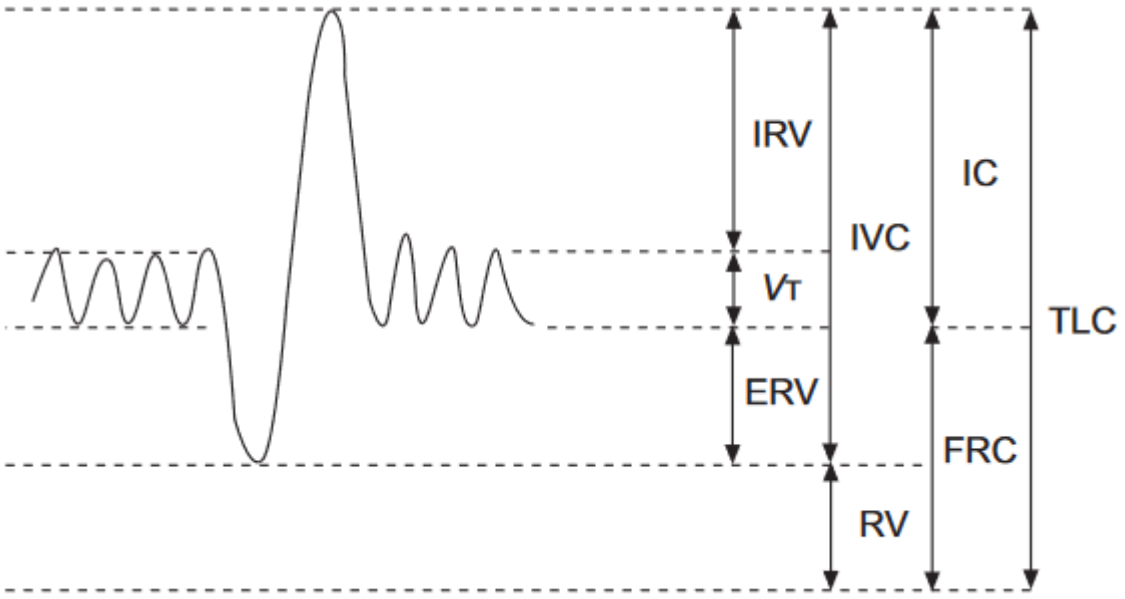

Figure 1.2[14]**:** *All measurable respiratory lung volumes. FRC is the volume of gas present at end-expiration during normal tidal breathing, Vt is the volume of air inhaled during normal tidal breathing (tidal volume), and FRC+TV is the volume of gas present at end-inspiration during normal tidal breathing. Maximal exhalation (ERV) is naturally a smaller volume than FRC, while maximal inhalation (IC) is naturally a larger volume than FRC+TV.*
IRV, IVC, RV, and TLC are important measurements in many respiratory studies, though not relevant to this work.

.

1.2.2: Lung Water

The aforementioned ABB has two portions, a thin side (previously discussed as the site of gas exchange) and a thick side. The thick side is the site of fluid and solute exchange and consists of an interstitial space filled with extracellular matrix and lymphatics separating the endothelial and epithelial cell layers of the capillary perimeter[2]. The thick side of the ABB has a variety of functions that serve to keep the alveoli relatively dry and healthy, such as filtering out particulates in the air breathed in, presenting immune responses to bacteria and viruses causing infection, filtering out pharyngeal fluid that may have emanated from the stomach or the mouth, and, most importantly, adapt its flow of fluid out of the interstitial space in response to regular

physiological changes or other lung injury[27]. Trans-capillary and trans-epithelial fluid exchange is governed by the Starling law[17]:

$$Jy = Kf * [(P1 - P2) - \sigma(\pi 1 - \pi 2)] \quad (1.1)$$

Where J_v is the rate of fluid flow, Kf is the filtration coefficient, P_1 is the capillary hydraulic pressure, P_2 is the hydraulic pressure of the interstitial space, σ is the protein reflection coefficient, π_1 is the capillary oncotic pressure, and π_2 is the interstitial oncotic pressure. If there is an increase in extravascular volume, the lymphatic system will engage and increase flow out of the capillaries[17]. For example, high intensity exercise shows excess lung water in healthy individuals for hours post-exercise, with swelling of the lymphatics clearing the increase lung water content[28]. A visual depiction of the ABB (including the thick side) is seen in Fig. 1.1.B, and a visual depiction of Starling's law is seen in Fig. 1.3.

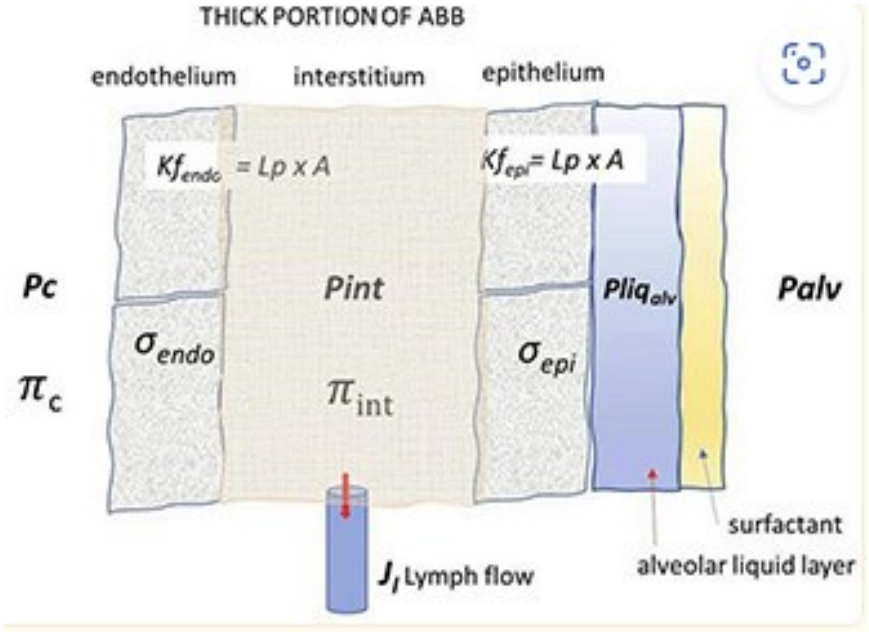

Figure 1.3; *Lung fluid compartments of the ABB and parameters governing fluid exchanges. P_c, P_{int}, and $Pliq_{alv}$ are capillary, interstitial, and alveolar liquid hydraulic pressure, respectively; π_c and π_{int} are capillary and interstitial oncotic pressure, respectively; σ_{endo} and σ_{epi} are protein reflection coefficient of endothelium and epithelium, respectively; P_{alv} is the alveolar pressure; Kf_{endo} and Kf_{epi} are the endothelial and epithelial filtration coefficient, respectively. Lymphatic drainage (J_l) occurs from the thick portion of ABB where lymphatics are located[17].*

1.2.3: Lung Disease

Excess water in the lungs is known as pulmonary edema (PE), and is typically the result of either increased driving pressures for fluid filtration or weakening of the barriers that restrain fluid and protein movements[2]. Practically, PE is split into two different types; cardiogenic PE (usually caused by an increase in capillary hydrostatic pressure[2]) and non-cardiogenic PE (usually caused by injuries to the alveolar-capillary barrier[2], also termed acute respiratory distress syndrome (ARDS)[29]). Both types of PE can cause shortness of breath and/or productive coughing. Cardiogenic PE will differentiate itself from non-cardiogenic by presenting symptoms such as arterial blockages (potentially causing heart-attacks) associated with chronic systolic or diastolic heart failure, and mitral or aortic valve disease. Non-cardiogenic PE on the other hand is associated with other clinical disorders, such as pneumonia or sepsis, and will present with vomiting, aspiration of gastric contents, decreased levels of consciousness[29]. Elevated lung water content is a clinical indicator of heart failure[3], ARDS[30,31], non-ARDS sepsis[32] and even COVID-19 patients[33]. Furthermore, lung water content can present differently in cardiogenic PE vs non-cardiogenic PE, which, given their different diagnostic and therapeutic objectives, is an important differentiation[34]. Overall mortality rate of both forms of PE is high (12% in cardiogenic[35] and 30% in non-cardiogenic[36]), making proper identification of PE vital to treatment strategies.

When considering lung water content and PE, it is important to remember that normal operating ranges of the lungs for an individual is highly variable, thus some individuals inherently may have larger lung spaces and therefore higher lung water content than others. To ensure the amount of lung water measured within an individual is accurate relative to the lung size, Lung Water Density (LWD) can be derived, globally, by dividing the amount of total water within the lung by the volume of the lung or regionally as detailed in this thesis. Elevated LWD has been seen in patients with reduced exercise tolerance, which is a cardinal feature of heart failure[1], as well as predictive of patient outcomes in heart failure[4]. Indeed, there appears to be great prognostic value into accurate quantification of LWD.

1.2.4 Measuring Lung Water Content

Currently, there are several non-invasive methods to identifying elevated lung water content. A process known as auscultation involves using a stethoscope on the patient's chest to listen for abnormalities in the frequency, quality and amplitude of a breath. A discontinuous, explosive and nonmusical lung sound is known as a "crackle", which is often noted in patients with PE and other pulmonary disorders[37]. While a staple of the basic physical examination, auscultation is a qualitative measurement only, and cannot definitively differentiate between various pulmonary disorders.

One of the most common imaging modalities for diagnosing PE is a chest radiograph (chest X-ray). Chest radiographs provide imaging features of the lungs that can not only help diagnose PE, but also moderately helps distinguish between noncardiogenic PE and cardiogenic PE. However, chest radiography can erroneously interpret hemorrhages or pus presenting as PE, has substantial inter-observer variability in the interpretation of radiographs, and has no quantitative way of measuring lung water content[29,34].

Computed tomography (CT) is experiencing increased use in the diagnosis of pulmonary disease. The higher-resolution three-dimensional images that CT provides has shown a greater ability to detect and characterize pleural effusion (water accumulation between lungs and chest wall), and can provide additional useful information affecting diagnosis or management of pulmonary disease in up to 70% of cases that would otherwise be unavailable with chest radiography[38]. CT remains limited, particularly in the research setting, by the high-dosage of ionizing radiation required to obtain CT images, and cannot provide accurate quantitative measurements of lung water content without using secondary techniques[39]. Recent advances in CT techniques have introduced the feasibility of ultralow dose CT, reducing the radiation dose by nearly 14 times (1.8 vs. 0.13) while maintaining high enough image quality for lung nodule detection[40].

Lung ultrasonography (LUS) provides a semi-quantitative measurement of lung water by summing what are known as "B-lines" in the resulting image, giving an approximation of lung

water content. LUS uses high-frequency sound waves to obtain it's images and is a relatively simple and portable machine, making it an appealing choice for immobile/bed-ridden patients and for limiting radiation exposure[41]. LUS has also shown high sensitivity to pulmonary bruising, a known non-PE related cause of ARDS. The major drawbacks to LUS is the lesser qualitative quality of the images (often appearing "speckled" in appearance), smaller field of view, and high variability in quantitative results in the presence of increased air in the lungs (emphysema, pneumothorax, etc.)[42]

The standard in-vivo quantitative measurement of lung water content is known as transpulmonary thermodilution (TPTD), and is capable of measuring lung water content (specific to this method, the lung water in the extravascular space) as well as cardiac output and other lung volumetric parameters. This method requires injection of a bolus of known temperature saline through a central venous catheter (which is thermistor-tipped), and calculates various cardio-pulmonary metrics via transit time of the bolus and time-course changes of circulating blood temperatrue[43]. TPTD has shown good correlation as a quantitative lung water measurement with the accepted gold standard of gravimetric lung measurements post-mortem, and has been shown to clinically establish the existence and nature of PE[43,44]. However, given the highly invasive nature of the method, it is restricted to critically ill patients in the ICU and during operation.

Quantification of lung water content is becoming an area of increased interest in the field of MRI due to advancements in sequencing and hardware capabilities. MRI inherently uses the existence of hydrogen protons to obtain signal, thus it follows that water content within the lungs could be directly calculated from an MRI image. This, combined with the lack of ionizing radiation within an MRI, makes it an appealing choice for EVLW measurement. The barriers related to using MRI for lung imaging will be discussed in later sections.

1.2.5: Gravitational Effects on the Lungs - Changes Over Time

A standard MRI scan requires the subject to lie down, most commonly on their backs (supine) (Fig. 1.4). Furthermore, MRI scans often take tens of minutes to complete. Due to this, important consideration must be placed into what potential changes may occur within the body

and the organs of interest when the gravitational forces affecting the body change from head-to-toe (standing forces) to chest-to-back (supine forces), and how these changes develop over time.

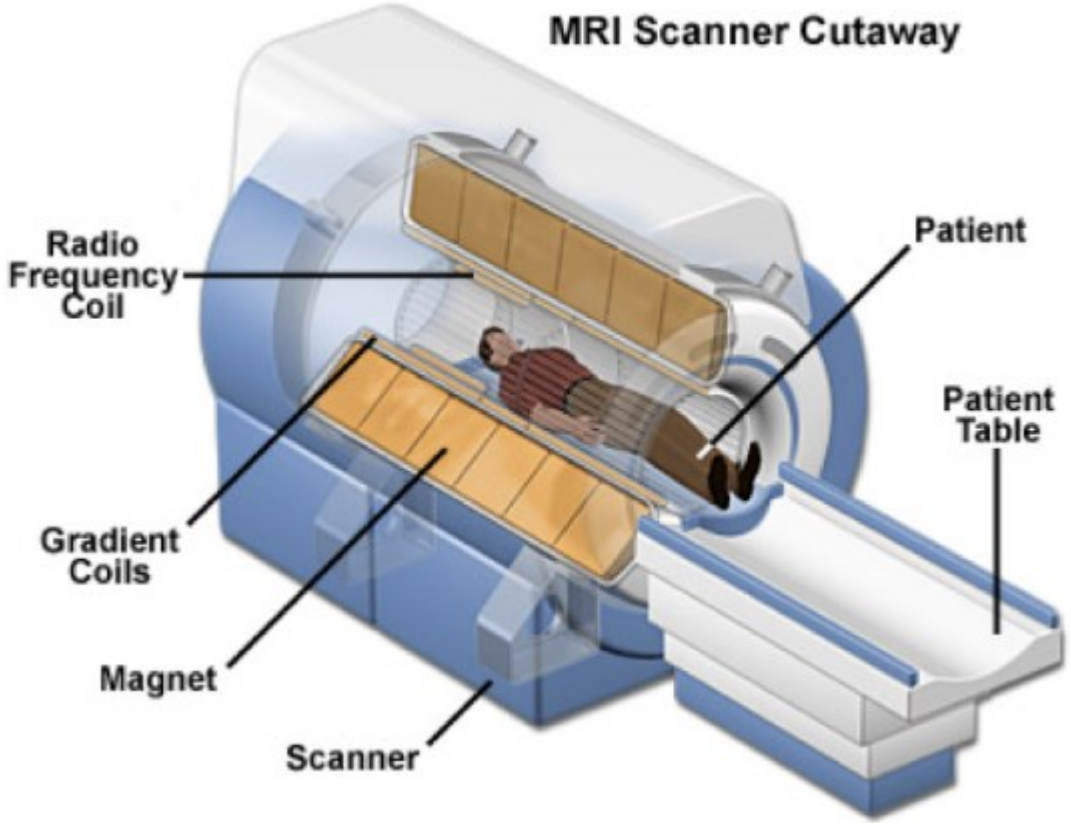

Figure 1.4: *A cutaway of an MRI Scanner. The large magnets and coils required for a MRI scan means the subject must be sent into the middle of the cylindrical MRI machine, typically in supine positioning*[45].

There is a well-established chest-to-back gradient in LWD that forms when taking supine positioning. This phenomenon was first introduced by Hopkins et al (2007)[7], who suggested that the lungs behaves like the deformable spring toy known as a "*Slinky",* an association that was coined *"the Slinky Effect".* Much like how a *"Slinky"* distorts more heavily in the upper portion of a vertically orientated *"Slinky"* due to increased weight caused by the coils in lower regions, the lungs will experience greater density of lung tissues in its dependent (i.e. lower in the gravity field) regions (in this orientation, this would be towards the back of the lungs). This gravitational dependence is responsible for the characteristic chest-to-back gradient in LWD. MRI studies performed after Hopkins et al (2007) have confirmed the existence of *"the Slinky Effect"*[5,6],

however, to date, there has been no definitive research demonstrating exactly how long it takes to establish this effect post-supine positioning, nor has it been concluded how long it takes for the effect to reach steady-state. Seeman et al (2022)[6] concluded that the LWD gradient reverses in direction shortly (~9 minutes) after a healthy subject assumes prone positioning, further suggesting that the *"Slinky Effect"* is heavily dependent upon changing gravitational forces and forms quickly. An example of a typical chest-to-back gradient of LWD in a healthy individual is depicted in Fig 1.5.

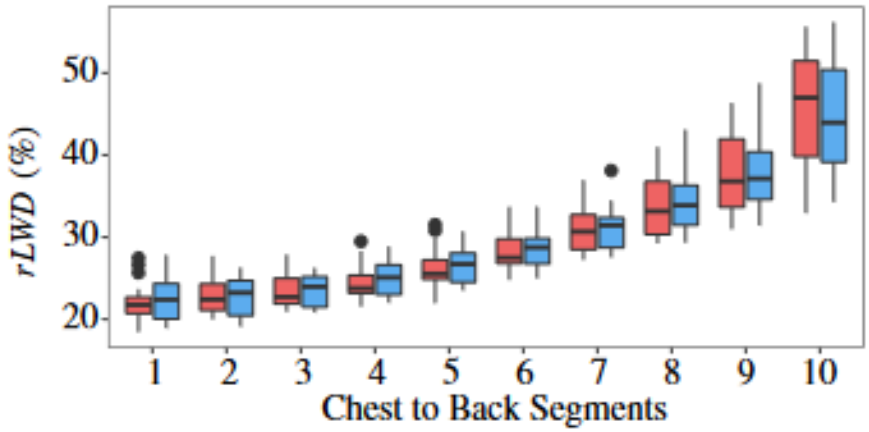

Figure 1.5: *A depiction of the "Slinky Effect". Spatial variation in LWD from 10 equal lung volumes from chest to back for the left (red) and right (blue) lungs. All results shown using box and whisker plots that indicate the median value and lower and upper quartiles for the box, and lowest and highest values at the ends of the whiskers. Black circles are outliers*[5].

There are several other relevant phenomena that are known to occur in the body when supine positioning is assumed that must be considered when discussing the context of changes in lung water content/LWD over time. Firstly, it has been observed that the abdominal organs (diaphragm, liver and kidney) redistribute themselves within the abdominal space in accordance to the directional forces of gravity that the body is experiencing[8,9]. There is potential for this redistribution of the abdominal organs to "crowd" the lungs, causing them to compress and decrease in total volume over time when the abdominal organs are not experiencing downwards (towards the toe) forces of gravity. Secondly, pulmonary blood flow tends to redistribute towards gravity-dependent regions of the lungs, as well as an increase in venous cross-sectional area in gravity-dependent regions[10]. This redistribution of blood could cause regional changes in perfusion (and therefore V/Q matching) or increased water content measured over time. Thirdly,

300-500 mL of blood is known to shift towards the thoracic cavity with supine positioning[46,47], which also has the potential of increasing total water content measured over time. Lastly, extended supine positioning causes sizeable increases in free water measured in plasma volumes (~440 mL expansion over 35 minutes)[11]. It is yet to be studied how much of this free water expansion occurs within the lung space, however, there is potential for free water measured within the lung space to increase over time with supine positioning due to this phenomenon.

1.2.6: Obstacles to MR Imaging of the Lungs

MRI uses a combination of powerful magnetic fields and receiver coils to capture signal from the spins of hydrogen protons within the body. When considering a gradient echo sequence (described further in section 1.3.1 below) signal acquisition will be described by the transverse signal (M_{xy}) decay equation described in equation 1.2:

$$Mxy(TE) = Mxy(0) * e^{-\frac{TE}{T2}*} \quad (1.2)$$

Available measurable transverse signal within a given tissue at a given echo time, $M_{xy}(TE)$, is thus dependent upon $M_{xy}(0)$ (maximum available transverse magnetization, determined by pulse sequence parameters of T1, TR and flip angle) and T2*. Tissue contrast arises from differences in T1 and T2* times between tissues[48]. For many applications of MRI, obtaining high contrast, high signal images is a highly achievable task that is largely dependent upon basic manipulation of the above sequence parameters. The unique composition of the lungs, however, introduce some challenges to lung MRI that must be overcome in order to obtain quantifiable 3D images.

Firstly, the high-air content nature of the lungs results in much lower tissue density compared to adjacent tissue (up to 10 times lower), resulting in MR signal to be proportionally lower within the lungs than surrounding tissue using typical MRI practices. The low signal-to-noise ratio (SNR) that is inherent within the lungs makes quantification of lung signals challenging. Scan repetition and signal averaging can be employed, however, this can extend image acquisition time greatly, potentially making it unfeasible for standard clinic routine. Furthermore, one could increase the voxel size of the image in order to increase SNR, however,

this would make identifying small lesions or other lung pathologies difficult to spot[49] and leads to partial volume errors with blood vessels.

Secondly, due to differences in magnetic susceptibility between air and tissue (difference of ~ 8 ppm between the two), static local magnetic field gradients exist at lung-air interfaces. The extremely high number of lung-air interfaces that exist within the lungs, particularly the alveoli, creates a highly inhomogeneous local magnetic field gradient within the lungs. This field will cause rapid dephasing of the transverse signal, leading to a very short apparent transverse relaxation times ($T2^* \approx 0.5$ ms at 3T) within the lungs and potential off-resonance artifacts. Pulse sequences must be designed with extremely short echo times to compensate ($TE \leq 100$ μs), a design challenge which requires custom pulse sequences and potentially high performance gradient systems to achieve. Similarly, the T1 of lung parenchyma is relatively long (1,300 ms at 1.5 T), which requires appropriate pulse sequence parameters that avoids T1-weighting (e.g. low flip angles)[49].

Thirdly, consideration must be placed into correcting for respiratory motion. An average adult breathes ~12 times per minute or once every ~5 seconds[50], with lung volume continuously expanding and contracting over the course of the breath and accompanied rise/fall of the diaphragm and chest. If MR signals are received in multiple different phases of the respiratory cycle, the resulting images would be extremely blurry and inaccurate. Acquiring signal at breath-holds (max inspiration or max expiration) is a straight-forward solution to this issue, however it limits the flexibility on sequence parameters and performance, and it is often clinically useful to acquire data during regular free-breathing conditions. For similar reasons as respiratory motion, cardiac motion must be accounted for to obtain artifact-free images.

Fourthly, the lungs and the torso are comparatively much larger than many other organs/areas of interest, which in turn requires a large field of view (FOV) to accurately capture the entirety of the lungs in a 3D context (typically >300 mm + in all directions, see section 1.4.5). Careful consideration must be placed into k-space sampling in order to maintain a high enough sampling rate that satisfies the Nyquist sampling criteria and wrap-around artifacts are avoided[51]. Furthermore, a spatial resolution that is high enough to give quality images capable of lung parenchyma segmentation is required; given the inverse relationship between k-space FOV and pixel width, the designed sequence must be capable of delivering adequate FOV and spatial

resolution without extending into unsafe slew rates or exceed the capabilities of the gradient hardware.

Lastly, despite MR signal originating from the hydrogen protons within the body, it is not practical to directly quantify obtained signal into a known unit such as “water content” or “water density” as the RF transmitter and receiver have non-constant local magnet fields, or “B1 inhomogeneity”. MR signal is thus expressed in arbitrary units (au), and historically there is no direct conversion between MR signal and units of water. Therefore, in order to obtain a quantification of lung water and consequentially LWD, a signal reference must be used in order to quantify the signal in water-density units. Local B1 inhomogeneity (both transmitted, $B1^{+}$, and received fields, $B1^{-}$) makes establishing an external signal reference difficult due varying local magnetic fields causing biased signals outside of the body. This reference must be robust enough to use from subject-to-subject.

1.3: Imaging Methodology

1.3.1: Lung MRI Pulse Sequences

Increased interest in MRI technology as a clinical tool has sparked major advancements in MRI technologic capabilities and ingenuity within MRI sequence design, aiding the ability to overcome the challenges to lung MRI described in section 1.2.6. Typical clinical scanners boast gradient strengths up to 80mT/m, peak slew rates of 200 T/m/s, and field strengths of up to 7 T are now relatively common[52] (less commonly, 9.4 T or above[53]). Given that increased field strength is proportional to an increase in signal, one would guess that using the maximum field strength possible would aid in overcoming the relatively low MR signal that exists within the lungs; However, increasing field strength has a byproduct of lengthening T1 relaxation times, shortening T2 and T2* relaxation times, and increasing the inhomogeneity of the local magnetic fields[53] (Fig. 1.6 A). As a result, the baseline increase in SNR caused by an increase in field strength cannot be realized within lung MRI without sequence design that is able to overcome the more stringent physical properties that come with increased field strength. In particular, the need for ultrashort

echo times to address lower T2* values at 3T is vital. Strengths higher than 3 T are typically not used for lung MRI (likely related to increased need for body B_1^+ coils and further reduction in T2* times). Beyond the inherent low SNR within the lung space, the other major challenge that must be overcome the local magnetic field inhomogeneity caused by large magnetic susceptibility differences at the lung-air interfaces. With T2* being very short within the lungs (~1.4 ms at 1.5 T[54] and as low as 0.5 ms at 3T[49]), most of the MR signal that would exist within the lungs has been destroyed at TE times often used to measure other tissues (Fig. 1.6 B).

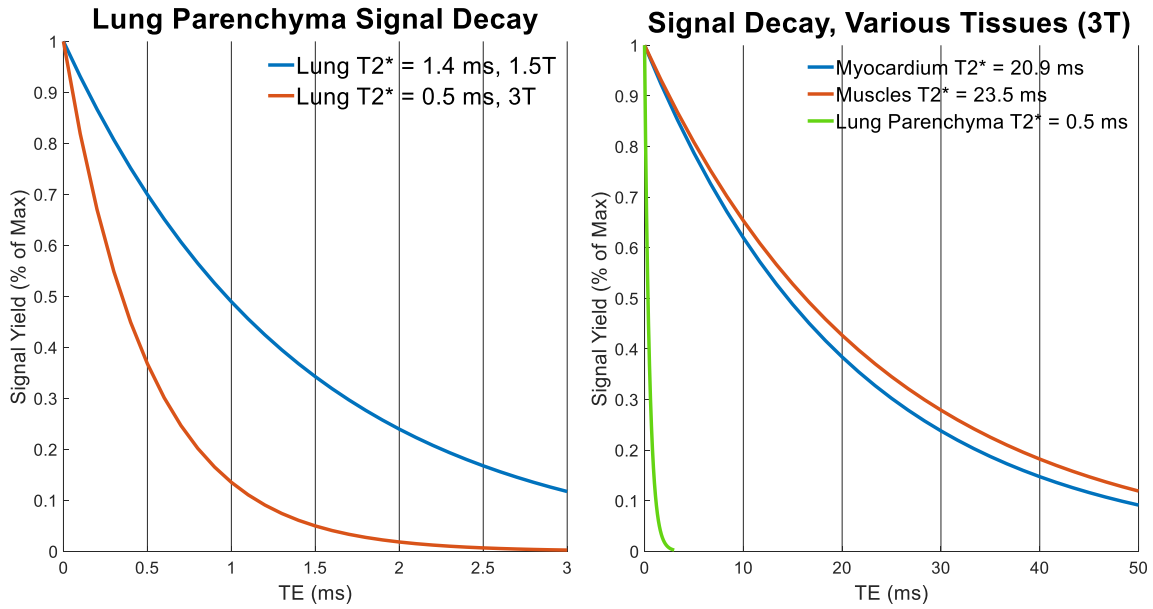

Figure 1.6: A) *Percentage of MR signal available at a given TE (< 3 ms) in lung parenchyma at 1.5 T (blue) vs. 3T (red). Note that more than half the available signal has decayed by TE = 0.5 ms.* **B)** *Percentage of MR signal available at a given TE (< 50 ms) in myocardium (T2* ≈ 20.9 ms[55], blue) vs. Muscles (T2* ≈ 23.5 ms[56], red) vs. lung parenchyma (green). All values at 3T. TE times acceptable for other tissue would result in null signal from the lungs.*

One of the most common and versatile MRI pulse sequences is the spoiled gradient echo (SPGR). The SPGR sequence is an extension of a standard gradient echo design, however, the SPGR utilizes a semi-randomly varying phase angle (φ) in each subsequent excitation RF pulse with the goal of eliminating the residual transverse magnetization left by previous pulses[13,57]. This is known as RF-spoiling (Fig. 1.7).

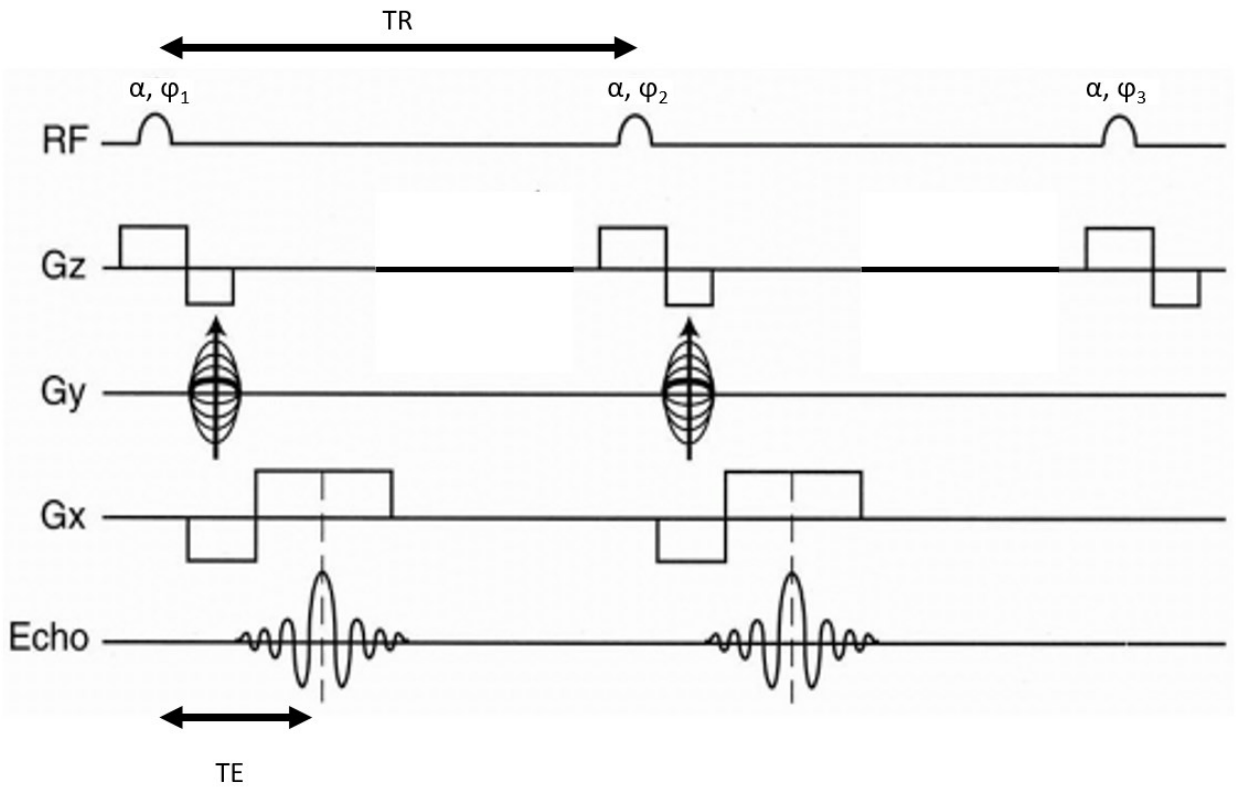

Figure 1.7: *Standard SPGR pulse sequence design. RF is the excitation radiofrequency pulse with flip angle α and phase angle φ. Gz, Gy, and Gx are the slice, phase and readout gradients, respectively. Each subsequent RF pulse has a varied phase angle to eliminate transverse magnetization between pulses.*

The signal of an SPGR sequence, assuming longitudinal steady-state and perfect spoiling, is determined by equation 1.3[58]:

$$S = k[H]\sin\alpha\frac{1-e^{-\frac{TR}{T1}}}{(1-(\cos\alpha)e^{-TR/T1})}e^{-\frac{TE}{T2}*} \quad (1.3)$$

Where S is the signal, k is a scaling factor, and [H] is the spin density. Employing ultra-short TE (≤100 μs) and lower flip angles (α ~ 1-2°) will minimize both T1 and T2* weighting, facilitating proton density weighting and the ability to detect lung parenchyma signal[49]. SPGR acquisitions are fast (short TRs) and thus can inherently reduce both cardiac and respiratory motion artifacts[59]. However, the minimum echo-times achievable, on the order of 1 ms, are far too long for quantification of lung water density without the use of additional techniques, particularly at 3T.

Turbo spin echo (TSE) is another often used pulse sequence in lung MRI, due to the elimination of the effects of the very short T2* in the lungs. Each 180° refocusing RF pulse in a TSE sequence will act to re-phase all of the signal that would have otherwise been destroyed by local magnetic fields caused by magnetic susceptibility differences at the lung-air interface. Thus a spin echo sequence is restricted only by the T2 time (~30 ms at 1.5T[49]) rather than the much shorter T2* times. While TSE sequencing has been proven to be clinically useful in identifying some lung pathology[59,60], it is highly susceptible to image blurring due to T2 decay causing signal reductions in later echoes of the train[49]. Spin-echo sequences are typically slower than GRE, making acquisition times which are short enough to accommodate lung MRI difficult to achieve. Furthermore, "ghosting" artifacts caused by respiratory and cardiac motion become more of an issue[59]. An advanced spin-echo technique known as Half-Fourier Acquisition Single-shot Turbo Spin Echo (HASTE) can greatly reduce acquisition time compared to traditional TSE and thus suffers less from respiratory and cardiac motion artifacts, however, it sacrifices signal-to-noise and tissue contrast to do so[61]. Furthermore, TSE/HASTE sequences are typically 2D only, making this type of sequencing less desirable given the need for large FOV volumetric images.

1.3.2: Non-Cartesian Sampling for UTE

Any sequence that can achieve an echo time of roughly less than 100 μs is referred to as an ultra-short echo time (UTE) sequence, a design parameter that avoids the rapid decay of transverse magnetization caused by magnetic susceptibility differences.

Non-Cartesian k-space sampling methods are able to achieve such short TE times to be classified as a UTE sequence. 2D center-out radial trajectories use many radial "spokes" or radial arms that all originate from the center of k-space, projecting outwards towards the edge of k-space in a star-like shape (Fig. 1.8). No phase-encoding gradients are required, resulting in the ability to acquire the center of k-space immediately after excitation and achieve UTE times. The

center-out nature of radial trajectories results in oversampling of the center of k-space, which can eliminate "ghosting" artifacts that arise from motion during image acquisition; artifacts created by moving objects are evenly diffused across the whole image instead of localized to one phase-encoded step or direction[62]. The major disadvantage of radial k-space sampling lies within its inefficiency; for the Nyquist criteria to be maintained (sampling rate at least twice the highest frequency of the signal), the number of radial k-space arms that must be acquired must be greater than with Cartesian sampling by a factor of $\pi/2$[63]. Furthermore, data obtained in a non-Cartesian acquisition is not evenly sampled over k-space, and thus cannot have the Fast-Fourier transform applied. A process known as "gridding" places the obtained data into useable Cartesian grid coordinates (often with finite sampling kernel to obtain an estimation of the inverse Fourier transform[64]), which adds computational time to the reconstruction process, and introduces potential reconstruction artifacts on the final image in the case of gradient and/or timing imperfections[62].

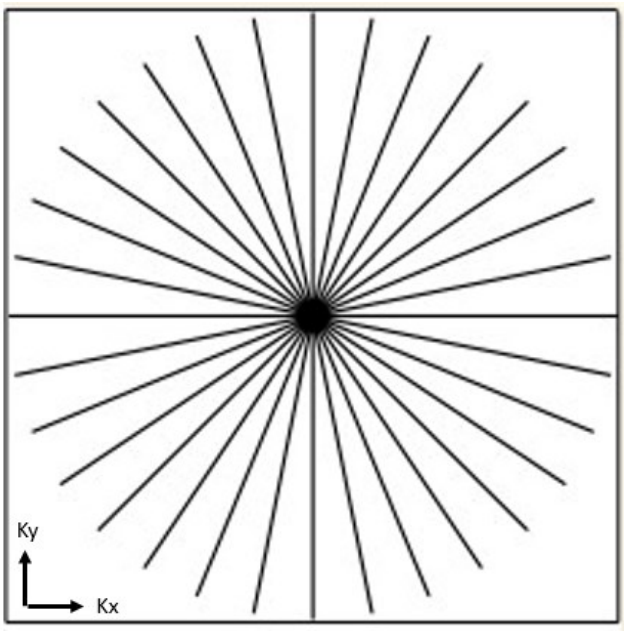

Figure 1.8[63]**:** *Radial k-space sampling.*

A similar 2D non-Cartesian k-space sampling method, spiral sampling, starts at the center of k-space and winds outwards in concentric circles, forming a "bullseye" shape in k-space (Fig.

1.9). This is achieved by applying sinusoidal phase and frequency gradients that slowly increase in amplitude over time[65]. The spiral nature of the sampling achieves greater k-space coverage in fewer shots (potentially even single-shot) than either radial or Cartesian methods, making it UTE compatible. However, it is potentially more affected by incorrect gradient timing and artifacts arising from the gridding process than radial sampling due to the longer readouts[63].

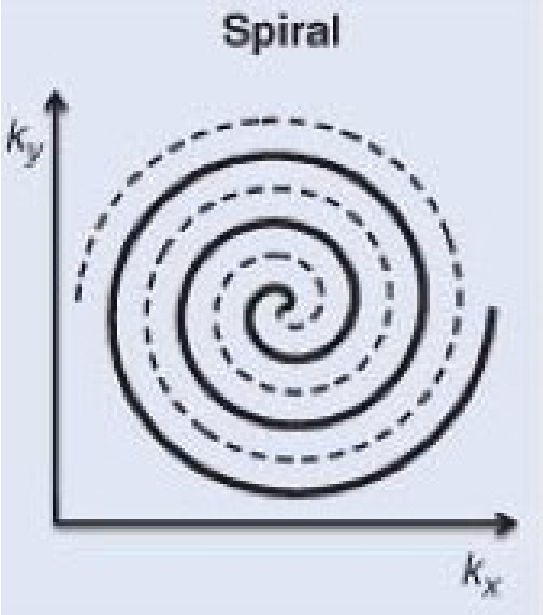

Figure 1.9[66]: *Spiral k-space sampling.*

3D isotropic images are possible using a three-dimensional version of radial sampling, often referred to as "koosh-ball" sampling (Fig 1.10). This sampling technique behaves in the same manner as 2D radial but simply projects in all 3 k-space dimensions, and still does not require phase-encoding gradients (maintaining compatibility with UTE). The characteristic shape of "koosh-ball" stems from circles of constant latitude, whose radius is dependent upon the equidistance spacing of each radial arm at the edge of k-space ($\Delta k = 1/ FOV$, $RES = 1/(2k_{max})$, RES = spatial resolution)[67]. "Koosh-ball, however, is even more inefficient than 2D radial, requiring π times the number of readouts compared to 3D Cartesian to maintain the Nyquist theorom[67]. If R represents the number of k-space points that are acquired on a single readout ($R = FOV/ (2 * RES)$), then the minimum number of trajectories needed to achieve full 3D radial sampling is:

$$Ntraj = 4\pi R^2 \qquad (1.4)^{68}$$

A 3D radial sequence with FOV of 350 mm and spatial resolution of 3.5 mm (assuming all directions, thus R = 50) would require 31,416 trajectories to achieve full Nyquist sampling, while a 3D Cartesian sequence would only require 10,000 trajectories.

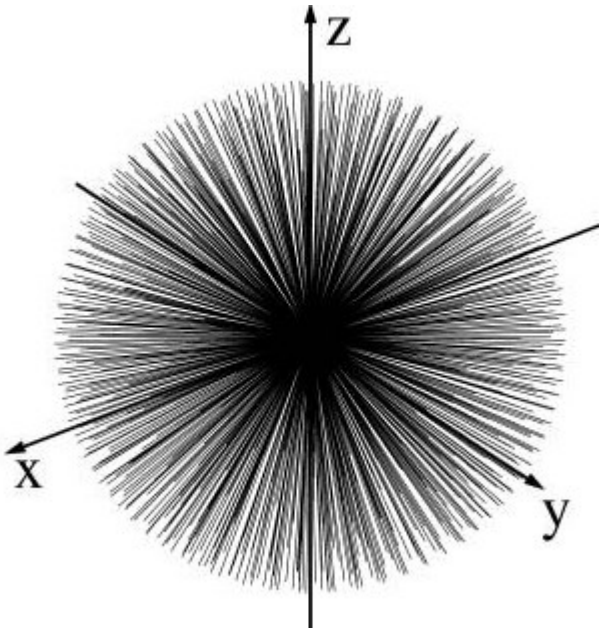

Figure 1.10[67]**:** *3D radial k-space sampling ("Koosh-ball")*

In another adaptation of k-space sampling, "3D-cones", the radial spokes "twist" around an axis, rather than projecting outwards directly in a straight line (Fig. 1.11 A). These twists occur in the x-y plane forming a spiral interleaf on the surface of each "cone"; This increases the readout time per trajectory, but also leads to fewer trajectories being required. Ultimately, 3D cones can provide overall shorter scan times and more uniform sampling density than 3D radial. The number of cones required to adequately sample k-space is determined by:

$$Ncones = \left[\frac{\pi}{2} * \frac{FOV}{RES}\right] + 1 \qquad (1.6)^{69}$$

The result of the combination of the k-space cones can be seen in Fig. 1.11 B. 3D cones is extremely efficient, needing only 800 trajectories for full Nyquist sampling where traditional 3D radial would require 31,416 excitations[12]. However, the longer readout times reduces the high-resolution features being imaged, and there is an increased risk of artifact due to higher sensitivity to motion/flow artifacts and off-resonance blurring[69].

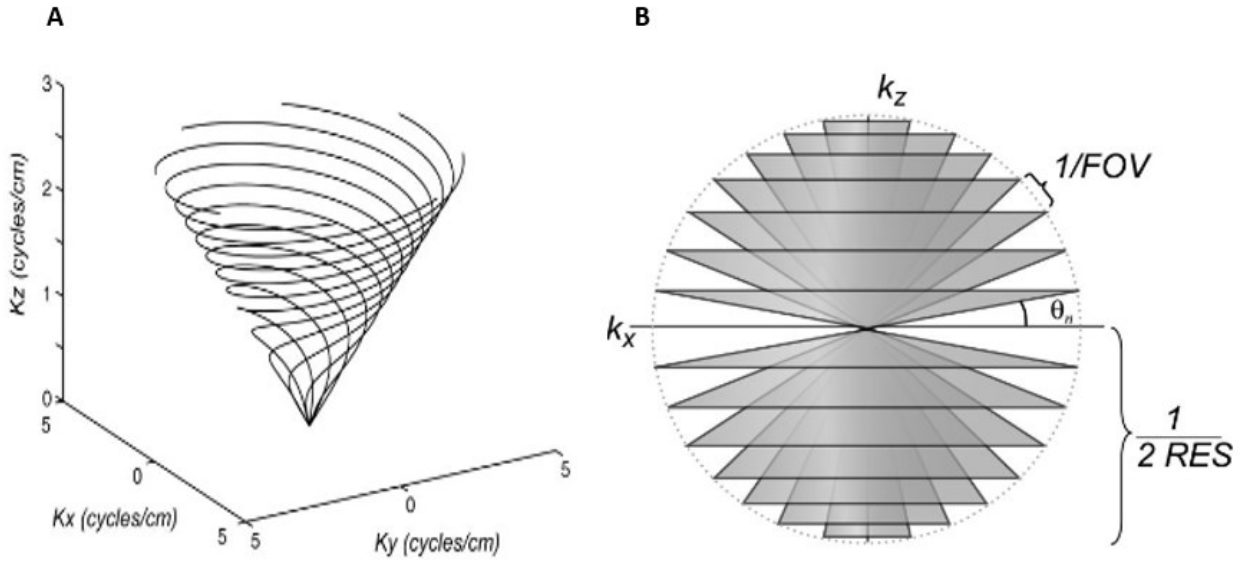

Figure 1.11[69]**: (A)** *One twisting "cone" k-space trajectory and* **(B)** *Complete k-space coverage using multiple cones.*

In general, all UTE sequences are limited by safety concerns that arise with high slew rates. In order to obtain these ultra-short echo times and efficient data acquisition rates, gradients must be ramped up extremely quickly in order to properly capture the image data immediately after excitation[70]. Slew rate is defined by the ratio between peak gradient strength and time to rise to peak, thus, the need for very rapidly changing gradients will cause high slew rates. High slew rates have been shown to cause peripheral nerve stimulation[71].

1.3.3: Yarnball

Stobbe and Beaulieu (2021)[12] introduced a novel approach to 3D k-space sampling known as "Yarnball" that is a direct, more efficient alternative to both 3D radial and 3D cones imaging. Akin to its name, the "Yarnball" technique winds through k-space in a similar manner to winding a ball of yarn; starting from the center of k-space and following a straight radial path for some distance, then winding around the z-axis with constantly changing angles. For a single trajectory, r is defined as the relative distance from the center of k-space (r = 1 at k_{max}), Rr is the distance from the center of k-space normalized by number of k-space steps, and Rṙ is the rate of radial evolution of k-space steps per unit of time. The distance that the straight radial path from the center of k-space is dictated by ρ, where ρ is a specific radial value along r. Every step in k-space past this threshold distance results in the azimuthal (θ, or x-y plane angle) sweeping from 0 to π, and for every azimuthal angle step the polar angle (φ, or y-z plane angle) evolves 2π. These angular relationships are defined in equations 1.6 and 1.7, and a pictorial representation of a single-shot trajectory is seen in Fig. 1.12:

$$\dot{\theta} = \pi R\dot{r} \tag{1.6}$$

$$\dot{\varphi} = 2\pi Rr\dot{\theta} \tag{1.7}$$

Where both $\dot{\theta}$ and $\dot{\varphi}$ are azimuthal and polar angular evolution, respectively.

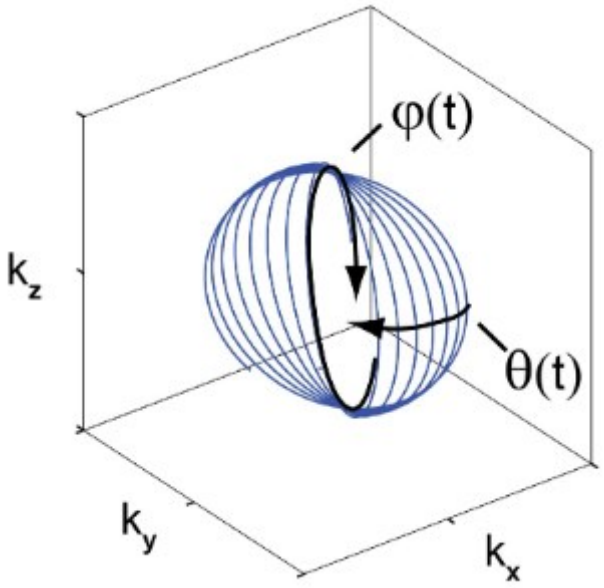

Figure 1.12[12]**:** *Example Single Yarnball Trajectory*[12].

Full sampling of k-space is be achieved by introducing multi-shot or multiple trajectory YB, where the number of YB trajectories required is dictated by the azimuthal evolution $\dot{\theta}$ and matrix radius Rr. If each trajectory is uniformly radially distributed, then the winding of each "rotating disk" trajectory will cause spiral-interleaving between trajectories in both the azimuthal and polar dimensions. Both the azimuthal and polar angle evolution rates can be reduced in proportion to the number of discs, $Ndiscs$, and spokes per disc, $Nspokes$, via a relationship described in equations 1.8 and 1.9:

$$\dot{\theta} = \frac{S\pi R\dot{r}}{Ndiscs} \tag{1.8}$$

$$\dot{\varphi} = \frac{S2\pi Rr\dot{\theta}}{Nspokes} \tag{1.9}$$

Where S is the "spin parameter", and dictates over-sampling or under-sampling. The radial sampling density (number of samples within a thin spherical shell) can be uniformly distributed across k-space if radial evolution is dictated by equation 1.10:

$$R\dot{r} = \frac{p^2}{r^2} \tag{1.10}$$

To critically sample k-space to the radial fraction ρ, $\rho 2\pi R$ spokes/disc and $\rho \pi R$ discs are needed, yielding equation 1.11:

$$Ntraj = Ndiscs * Nspokes = \rho^2 2\pi^2 R^2 \tag{1.11}$$

The most efficient and evenly sampled trajectories maintain a relationship of $Nspokes = 2Ndiscs$. Treating equations 1.8 – 1.10 as differential equations can yield solutions for $Ndiscs$ and $Nspokes$, which can subsequentially be used to solve for ρ in equation 1.11. In essence, the goal is to maintain proper radial sampling to the threshold distance of ρ, and beyond this distance wind the trajectory through k-space in such a manner that constant, critical sampling density is maintained. An example of a fully realized YB implementation is shown in Fig. 1.13.

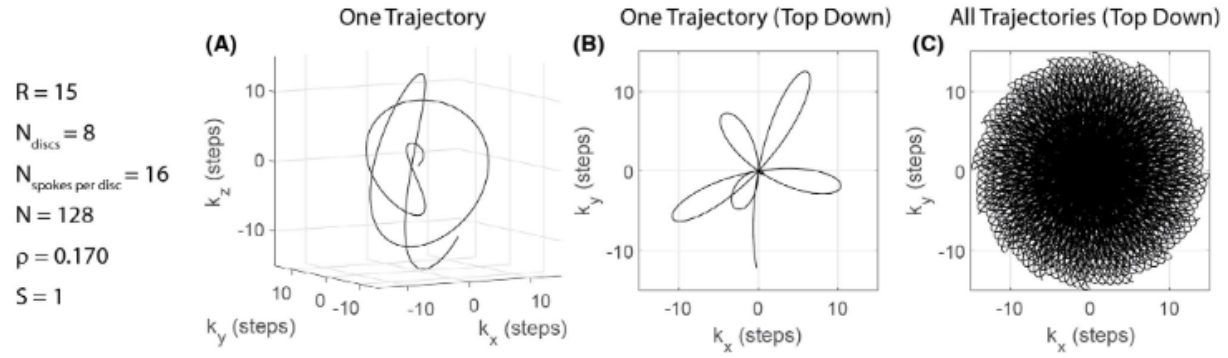

Figure 1.13: *Example Yarnball k-space sampling*[12].

Reducing ρ can result in very large reductions in number of trajectories needed, as there is more k-space sampling per trajectory (more loops). This increases the efficiency of the sampling greatly, and can minimize scan duration. However, the reduction in ρ is limited by the fact that increasing the number of loops will increase gradient slew rate, leading to hardware and physiological (peripheral nerve stimulation) constraints. For similar reasons, increasing the FOV or the spatial resolution of the image will also require more trajectories. While increasing readout duration enables greater k-space sampling and thus a reduction in trajectory number, leaving readout duration too long introduces issues with signal decay due to T2* effects and higher

potential of off-resonance artifacts. In the context of lung imaging, attempting to leave readout times too long will quickly introduce heavy smearing and ringing effects into the final image, potentially interfering with accurate image quantification. YB having higher sampling density and more efficient trajectories than traditional Cartesian sampling techniques enables larger FOV's at sufficient spatial resolutions.

1.3.4: Image Reconstruction and Processing

YB k-space sampling techniques inherently addresses 4 of the major challenges that must be overcome to perform 3D lung MRI: 1. Reduction in T2* effects caused by magnetic susceptibility differences at the lung-air interface (via use of UTE) 2. Efficient signal acquisition to minimize scan times 3. Elimination of cardiac motion artifacts (via oversampling of the center of k-space causing diffusion or smearing of motion artifacts across whole image) and 4. Sufficient FOV to cover the entire torso and lungs (via high sampling density and trajectory efficiency). Use of chest and back RF coils can aid the UTE YB sequence in obtaining an adequate amount of signal to properly image the lungs. The remaining major obstacles to clear include management of respiratory motion and associated motion artifacts that it causes, resolving varying B1 receive and transmit inhomogeneity, generating a signal reference to relate obtained signal within the lungs to total water content, and proper segmentation of the whole lung and lung parenchyma from surrounding tissue to obtain accurate lung water density quantification. All of the above listed obstacles will be tackled in the image reconstruction/processing stage of the imaging pipeline.

1.3.4.1: Respiratory Motion and Navigator Signal

Lung imaging must account for the complex three-dimensional motion of the boundaries of the lungs (diaphragm and chest walls that drive the motion) and the heart and blood vessels throughout the lungs. The most simplistic answer is to instruct the subject being scanned to hold their breath (either at maximal inhalation volume or maximal expiration volume) for the duration of the scan. UTE YB is capable of completing a full isotropic image in <10 seconds, a breath-hold length most patients are capable of performing. However, breath-hold positions are highly variable depending on the subjects selected lung volume at which they perform the hold and some patients with lung disease (e.g. severe pulmonary edema with heart failure) may have difficulty with any breath-hold. Respiratory navigator techniques exist to compensate for respiratory motion during free-breathing, including the use of external respiratory monitoring devices, navigator echoes such as "pencil beams", or sub-second self-navigator scans detecting diaphragm position to trigger sequencing[49]. However, these require complex custom modification of the MRI code and could interrupt the MRI signals steady-state, leading to artifacts and reduce efficiency.

A useful property of the oversampling of the center of k-space is that it represents the mean signal of the image (zero frequency component or DC signal). Larger lung volumes following inspiration (FRC+TV) will push the highly proton-dense abdominal organs down and out of the FOV, resulting in fewer total proton spins and thus lower total signal than end expiration (FRC). As such, the center of k-space can be used to extract respiratory information in the form of a retrospective (continuous data collection with subsequent "binning" of respiratory phases) self-navigator. Plotting the navigator signal obtained from data of every trajectory (i.e. every readout starts at the center of k-space) in the sequence and applying a band-pass frequency filter, to remove high frequency information, gives a full-scan-time self-navigator signal that serves as an estimation of respiratory motion[72]. Using a Gaussian weighting approach, each trajectory is "binned" into one of the user-specified number of respiratory phases (where 0% = FRC, 50% = FRC+TV of a breathing cycle). Specifically, the weighting of each k-space acquisition at a given respiratory phase is determined by its phase (i.e. 0 to 100% of a respiratory cycle) relative to the targeted phase, with a Gaussian weighting (i.e. less weight as the phase is

further from the target, according to a Gaussian function). Implementing the YB sequence in a "golden ratio" fashion, such that each trajectory is not played out in a sequential manner but rather in step sizes of $S \approx Ntraj/\phi g$, (golden ratio, $\phi g \approx 1.618$)[73], ensures uniform and pseudo-random coverage of k-space across each respiratory phase. The free-breathing YB trajectories implemented within this study used 20 respiratory phases to balance sufficient respiratory sampling and avoiding respiratory motion blurring.

It is important to remember that the use of chest and back coils will mean that coils in different positions will experience different variations in DC signals due to respiratory motion (e.g. a coil directly on the chest will have larger DC variations than a coil on the shoulder). To correct for this spatial variation between coils, principle component analysis (PCA) can be performed to on the DC navigator signal across all coils. PCA is a data reduction method that combines and amplifies the most correlated data across multiple information sets, while simultaneously suppressing noise and outliers in the samples[74]. The result is one single weighted navigator signal that describes the real-time evolution of a subjects breathing patterns over the length of a full scan.

Once DC signal combining and respiratory binning has been completed, a gridding algorithm can be implemented (sampling-density compensation[75] followed by Inverse Fourier Transform[64]) on the raw data, giving the ability to reconstruct 3D isotropic images with 20 unique respiratory phases. Thus, one of the 4 remaining obstacles for lung MRI has been addressed, the effects of respiratory motion.

1.3.4.2: Coil Combination via SUPER

The use of chest and back array coils with RF receive capabilities serves to greatly increase the amount of acquired signal[76]. Each coil can have an image reconstructed from the acquired data; Within each unique image, the SNR in pixels very close to the coil will be much higher than the SNR in pixels further away from the coils. At any given spatial location, all coils used in data acquisition will contribute some information to that location; coils close to the location will contribute high SNR images, while coils further away from that location will contribute mostly noise. This concept of spatial variation in SNR caused by the coils is known as

coil shading or a coil sensitivity map, and must be considered to create high-quality, uniform images from multiple receive coils.

The sum-of-squares methodology can estimate coil spatial information, but introduces SNR loss, signal bias, and does not suppress artifacts[77,78]. The summation using profiles estimated from ratios (SUPER) method extends the sum-of-squares methodology for coil spatial information by making three assumptions: 1. A low-pass smoothing filter will reduce the noise to near negligible levels 2. Underlying coil profiles are preserved through the smoothing process and 3. Systemic errors (such as motion artifacts) are negligible. When compared to traditional sum-of-squares methodology, the addition of the low pass filter was shown to reduce noise fluctuations in the coil mapping estimations, reduction in signal biasing, and an overall reduction in noise levels, particularly in areas of low SNR. Given the large FOV required in lung imaging, accuracy in coil combining the medial pixels (low SNR lung parenchyma) is essential, and as such, the SUPER approach is used in this study[77].

1.3.4.3: Normalization

Following SUPER coil combination, the images are still affected by B1 field inhomogeneity, both excitation and reception, that will cause a non-uniform variation in signal intensity throughout the subject (particularly in the large FOV required in lung imaging). Fig. 1.14 below shows a SUPER coil-combined reconstructed image, and highlights the need for further image processing to achieve accurate lung water quantification. Furthermore, the units of an MR image remain arbitrary (au), and the need for conversion into water density units persists.

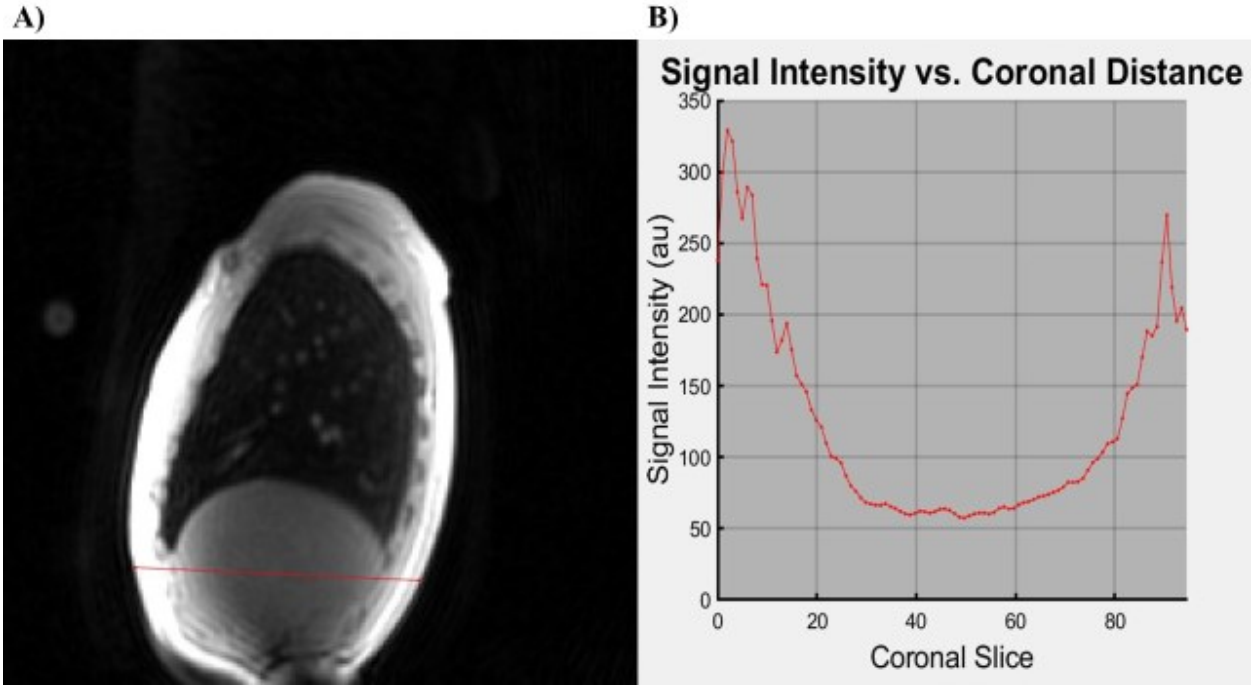

Figure 1.14: A) *Example free-breathing Yarnball image, coil-combined using SUPER coil-combination, respiratory resolved showing FRC, sagittal slice #91 of 217. There is a red-line manually drawn through the lower section of the torso, with signal intensity (au) vs chest-to-back distance plotted in* **B)**. *The lower section of the torso at this sagittal slice should have a mostly uniform signal intensity (i.e. if signal depended only on water content), yet there is a clear signal drop in pixels further from the coil arrays. This highlights the need B1 field mapping.*

A normalization process described by Meadus et al (2021)[5] aims to both adjust for the inherent B1 transmit/receive inhomogeneity map as well as provide an estimation for quantification of lung water. Two assumptions are made in the process: Firstly, all solid tissue surrounding the lungs (liver, skeletal muscle, blood pools, and the myocardium in the heart) are assumed to contain 70-80% water densities, based off of results from several prior studies[79–81]. Secondly, the main modulator of signal intensity variations over space is due to B1 field inhomogeneity[5]. If both assumptions hold true, then the solid tissue surrounding the lungs can be used as a subject-specific global signal reference.

A low spatial frequency map can be fitted to the reference tissue via application of a MATLAB function authored by John D'Errico called "gridfit" (2016)[82] in a slice-wise manner (i.e. in separate 2D chest-to-back slices). Application of the "gridfit" function in a 2D manner is done to measure signal variations in the chest-to-back direction caused by the naturally occurring LWD gradient[5–7], and are sub sequentially combined into one smooth 3D surface. The smoothing

process of this function acts to eliminate spatial variations in signal caused by B1 field inhomogeneity. This reference surface, however, contains a large region of missing data caused by the masking of the lungs (section 1.3.5 below), which results in undetermined solutions to the linear algebra equations that the "gridfit" function calculates to generate the smooth surfaces. This issue is resolved by interpolating the pixels within the lung mask via the Tikhonov regularization method[83], with optimal surface smoothness (balance between over-smoothing the interpolated data and error in the original data) being determined by the L-curve method[84] (as previously describes by Meadus et al.[5]), completing the 3D normalization map.

The signal of all tissues within the original reconstructed YB image can be divided by the now completed normalization map; division serves to both remove the spatial variations in signal caused by B1 field inhomogeneity and to normalize pixels within the lungs to the reference tissues, yielding pixel intensities in units of rLWD (%) across the entire torso. An example normalized image and its signal intensity profile is seen in Fig 1.15. Two of the remaining three challenges to quantitative lung MRI have been eliminated.

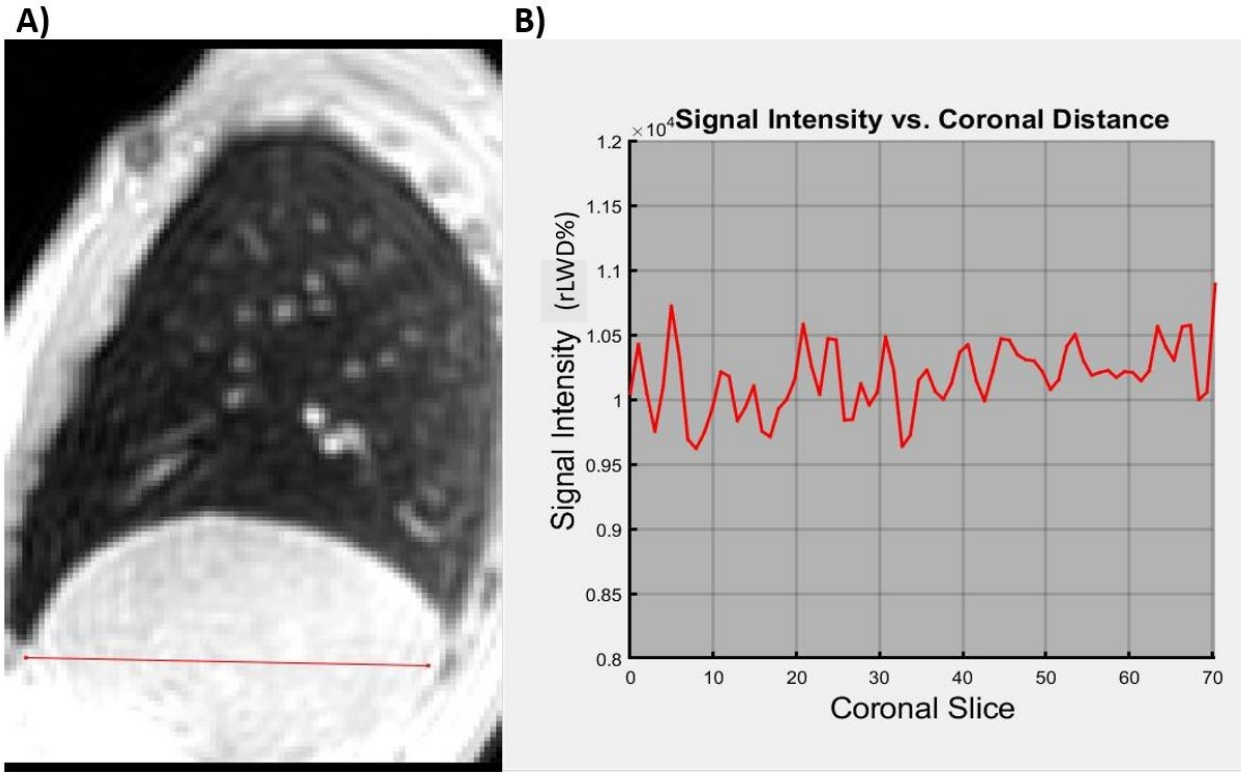

Figure 1.15: A) *B1 field corrected, normalized 3D isotropic lung MRI (same subject as Fig. 1.13). The sagittal view provided here is approximately the same sagittal position as* **Figure 1.14 A)** *above, though it is cropped to center more closely on the torso. Normalized sagittal slice #39 of 142, at FRC. Image is now in rLWD% units, with the solid tissue outside the lungs expected to ≈100%. (Note that the units are set to 10,000, which corresponds to 100%, which enabled 16-bit representation to save memory). A red line is drawn through the lower torso with* **B)** *signal intensity (rLWD%) plotted vs chest-to-back distance. Note that the variation in signal intensity in the chest to back direction through the solid tissue outside the lungs is significantly more uniform than is seen in* **Figure 1.14 B)**.

1.3.5: Image Segmentation (Including Vasculature)

Without reliable lung segmentation, proper calculation of the normalization map, lung volumes and rLWD would be not be feasible. Furthermore, the datasets obtained in these 3D isotropic images contain ~ 75-90 chest-to-back slices (depending on the size of the subject) across 20 respiratory phases, which would mean at least 1,500 images per subject that require segmentation. Performing this task by hand would take far too long and is impractical; as such, the need for a quick and highly accurate automated approach to lung segmentation is required. Meadus et al (2021)[5] proposed an semi-automatic "region growing" segmentation method that

had high reproducibility, however, it required a small amount of user input causing some variability in results, and had decreased performance at the smaller/more complex lung vasculature.

To remove user input from the pipeline and increase vascular segmentation and overall lung masking performance, a deep learning framework was developed in house at the University of Alberta and applied to the YB UTE lung MRI pipeline. The deep learning framework that was selected is known as "nnU-Net" or "U-Net like" architecture, and was selected due to its robustness when it comes to biomedical imaging segmentation[85]. In short, the nnU-Net deep learning algorithm follows the general U-Net framework, however, characteristics from the provided datasets are pre-assessed in the form of a "data fingerprint" (image voxel size, typical image shape and size, signal intensity distribution, etc.), and used to help infer the U-Net training parameters (batch size, network topology, patch size, etc.)[85]. Visually validated parenchyma masks (which were generated using the previously mentioned semi-automatic region growing algorithm) were manually selected and inputted as training sets into the semi-supervised nnU-Net model. The masks were passed through a high pass filter for the purpose of increasing vascular region brightness and enabling vascular thresholding to further refine the parenchyma mask. Separately, a Chan-Vese active contour mask[86] was implemented as a method of defining a total lung volume mask; subtracting the refined parenchyma mask from the Chan-Vese mask yields a lung vasculature mask. Finally, the semi-automatic region growing algorithm was applied to the normalized reference tissue mask for the purposes of further refining the final reference mask. The end result of this process is a 5-compartment mask that contains the right and left lung parenchyma mask, the right and left lung vasculature mask, and the reference tissue mask. These 5-compartment masks trained the nnU-Net model to be capable of performing automatic multicompetent segmentation of new cropped YB UTE images. A visualization of this nnU-Net model framework is seen in Fig. 1.16[87].

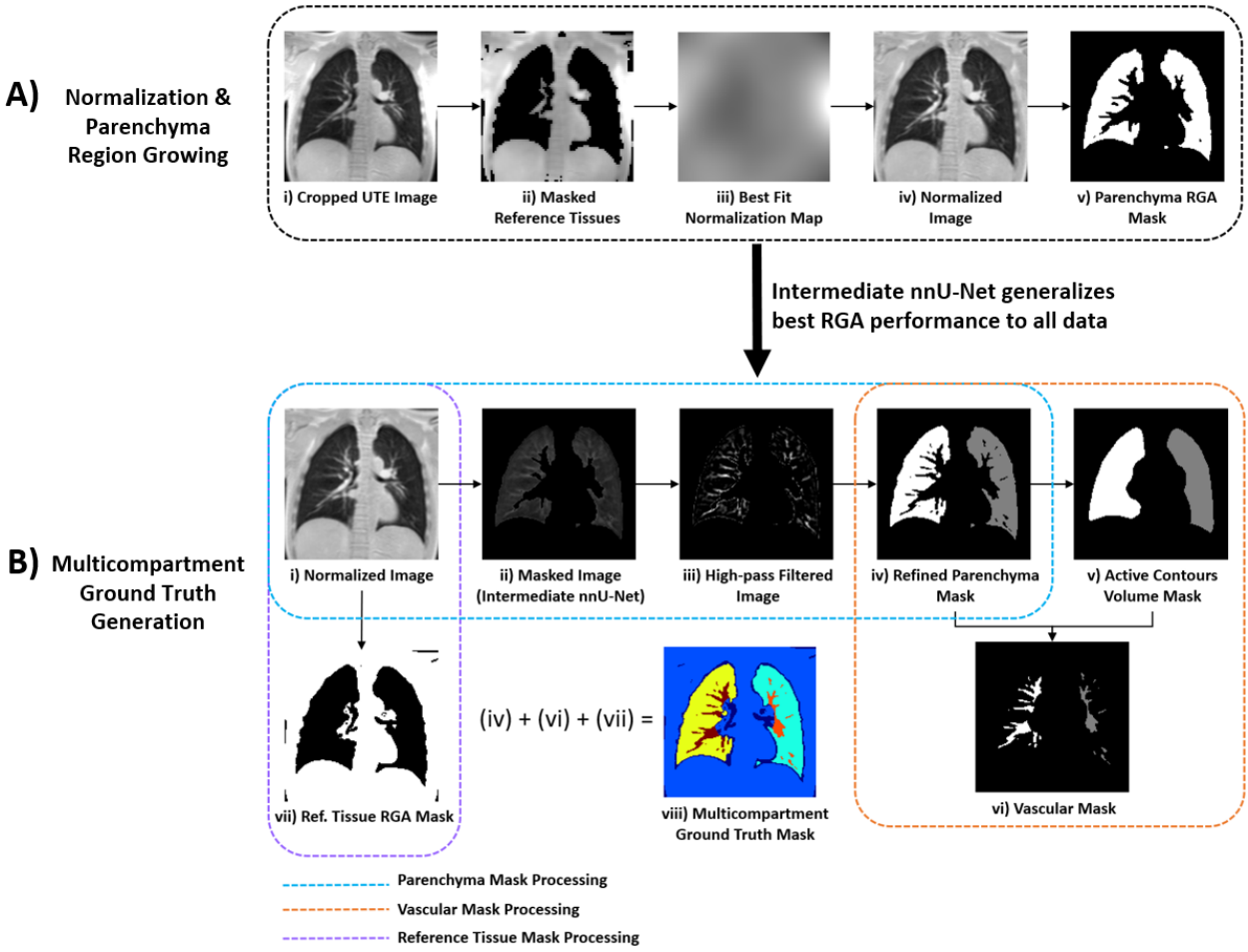

Figure 1.16: A) *Masking as described by Meadus et al (2021)*[5] *and normalization as described above.* **B)** *nnU-Net learning pipeline. Image courtesy of Christopher Keen, University of Alberta Graduate Student.*

With a robust segmentation method in hand, we have now cleared all of the major obstacles to quantifiable, 3D isotropic free-breathing lung MRI. Further examples of the resulting lung images and parenchyma masks are displayed throughout section 1.4 and section 2.

1.3.6 Estimation of SNR

Measuring SNR in the presence of coil-combining methods becomes more complicated than without, as each coil contributes a different amount of noise to each pixel. The most accurate method of measuring SNR in the presence of multi-coil imaging is to obtain a "pre-scan

noise" image, which is an image acquisition without any RF gradients or excitation applied, and apply the same image reconstruction and normalization pipeline described above. The scaled noise image can be used to calculate SNR, as described as Kellman et al (2005)[88]. Meadus et al (2021) applied this methodology, and showed good SNR in UTE free-breathing YB (SNR ≈ 10-20)[5].

In this study, a very similar UTE YB sequence to Meadus et al. is used, therefore it was assumed that SNR would remain strong enough (>10) to properly image the lung parenchyma, and the choice was made not to include a pre-scan noise image. While this study will use a very similar UTE YB as Meadus et al, some optimizations of the sequence parameters will be performed (section 1.4). As will be detailed, the optimal sequence had an increase in FOV, lower spatial resolution and several signal averages , and thus it is assumed that the final version used in this study maintains good SNR (≥ 10)[89].

1.4: Optimization of Yarnball

Meadus et al (2021)[5] demonstrated the ability of YB UTE MRI sequencing to obtain good SNR, 3D images of the lungs in both a breath-hold and free-breathing scenario. This study aims to improve upon the sequencing performed by Meadus et al (FOV of 300 mm in all directions, 2.5 mm x 2.5 mm x 2.5 mm voxel size, 1.3 ms readout-time. TE = 70 μs, TR = 3.54 ms, 7381 projections, 130 seconds scan time (5 averages))[5] with the goal of reducing scan time and maintaining analyzable images (i.e. maintaining rLWD quantification). Readout time, voxel size, TR, FOV, and number of averages were all changed in a step-wise manner of testing in new YB sequences, with number of trajectories changing accordingly to maintain safe slew rate operation. These sequences were tested on in-house volunteers, with qualitative and quantitative measurements of the results being used to determine the most "optimized" version of the YB sequence.

1.4.1: Development of a Faster "Reference" Sequence

In order to achieve useful information regarding changes in rLWD% and lung volume over time after supine positioning, reductions in scan time are needed. A sequence was designed with similar parameters as Meadus et al[5], however, the number of trajectories was reduced by over half (7381 to 3362), allowing for shorter scan times and an increased number of averages taken to ensure full respiratory sampling. Voxel size (3.0 mm in all directions), FOV (350 mm in all directions) and readout length (1.5 ms) were altered. Each average took 9.68 s to fully sample k-space, and 15 averages were used for a total of 145 seconds of scan time. The resulting normalized images (Fig. 1.17) were of similar quality as Meadus et al, and similar values for global rLWD% were calculated. Furthermore, a signal drop appeared in the left distal lung region in both subjects (Fig. 1.18), an inaccuracy that will be explored in section 1.4.3.

Figure 1.17: *Example normalized UTE Yarnball lung MRI acquired in free-breathing conditions. Slice #51 of 79 shown at FRC respiratory phase. FOV = 350 mm, VOX = 3.0 mm, readout time = 1.5 ms, 15 averages, 9.68 s/average (145 s total scan time). Reference tissue ≈ 70%-80% rLWD. Lung parenchyma contains roughly 20%-40% rLWD.*

This lower trajectory, faster YB sequence will serve as the "reference point" scan when further testing YB sequence variations.

1.4.2: Variation in Readout Time

Sampling efficiency of YB sequencing is increased with longer readout times[12]. YB sequences with readout durations of 2.0 ms, 2.5 ms and 3.0 ms were designed with the same FOV and scan time, and changes in voxel size/number of trajectories to maintain safe operation (Table 1.1).

Table 1.1: *Variation in Readout Length (Free-Breathing)*

Readout Time (ms)	VOX (all directions), (mm)	FOV (all directions), (mm)	TR (ms)	# Traj	# Averages	Time/Ave (s)
2.0	2.63	350	3.54	2888	15	10.24
2.5	2.38	350	4.04	2312	15	9.34
3.0	2.20	350	4.57	2048	15	9.36

Increasing readout duration to 2.0 ms and above created "rippling" artifacts that distorted the overall quality of the lung image, likely caused by a combination of increased smearing and off-resonance effects[12] that can occur when readout time is increased.

Given the poor results from the first test, a second set of sequences were developed with readout duration being varied from 1.0 ms – 2.0 ms, with 0.1 ms increments in each sequence tested (Table 1.2). In order to achieve the quickest possible scan, the lowest number of trajectories that allowed for safe slew rates was used, with minor adjustments made to TR to keep relatively similar scan lengths. This trial was performed using breath-holds for faster experimentation/computation time.

Table 1.2: *Variation in Readout Length, Second Trial (Breath-Hold)*

Readout Time (ms)	VOX (all directions), (mm)	FOV (all directions), (mm)	TR (ms)	# Traj	Time/Ave (s)
1.0	3.0	350	2.36	5832	13.76
1.1	3.0	350	2.45	5202	12.74
1.2	3.0	350	2.56	4608	11.80
1.3	3.0	350	2.67	4050	10.81
1.4	3.0	350	2.77	3698	10.24
1.5	3.0	350	2.87	3362	9.65
1.6	3.0	350	2.96	3200	9.47
1.7	3.0	350	3.08	2888	8.90
1.8	3.0	350	3.17	2738	8.68
1.9	3.0	350	3.27	2592	8.48
2.0	3.0	350	3.36	2450	8.23

Artifacts caused by longer readout duration, as described above, continued to be present at readout times of 1.7 ms and above. Overall image quality appeared to improve as readout times decreased, with blood vessels becoming more clear and distinct from lung parenchyma at the lowest readout times. However, at roughly 1.2 ms, it became exponentially more inefficient to decrease the readout time ($Ntraj$ increased by 1228 from 1.2 ms to 1.0 ms) compared to longer readout times ($Ntraj$ increased by only 688 from 1.5 ms to 1.3). There was not a significant change in calculated global rLWD% for all readout lengths of 1.5 ms and below. As a result, a readout time of 1.3 ms was selected as the best balance between overall image quality and efficiency.

The sequences with readout times of 1.0 ms, 1.3 ms, and 2.0 ms were tested at free-breathing (15 averages) to confirm the above findings.

1.4.3: Variation in TR

The new sequences experienced a signal drop along the anterior-distal region of the left lung (Fig. 1.18). It was theorized that increasing TR may eliminate the existence of this signal drop. As such, the 1.5 ms readout sequence from section 1.4.2 was repeated at breath-hold eight additional times with various TR lengths (TR = 5.87 ms, 4.87 ms, 3.87 ms, 3.17 ms, 2.97 ms, 2.92 ms, 2.90 ms, 2.88 ms).Given the initial sequence required (TR = 2.87 ms), the above tests correspond to a "TR delay" of 3 ms, 2 ms, 1 ms, 100 μs, 50 μs, 30 μs and 10 μs, respectively.

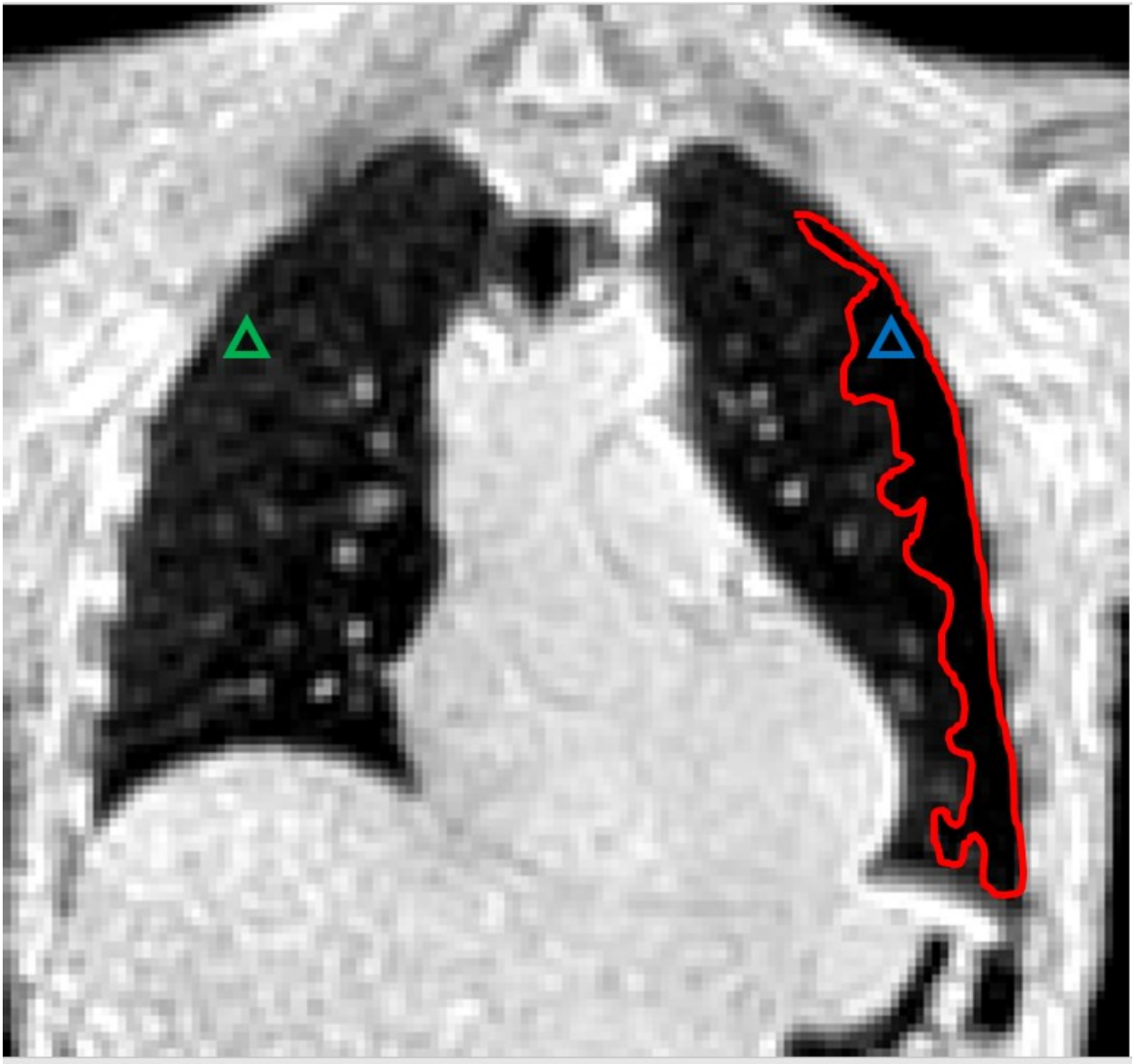

Figure 1.18: *Signal drop (red) along anterior-distal portion of the left lung. A region within the area of signal drop (blue triangle) has a mean signal intensity of ~53% the mean signal intensity in a similar region in the right lung (green triangle). Image is slice #30 of 86 taken at breath-hold. See Table 1.2 for full trajectory information (readout = 1.5 ms).*

It was determined that TR delay of 50 μs and below were unsuccessful at eliminating the area of signal drop, while all TR delays of 100 μs and above were successful. A possible source for this signal drop could arise from eddy currents disrupting the local magnetic fields. The rapidly switching gradients that are required to complete the 3D YB imaging could be the cause of these eddy currents; applying a TR delay and giving the sequence more time for these

unwanted eddy currents to dissipate would explain why a TR delay eliminates the signal drop. All scans moving forward will contain a TR delay of 100 μs to compensate for the signal drop.

1.4.4: Variation in Voxel size

Variation in isotropic spatial resolution can have large implications on overall image quality and potentially the robustness of the quantification of lung water. If minimum SNR requirements are met within each voxel, a smaller voxel size will result in more fine, crisp looking images. However, increasing spatial resolution inherently increases slew rate; a trade off in increased number of trajectories is required with increased spatial resolution in order to keep slew rates within safe operational range[12], sacrificing valuable scan time. Five different sequences of different isotropic spatial resolutions (2.5 mm – 3.5 mm, 0.25 mm steps) were designed and performed during free-breathing (Table 1.3). to examine the trade-off between image quality and number of trajectories.

Table 1.3: *Variation in Voxel Size (Free-Breathing)*

Readout Time (ms)	VOX (all directions), (mm)	FOV (all directions), (mm)	TR (ms)	# Traj	# Averages	Time/Ave (s)
1.3	2.50	350	2.88	6498	9	18.71
1.3	2.75	350	2.82	5000	12	14.10
1.3	3.0	350	2.77	4050	15	11.22
1.3	3.25	350	2.74	3200	19	8.77
1.3	3.50	350	2.69	2738	23	7.37

Increased spatial resolution resulted in the best image quality, with decreased ringing artifacts and sharp lung edges/small vasculature. However, increasing spatial resolution did not result in a significant change in calculated global rLWD%, while requiring significantly more

trajectories and thus longer scan times (2.5 mm scan took more than double the amount of time as 3.5 mm per average). VOX = 3.5 mm maintains high enough image quality to accurately calculate rLWD%. A decrease in spatial resolution (larger voxel volume) will increase SNR, thus maintaining good SNR status (≥ 10). Due to the above, the decreased spatial resolution of 3.5 mm (all directions) will be used in the final sequence.

1.4.5: Variation in Field of View

A reduction in FOV will reduce the minimum number of YB trajectories required to stay within safe operating limits[12] thus decreasing scan time. However, as discussed in section 1.2.6, a sufficient amount of bodily tissue surrounding the lungs must be imaged in order to obtain an accurate lung normalization map. Furthermore, sufficient enough FOV is required for a given individual to ensure "wrap-around" aliasing is avoided (in non-Cartesian sequences, this can often take the form of artifact bands that are diffused across the entire image) [90]. To determine optimal FOV, three sequences were designed at FOV = 300 mm, 350 mm and 400 mm in all directions and tested at breath-hold (Table 1.4).

Table 1.4: *Variation in FOV (Breath-hold)*

Readout Time (ms)	VOX (all directions), (mm)	FOV (all directions), (mm)	TR (ms)	# Traj	Time/Ave (s)
1.3	3.0	300	2.78	2888	8.03
1.3	3.0	350	2.78	4050	11.26
1.3	3.0	400	2.78	5202	14.46

FOV = 300 mm was not sufficient in capturing enough of the tissue surrounding the lungs, causing insufficient amount of reference tissue to be imaged and inaccurate calculations of rLWD%.. Furthermore, questions of wrap-around aliasing are introduced into the scan. In one extreme test, similar problems existed at FOV = 350 mm, however, are significantly less exaggerated than FOV = 300 mm and are very minor issues. FOV = 400 mm eliminates these

problems for the extreme case. Fig. 1.19 shows results at FOV = 300 mm (A and C) vs. FOV = 350 mm (B and D) for a typical test case. There was no significant difference in calculated global rLWD% between FOV 350 mm and 400 mm, while FOV 350 mm was ~3s/average faster than 400 mm. Larger FOV will increase the SNR; both FOV 350 mm and FOV 400 mm thus will maintain good SNR (≥10). It was decided that the fewer number of trajectories required for FOV 350 mm was more valuable than further increases in SNR, thus FOV of 350 mm (all directions) was selected for the final sequence.

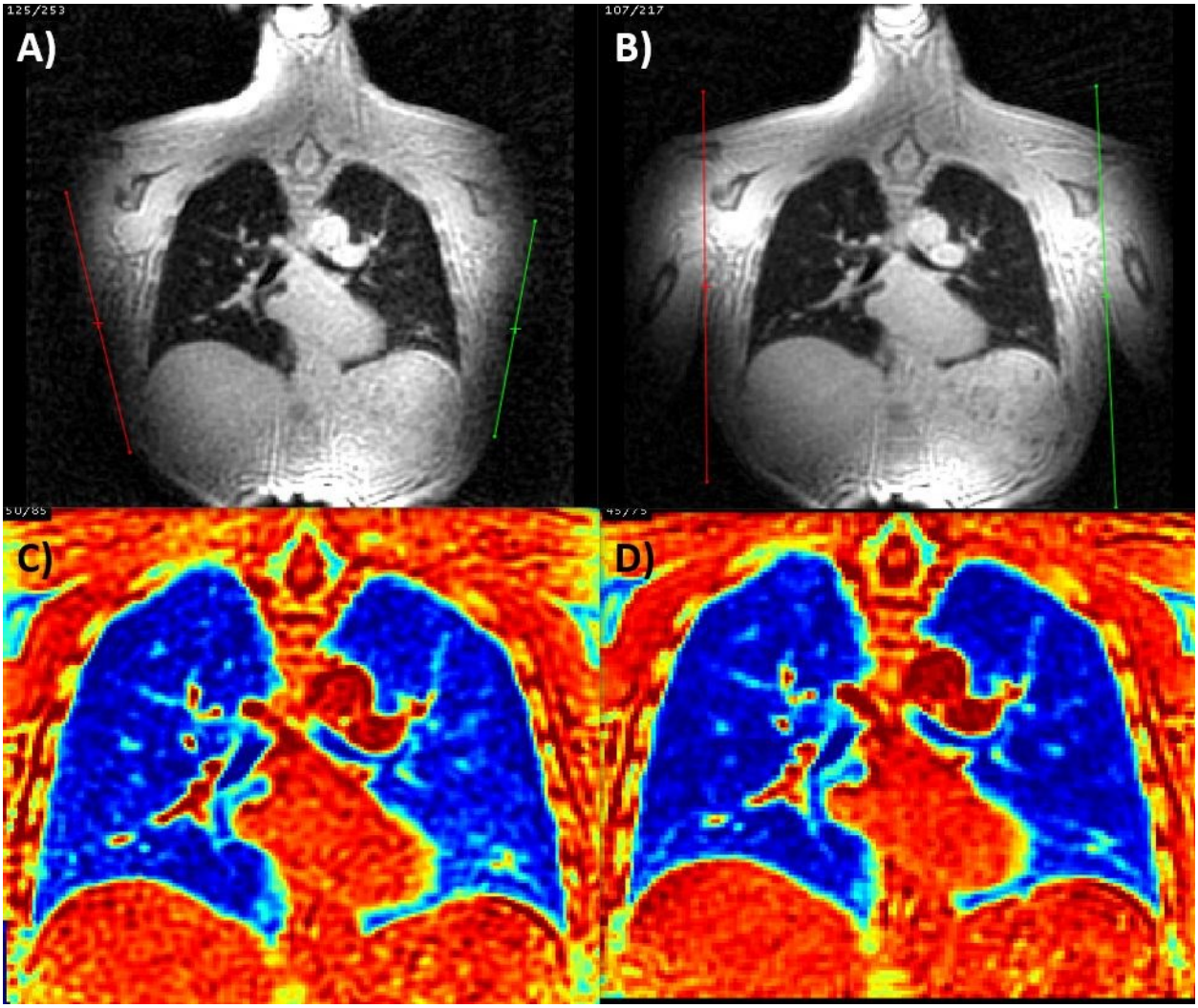

Figure 1.19*: SUPER images from variations in FOV in a volunteer.* **A)** *FOV = 300 mm,* **B)** *FOV = 350 mm (FOV = 400 mm not shown). The edge of the torso is missed at FOV = 300 mm, while FOV = 350 mm shows the entire torso with crisp edges (Red/Green lines). Resulting normalized images for FOV = 300 mm and FOV = 350 mm shown in* **C)** *and* **D),** *respectively. Normalization map outside the lungs is somewhat more uniform in FOV = 350 mm, and the resulting lung water density map is less noisy. Images taken at roughly the same slice, breath-hold. See Table 1.4 for full trajectory information.*

1.4.6: Variation in Averages Taken

An appropriate number of averages must be acquired in order to ensure all of the respiratory cycle is properly sampled (as described in section 1.3.4.1). Meadus et al[5] used 5

averages, however, they chose to separate into only 10 respiratory phases, which has a broader respiratory phase window and thus fewer phases required to be sampled than the 20 phases selected in this study. Fewer respiratory phases are more susceptible to blurring due different diaphragm positions in different respiratory phases overlapping significantly, particularly towards FRC+TV where the diaphragm is more rapidly moving. It was concluded that more averages would thus be required in this study to obtain 20 clear respiratory images; to determine how many averages this would require, the number of averages taken was varied from 9 - 23 (9, 12, 15, 19, 23) in the free-breathing variation of voxel size test at (Table 1.3).

9 averages caused very minor blurring at the diaphragm at the FRC+TV respiratory phase. This was resolved at averages 12 and above. Applying the readout time = 1.3 ms, FOV = 350 mm, VOX = 3.5 mm trajectory (Table 1.3) in one final free-breathing test scan with only 10 averages also generated respiratory images that were free of blurring artifacts at the diaphragm for FRC+TV (Fig. 1.20). Given that each average for this sequence takes 7.37 s to complete, it was advantageous to reduce the total number of averages taken from 12 to 10, saving nearly 15 seconds/average. In regards to SNR, we would expect SNR to be proportional to $\sqrt{\#\ averages}$[89], thus we have maintained good SNR (≥10).

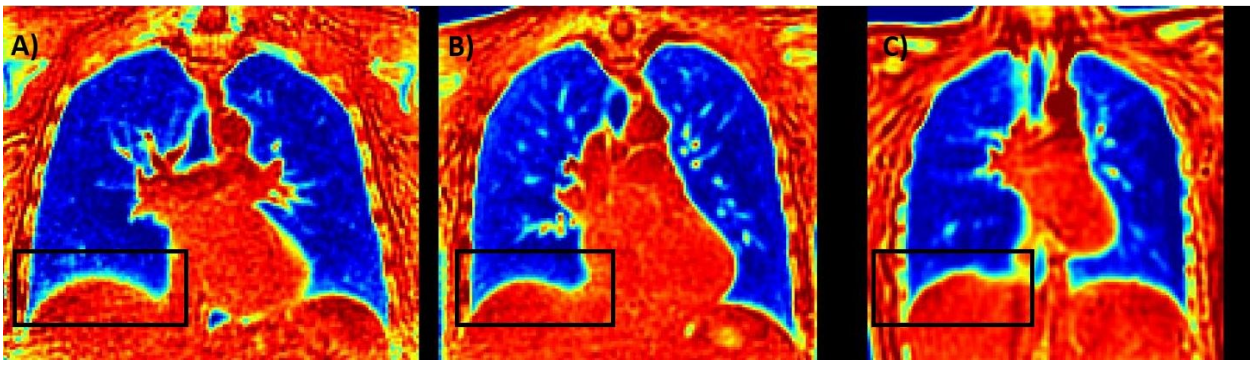

Figure 1.20: *Normalized images in scans with* **A)** *9 averages,* **B)** *12 averages and* **C)** *10 averages. Slight blurring occurs in 9 averages at the diaphragm, whereas 12 and 10 averages are free of blurring artifacts (black box). Images taken from three separate subjects are roughly the same slice, FRC+TV respiratory phase. See Table 1.4 (VOX = 3.5 mm) for full trajectory information.*

The final, "most optimized" sequencing parameters were determined to be as follows: readout time = 1.3 ms, VOX = 3.5 mm in all directions, FOV = 350 mm in all directions, TR = 2.72 mm, Ntraj = 2738, scan time/average = 7.4 s, 10 averages. These will be the sequence parameters used in the study outlined in chapter 2. Table 1.5 below outlines the difference in sequence parameters between Meadus et al (2021)[91] and the below study. With an increase in voxel volume, FOV, and an increased number of averages taken, we have ensured that good SNR is maintained.

Table 1.5: Differences in Sequence Parameters

Sequence Parameter	Meadus et al (2021)	This Study
Readout Time (ms)	1.3	1.3
Resolution (mm)	2.5	3.5
FOV (mm)	300	350
# Averages	5	10
# Respiratory Phases	10	20
Ntraj	7381	2738
TE (μs)	70	100
TR (ms)	3.54	2.72
Total Scan Time (s)	130	74

Chapter 2: Dynamic Changes in Lung Water Density and Volume Following Supine Body Positioning

The following chapter is an adapted version of a manuscript that has been accepted for publication in Magnetic Resonance in Medicine as a technical note.

2.1: Introduction

Pulmonary edema, or fluid accumulation in the lungs, is a primary feature of heart failure that is associated with clinical symptoms such as dyspnea and poor exercise capacity[2,3]. Elevated lung water density measured with MRI has been associated with reduced exercise capacity in heart failure[1] and also been shown to be predictive of clinical outcomes, even in the case of sub-clinical pulmonary edema[4]. Time-efficient three-dimensional UTE imaging methods designed for imaging of the lung parenchyma in combination with post-processing methods for signal normalization and segmentation now enable calculation of water-density-weighted lung images with breath-hold or short duration free-breathing acquisitions[5,6].

MRI studies of lung water typically take place with supine body positioning. The distribution of abdominal organs and thus lung volume is dependent on body position due to the effects of gravity[8,9] as is the distribution of blood and free water in the body[10,11]. There is shift of 300-500 ml of blood to the thoracic cavity with supine positioning[46,47,92] and well-documented differences in the chest to back gradient in lung water density for prone versus supine positioning, using MRI[6,7] and other modalities[93,94]. However, the time-course of changes in regional lung water density, lung volumes and total lung water content following patient positioning from upright to supine remain unknown[6,95].

The goals of the current study were to measure the changes in global and regional lung water density (rLWD) as a function of time after supine body positioning and their relationship with changes in lung volumes and total lung water content. We expect to determine the time

needed to achieve steady-state lung water distributions following supine positioning and if regional or total lung water content vary significantly over the duration of a typical MRI scan session.

2.2: Methods

2.2.1: Study Procedure and Subjects

Studies were completed in nine healthy volunteers (5 male, 4 female, 33.2±10.2 years (21-53 years), 1.72±0.05 m, 69.8±12.4 kg, Table 1) A health questionnaire was used to confirm all subjects have no known history of pulmonary or cardiovascular disease and with no current medications. This study was approved by the University of Alberta Health Research Ethics Board and written informed consent was given by all study participants. Serial three-dimensional water-density images of the lungs were acquired following supine body positioning. A timer was started with subject positioning on the scanner bed, followed by placement of the body array receiver coils and insertion into the scanner. A localizer scan was performed immediately, after which the lung water imaging acquisition was prescribed and started. The lung water acquisitions were repeated a total of 18 times over ~25 minutes, with the time after supine positioning recorded at the onset of each repeated scan. Three subjects repeated the procedure on a separate day with the addition of a total lung capacity breath-hold (10 seconds) at the half way time point. A nitrogen washout study for calculation of functional residual capacity (minimum lung volume during tidal breathing) was performed in three subjects, following supine body positioning. Measurements were completed upright and for 30 minutes following supine positioning at 5 minute intervals. For all studies, volunteers were instructed to breath normally over the entire scan duration with no other instructions. Additionally, a time-series of real-time images were acquired in a subset of three subjects on a separate day to provide independent assessment of changes in lung volumes following supine body positioning. Volunteers were instructed to breath normally over the entire scan duration with no other instructions.

2.2.2: Image Acquisition

All imaging data was acquired on a Siemens Prisma 3T scanner (Erlangen, Germany) using spine and body arrays (36 total coils) for signal reception to provide full torso coverage. Three-dimensional spin-density weighted lung images were acquired in a free-breathing acquisition using an optimized YB k-space trajectory[5]. Acquisition parameters: 350 mm field of view in all directions, TR = 2.72 ms, TE = 100 μs, 1.0-degree flip angle, readout time = 1.3 ms, voxel size = 3.5 mm x 3.5 mm x 3.5 mm (2mm interpolated reconstruction with zero padding), 2738 trajectories. Each full k-space acquisition was 7.4 seconds with 10 serial repetitions (averages) performed during free-breathing for a total acquisition time of 74 seconds per time point. The k-space trajectories were incremented in a golden-ratio manner to ensure that any subset of trajectories used for respiratory-resolved reconstructions (described below) included an even and pseudo-random distribution of trajectories throughout k-space. The use of short echo times (100 μs) and low excitation flip angle (1 degree) ensured minimal T2* and T1-weighting for proton-density weighting[5]. The complete 74 second scan is referred to as a single time step and was repeated 18 times in each subject with a 2 second delay between sequential acquisitions. All raw data was transferred off the scanner for processing with custom MATLAB software (The MathWorks Inc. Natick, Massachusetts). The study procedure was repeated in three subjects, with 11 datasets acquired immediately following supine body positioning (15 minutes' acquisition time), followed by a total lung capacity inspiration breath-hold of 10 seconds, and the acquisition of an addition 11 datasets following the breath-hold. On a separate day, real-time two-dimensional gradient-echo images were acquired in a subset of 3 subjects. For this experiment, formal calculation of normalization maps or rLWD% was not performed, but rather calculations of FRC lung volumes (using diaphragm positioning as a basic respiratory navigator) with an emphasis on obtaining images as fast as possible (hence 2D imaging rather than 3D). Acquisition parameters: 500 mm field of view with a coronal slice orientation, 128 x 128 matrix, TR = 2.3 ms, TE = 1.4 ms, 6-degree flip angle, 10 mm slice thickness, 3 slices, 300 ms per image with a total acquisition time of 24 minutes. For the GRE experiment, image acquisition used just the body coil for excitation and reception and began within 10 seconds of supine positioning.

2.2.3: Image Reconstruction and Image Processing

The image reconstruction and post-processing steps for each complete free-breathing acquisition (each time step) have previously been reported[5]. Briefly, a respiratory navigator signal was calculated using the center of k-space from each acquisition (every TR), which was used to assign each acquired k-space arm a respiratory phase with values of from 0% to 100% of a breathing cycle. Images at functional residual capacity (FRC, minimum free-breathing lung volume) were reconstructed using one of the ten repeated k-space arms for which the respiratory phase was closest to FRC (0% of breathing cycle), independently for each k-space arm. Similarly, images were reconstructed at 50% of the breathing cycle to approximate FRC + tidal breathing volume (FRC + TV, maximum free-breathing lung volume) using one of the ten repeated k-space arms closest to the targeted 50% respiratory phase. Acquisitions included 10 repetitions of each k-space arm to provide respiratory phases near FRC (0% respiratory phase) and FRC+TV (50% respiratory phase) for each arm. All image data within each respiratory bin was then averaged into one final image for each respiratory phase, for a total of 20 respiratory images per 74 s scan. Following data selection for image reconstruction at FRC and FRC+TV, raw data was sampling-density compensated[75] to a beta = 2 Kaiser k-space filtering shape with zero padding to the final 2 mm pixel size in each dimension. Images were then constructed using standard gridding methodology[64] and the coil elements combined with the SUPER approach[77].

Reconstructed images were normalized to units of relative lung water density (rLWD) using a previously described and validated approach that corrects for signal intensity variations over space from B_1 transmit and receive coil inhomogeneity[5]. Briefly, this method uses a best-fit low spatial-frequency signal intensity correction map that is calculated using all solid tissues surrounding the lungs, including the liver, heart, skeletal muscle, blood and spinal column. Division by the correction map normalizes all reference tissues to unity and the lung parenchyma to units of water density relative to the surrounding reference tissues. rLWD is reported in units of percentage, relative to the reference tissues.

The lung parenchyma was segmented using an in-house nnU-Net machine learning algorithm.[85,87] Five segmented regions included one for the reference tissue (all solid tissues

outside the lungs), and separate masks for the lung parenchyma and vascular pool, with unique identification of right and left lungs (Fig. 2.1B and C). Total lung volume was calculated as the total number of lung pixels (parenchyma plus vascular) multiplied by the voxel volume. Water volume in each region was calculated as the sum of rLWD values in the masked region (percentage values were divided by 100 to change units to a fraction) multiplied by the voxel volume, separately for the parenchyma, vascular and total lung regions. All parameters (rLWD, lung volume and lung water volume) were calculated at each of the 18 time points at FRC and FRC+TV respiratory phases. Tidal volume was calculated as the difference between minimum and maximum lung volume. The same image processing pipeline (FRC analysis only) was employed for the additional 3 subjects with 11 time steps (15 minutes) after supine positioning and 11 additional time steps following the total lung capacity breath-hold.

Continuous variables were expressed as mean±standard deviation. Paired Students T-Tests were used to analyze differences in average rLWD, lung volume and lung water volume over time (1^{st} scan vs 18^{th} scan) and differences between all values at the two respiratory phases. P-values < 0.05 were considered statistically significant. Repeatability of rLWD, lung volume and lung water volume was calculated using images from time-step 17 and 18 in each subject, calculated as intraclass correlation coefficients (ICC) and displayed using Bland and Altman plots.

For gold-standard calculation of FRC during normal tidal breathing, the non-MRI study of the nitrogen wash-out technique was performed as per guidelines[14]. Briefly, participants were situated in front of two mouthpiece's and instructed to breath at normal tidal volume. Importantly, prior to initiating each maneuver, participant tidal breathing nitrogen concentration was confirmed to be at baseline level (~78%) to ensure no "spill over" from repeat maneuvers. Once stability of tidal breathing was reached, participants were instructed to inhale through the mouthpiece that is outputting 100% oxygen and exhale through the outtake mouthpiece, while maintaining tidal breathing and performing multiple breaths. The volume of nitrogen exhaled as well as the concentration of nitrogen within each exhaled breath are measured, with FRC calculated as the difference between nitrogen volume exhaled and nitrogen volume within the tissue, divided by the difference in nitrogen concentrations within expelled air before the washout and at the last breath

of the test. The test was terminated when the expired gas contained less than 1.5% nitrogen for three consecutive breathes.

The lung cross-sectional areas from real-time gradient-echo images was measured over the 24-minute study duration, with extraction of minimum lung areas over 55 second intervals to capture the FRC respiratory phase. Right and Left lung areas were summed for each slice.

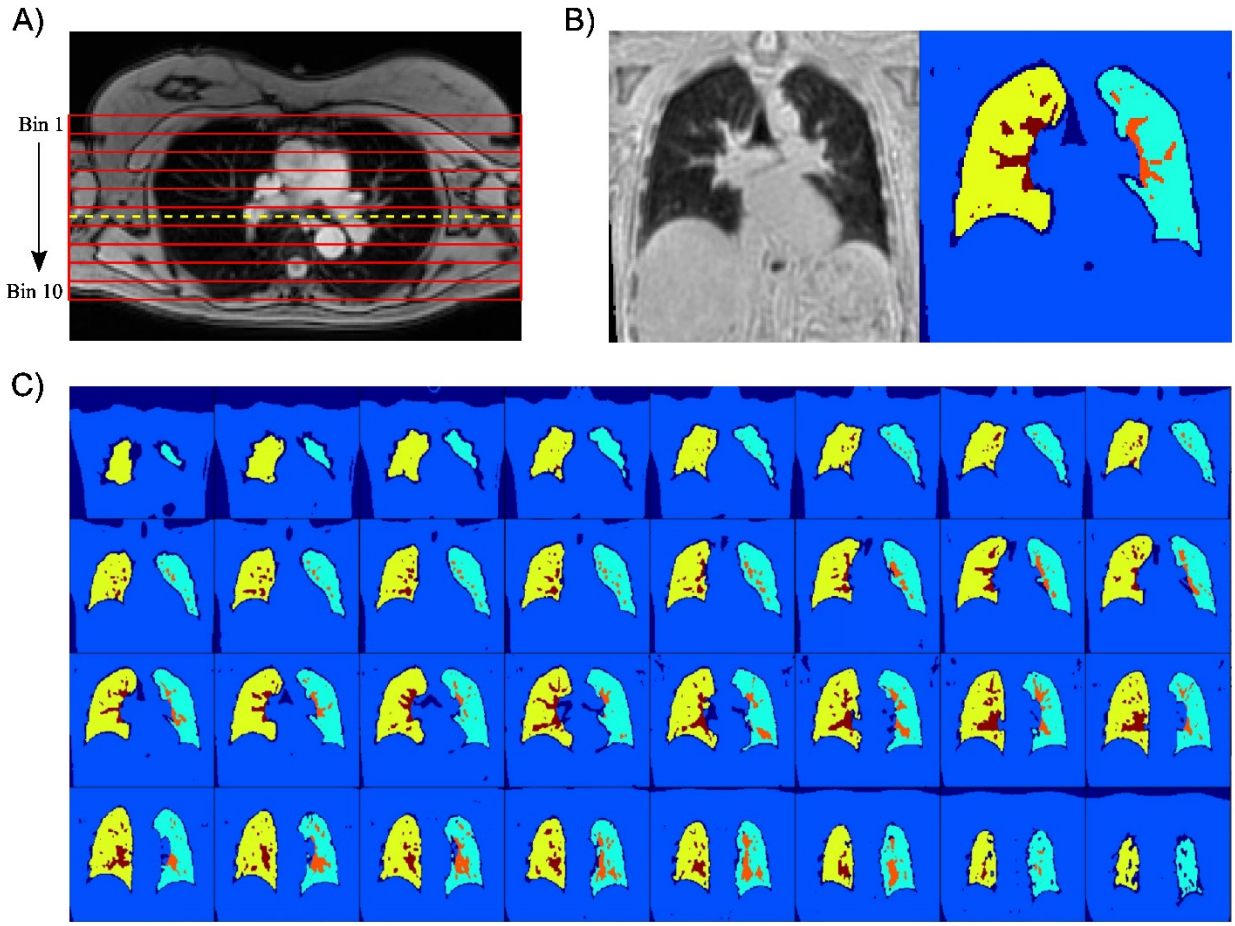

Figure 2.1: ***(A)*** *Location of the 10 binned lung regions containing coronal slices in the chest-to-back direction for regional analysis of the lung parenchyma with an equal number of slices in each bin.* ***(B)*** *One sample coronal slice (position shown as yellow dashed line in (A)) and the corresponding segmentation mask show the five segmented regions including the reference tissue outside of the lungs, parenchyma in the right and left lungs and the vascular pool in the right and left lungs.* ***(C)*** *Coronal slices from chest to back (every second slice) showing the five segmented regions.*

2.2.4: Regional Lung Analysis

The predominant spatial variation in lung water content is in the chest-to-back direction[5,6,96,97] with uniform distributions expected in the head-to-foot and right-to-left directions[5]. In order to calculate chest-to-back gradients and their trends over time, the 3D images were grouped into 10 equally sized bins with coronal slice orientations (Fig. 2.1A). Each bin contained the same number of coronal slices, with bin 1 representing the slices closest to the chest and bin 10 closest to the back. The average rLWD was calculated from all lung pixels (parenchyma plus vascular) within each bin of slices and also for just the parenchyma. The slices within each bin were re-calculated for each time point to account for changes in total lung volume over time.

2.3: Results

The average time from the supine body positioning to the completion of the first imaging time-point was 3:54±0:26 min, with an increment of 1:16 minutes between each subsequent time-point for an average total study time of 25:24±0:25 min. All grouped results are reported using the mean time for the first time point to define a common time-axis for all subjects. Representative images at FRC (minimum lung volume) and FRC+TV (maximum lung volume) show typical normalized images and segmented lung regions (Fig. 2.2). Sample FRC images for all subjects are provided in Fig. 2.13 (end of chapter).

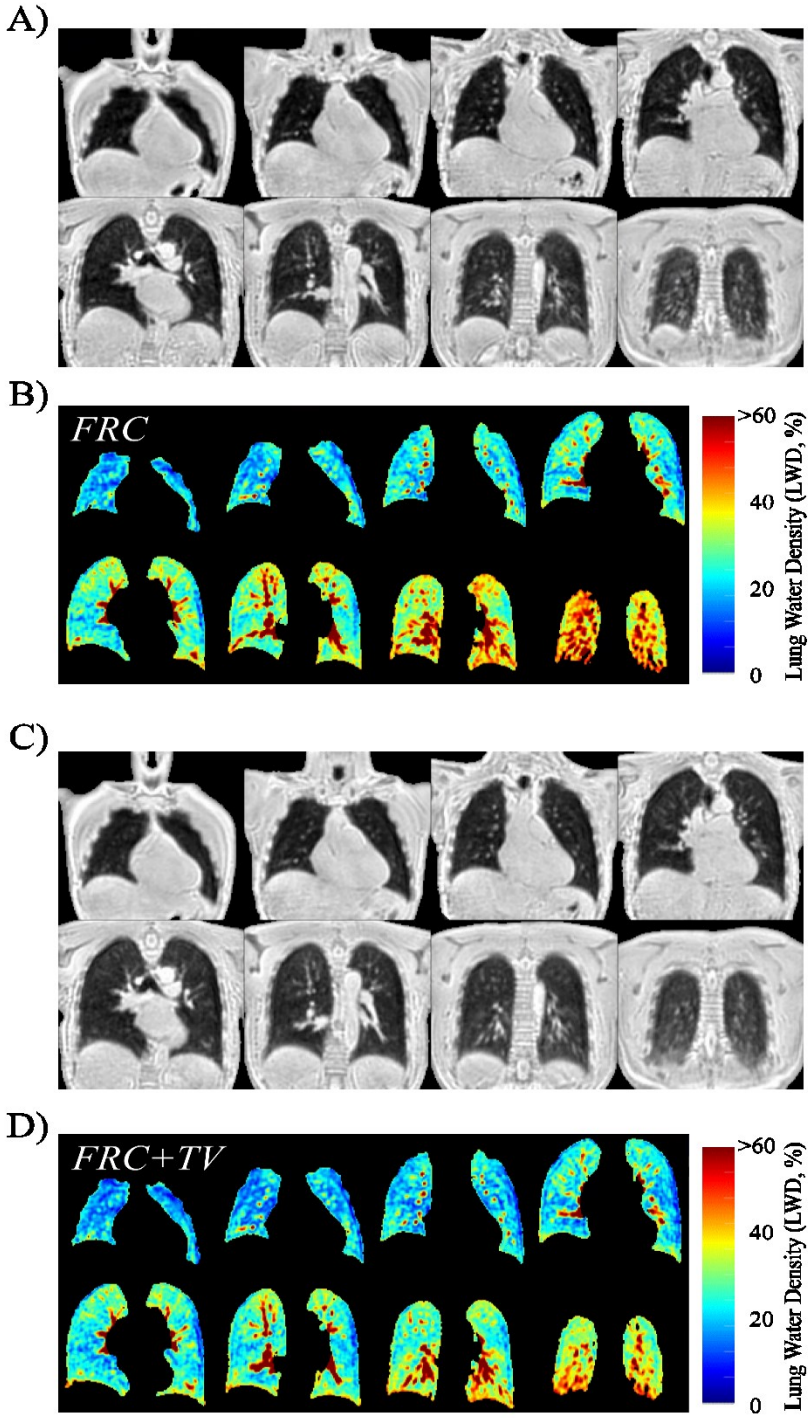

Figure 2.2: *Sample chest-to-back coronal slices from a free-breathing Yarnball acquisition.* ***(A)*** *Normalized images reconstructed at FRC (functional residual capacity, minimum lung volume).* ***(B)*** *Images from (A) including the lung segmentation.* ***(C)*** *Normalized images reconstructed at FRC+TV (maximum lung volume = FRC + tidal volume).* ***(D)*** *Images from (C) including the lung segmentation. 8 of 120 coronal slices are shown.*

2.3.1: Lung Water Density and Volume Changes at FRC

At FRC, there was a statistically significant increase in global rLWD (parenchyma plus vascular) over time (31.8±5.5% at t = 3:54 min vs 34.8±6.8% at t = 25:24 min, p=0.001), with an increase in rLWD for all 9 subjects. There was a statistically significant decrease in total lung volume over time (2.39±0.62 L at t = 3:54 min vs 2.13±0.63 L at t = 25:24 min, p<0.001), with a decrease in volume for all 9 subjects. There was a statistically significant decrease in total lung water volume (730±125 mL at t = 3:54 min vs 706±126 mL at t = 25:24 min, p=0.028), with a decrease in total lung water volume in 6 of the 9 subjects. Vascular water volumes did not change significantly over time (112±28 mL at t = 3:54 min vs 121±27 mL at t = 25:24, p = 0.077). Starting and final values for rLWD, lung volume, lung water volume and vascular water volume at the FRC respiratory phase for all 9 subjects are shown in Table 2.1. rLWD values in the parenchyma region (i.e. excluding the vascular region) are summarized in Table 2.2.

Table 2.1 *Lung Volumes and Water Content at FRC (Functional Residual Capacity)*

	rLWD (%)			***Lung Volume (L)***			***Lung Water Volume (mL)***			***Vascular Water Volume (mL)***		
Subject	***Start***	***End***	***Change***	***Start***	***End***	***Change***	***Start***	***End***	***Change***	***Start***	***End***	***Change***
1	30.3	31.0	0.68	2.63	2.46	-0.17	794	761	-34	142	141	-1
2	27.9	29.7	1.71	3.51	3.31	-0.20	977	977	1	150	160	11
3	35.5	41.0	5.52	1.68	1.38	-0.31	588	554	-35	100	102	2
4	43.5	49.7	6.21	1.71	1.42	-0.29	736	693	-43	87	128	41
5	27.5	30.2	2.75	2.78	2.41	-0.36	759	724	-34	105	114	9
6	26.2	28.6	2.42	2.68	2.50	-0.19	697	709	12	92	98	6
7	35.5	37.1	1.58	1.87	1.65	-0.21	657	605	-52	115	115	1
8	29.7	32.4	2.72	1.90	1.80	-0.10	564	583	19	73	75	2
9	29.6	33.1	3.46	2.72	2.28	-0.44	801	751	-50	145	152	7
Mean	*31.8*	*34.8**	*3.01*	*2.39*	*2.13**	*-0.25*	*730*	*706**	*-24*	*112*	*121*	*9*
STD	*5.5*	*6.8*	*1.82*	*0.62*	*0.63*	*0.11*	*125*	*126*	*27*	*28*	*27*	*13*

rLWD, Lung water density; *values are significantly different from the first time point (Start) to the last time point (End), p<0.05.

Table 2.2 *Lung Volumes and Water Content at FRC (Functional Residual Capacity), Lung Parenchyma Only*

	rLWD (%)			*Lung Volume (L)*			*Lung Water Volume (mL)*		
Subject	***Start***	***End***	***Change***	***Start***	***End***	***Change***	***Start***	***End***	***Change***
1	27.5	28.0	0.50	2.38	2.22	-0.16	652	619	-33
2	25.7	27.2	1.47	3.22	3.01	-0.20	824	815	-9
3	32.4	37.5	5.01	1.51	1.22	-0.29	484	451	-33
4	41.4	46.0	4.6	1.58	1.25	-0.34	649	566	-84
5	25.5	27.8	2.34	2.57	2.21	-0.37	652	610	-41
6	24.3	26.5	2.25	2.50	2.31	-0.19	605	610	4
7	32.5	33.7	1.22	1.68	1.47	-0.21	541	490	-51
8	27.8	30.4	2.65	1.77	1.67	-0.10	490	506	16
9	26.8	29.6	2.80	2.46	2.03	-0.43	659	599	-60
Mean	*29.3*	*31.9**	*2.54*	*2.19*	*1.93**	*-0.25*	*617*	*585**	*-32*
STD	*5.4*	*6.4*	*1.50*	*0.58*	*0.59*	*0.11*	*105*	*106*	*32*

rLWD, Lung water density; *values are significantly different from the first time point (Start) to the last time point (End), $p<0.05$.

Relative changes in average rLWD, lung volume and whole lung water volume for all time points, relative to the first time point, show the time-course up to the 25-minute time point (Fig. 2.3, FRC respiratory phase). The average rLWD, relative to first time point, had a logarithmic growth pattern with a total increase of ~9% while total lung volume decreased by ~11% with a similar pattern over time (Figs. 2.3A and B). Total water volume decreased by ~3% over the 25-minute interval (Fig. 2.3C). rLWD and lung volumes did not achieve steady-state values by the 25-minute time point. All time-course data shows the average values for all participants with error bars for the standard deviation of the mean of each subject.

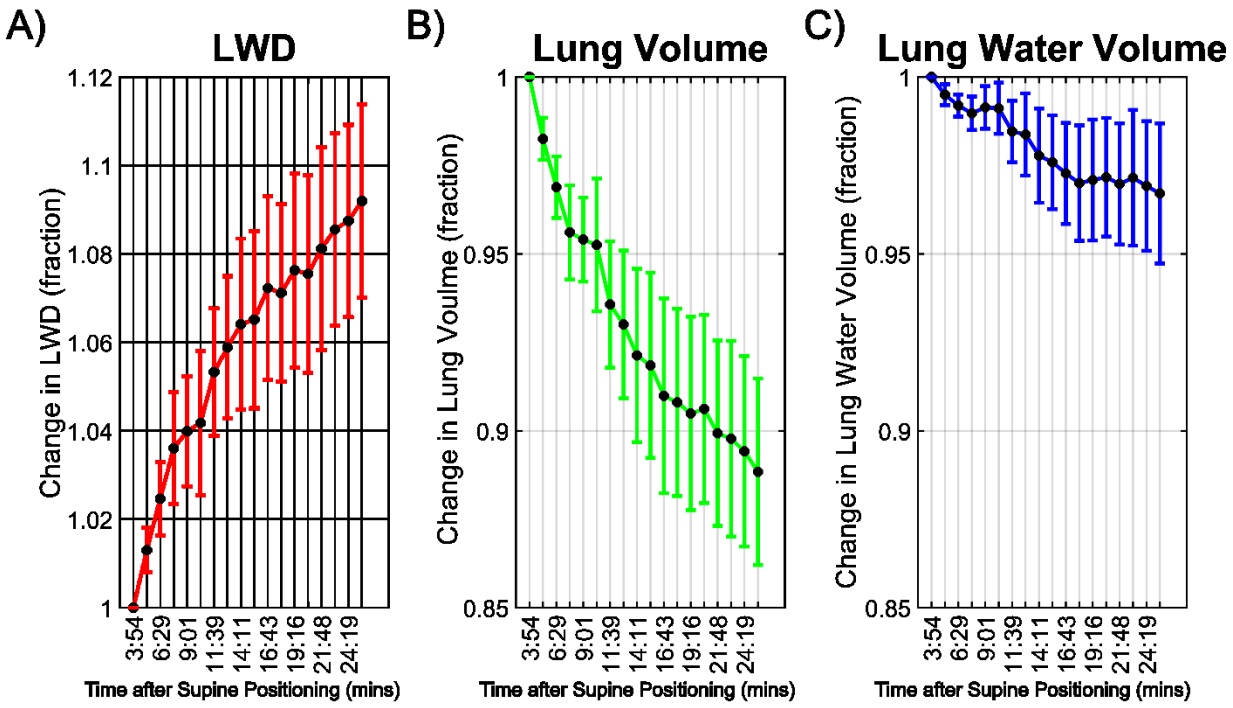

Figure 2.3: *Fractional change over time for **(A)** whole lung average rLWD **(B)** total lung volume and **(C)** total lung water volume at FRC (functional residual capacity, minimum lung volume), following supine body positioning. All values are normalized to the first time point. Plots begin at time = 3:54 minutes to account for subject set-up time and time to complete first scan. Average values for all participants are shown with error bars for standard deviation of the mean.*

The average regional rLWD in all 10 chest-to-back bins show an increase in lung water density over time with an expected chest-to-back gradient at the first time point 9baseline), with ~20% rLWD for the chest and ~40% rLWD at the back (Fig. 2.4A). Sample axial images are seen in Fig. 2.5, giving a visual depiction of the characteristic chest-to-back gradient. The absolute increase in rLWD over time was uniform from chest to mid-lung (bins 1 to 6), all with an increase of ~1.5%, with larger absolute increases of ~5% towards the back, increasing from 40% to 45% by 25 minutes after supine positioning (Fig. 2.4B). Volume changes in the 10 chest-to-back bins showed a similar pattern as rLWD, with larger changes towards the back (Fig. 2.6). Similar results were found at the FRC+TV respiratory phase (not shown).

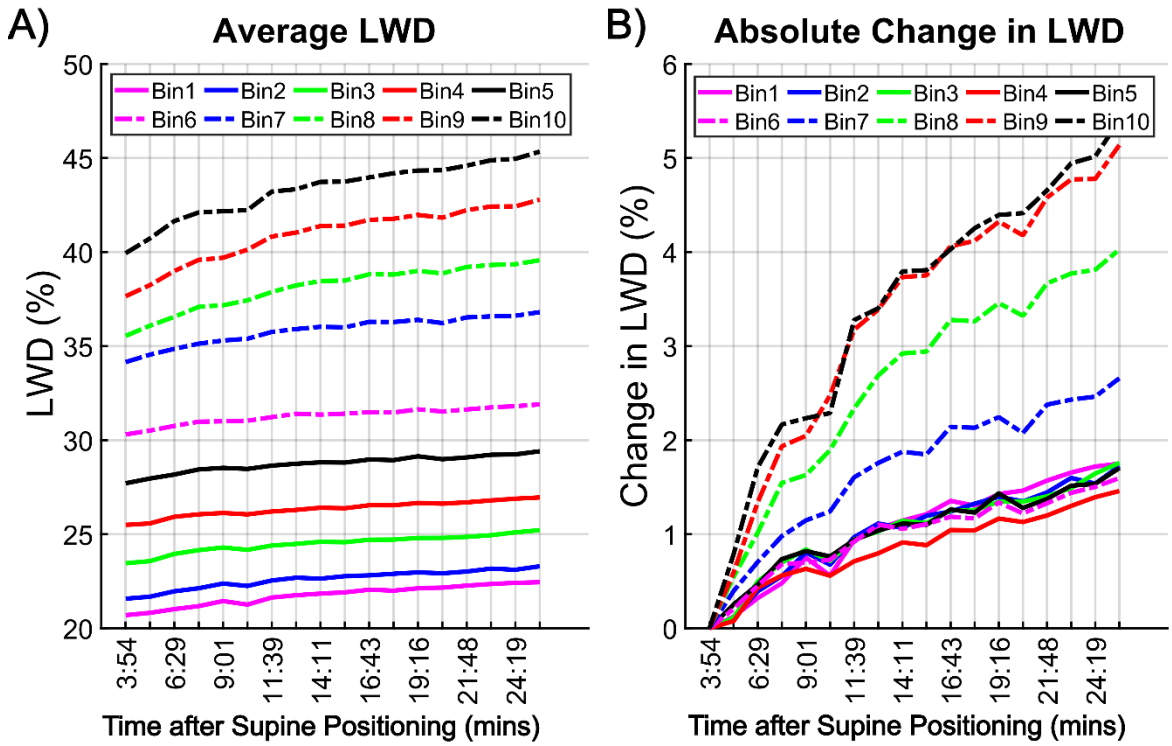

Figure 2.4: ***(A)*** *Absolute rLWD (average of all nine subjects) after supine body positioning in the 10 binned regions from chest (bin 1) to back (bin 10), as shown in Fig 2.1.* ***(B)*** *The change in absolute rLWD from the first time point in the 10 binned regions. All results are for images reconstructed at functional residual capacity.*

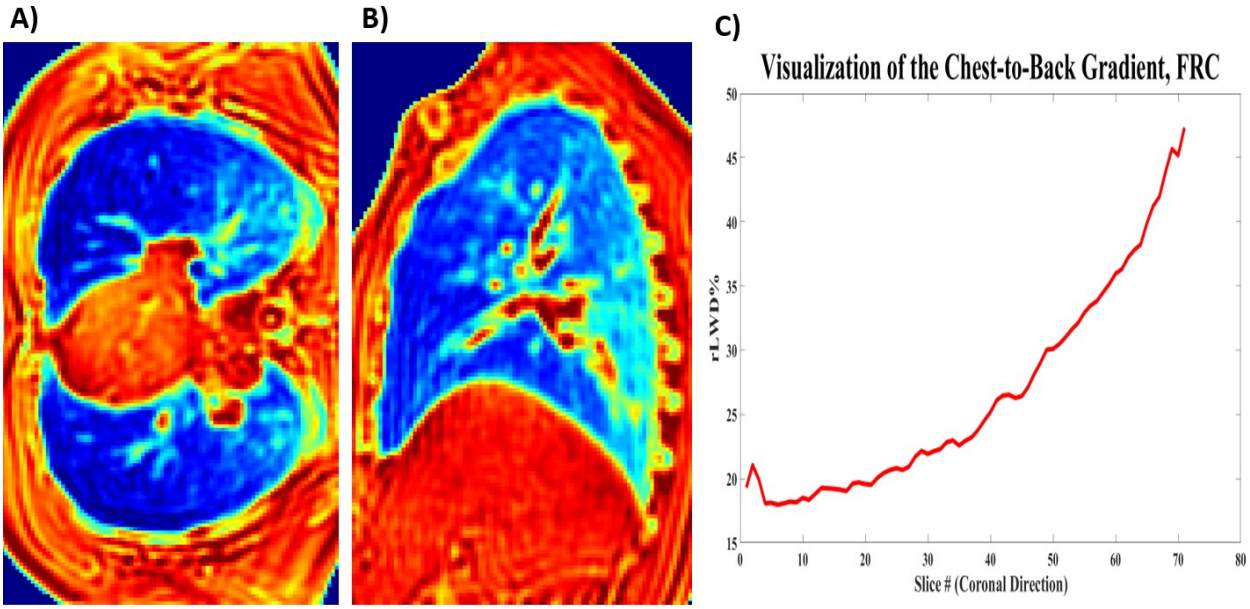

Figure 2.5: (A) *Sample normalized image with axial view (axial slice 65 of 143, taken at FRC).* **(B)** *Same subject, same time point, sagittal view (sagittal slice 55 of 159, taken at FRC).* **(C)** *Calculated rLWD% of subject in* **(A) and (B)** *in each coronal slice (71 slices within the lung parenchyma mask).*

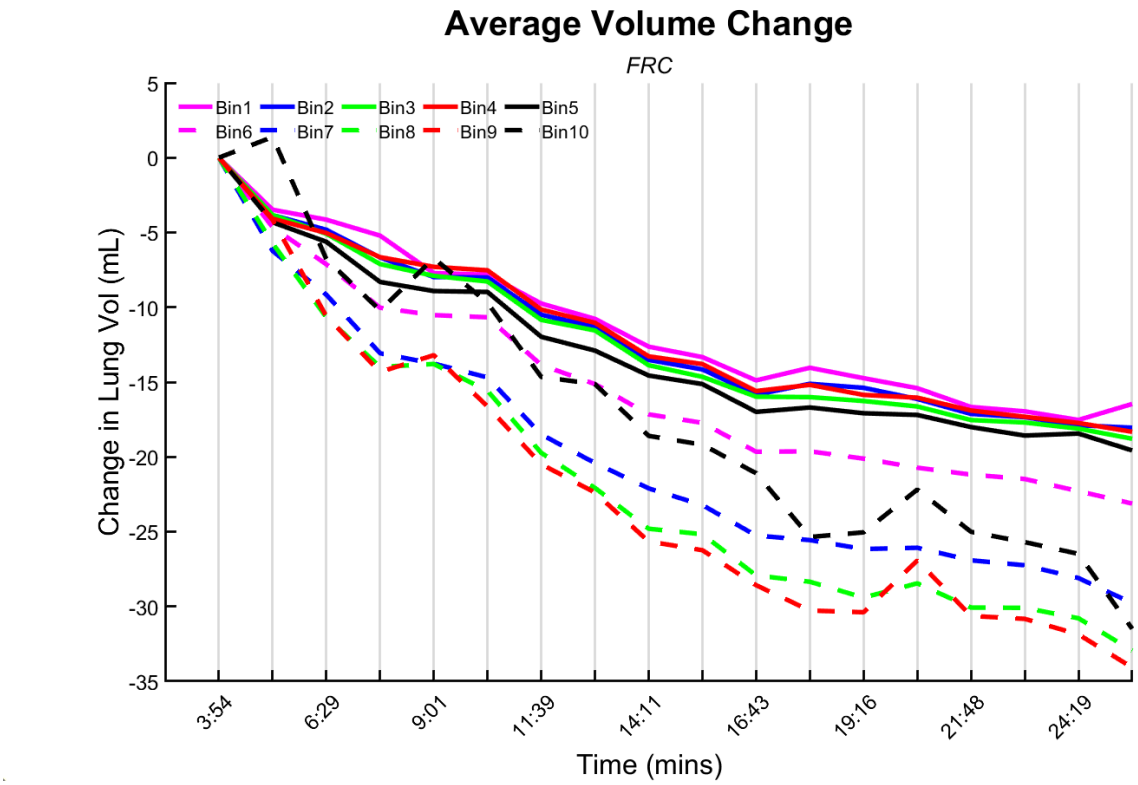

Figure 2.6: *The change in absolute lung volume from the first time point in the 10 binned regions. All results are for images reconstructed at functional residual capacity.*

The reduction in lung volumes over time following supine body positioning was confirmed using the real-time gradient-echo images. Representative images early (1 minute) and late post-positioning (20 minutes) illustrate the reduction in lung volume (Fig. 2.7A). The relative change in lung area over the 24 minutes following supine positioning show an average volume decrease of ~10% across the three subjects with similar results for all three slices (Fig. 2.7B).

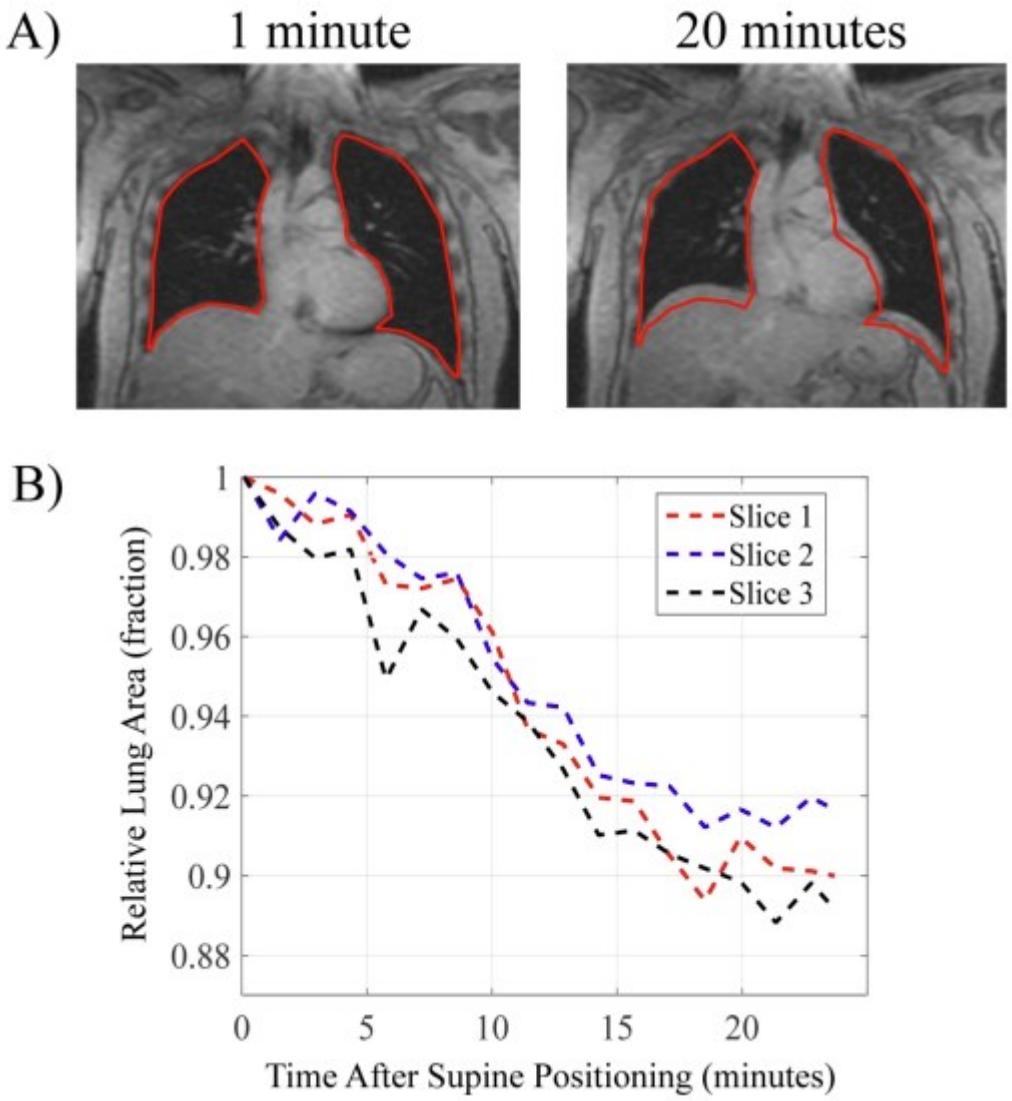

Figure 2.7*:**(A)** Sample real-time gradient echo images at FRC at 1 minute and 20 minutes following supine body positioning illustrate the reduction in lung area over time. The same red outline of the lungs is shown at both time points.* ***(B)*** *The average relative lung areas from the three subjects are shown as a function of time after supine body positioning for three coronal slices. The average of the FRC areas over a 55 second interval are used to represent FRC at each time point.*

2.3.2: Lung Water Density and Volume Changes at FRC + TV

At FRC+TV, there was a statistically significant increase in average rLWD over time (26.6±3.2% at t = 3:54 min vs 28.9±2.8% at t = 25:24 min, p = 0.005), with an increase in average rLWD over time in 7 of 8 subjects (one of the 9 subjects had image artifacts at the FRC+TV respiratory phase, and thus was excluded from FRC+TV calculations). There was a statistically

significant decrease in total lung volume over time (2.94±0.63 L at t = 3:54 min vs 2.61 ±0.64 L at t = 25:24 min, p<0.001), with a decrease for all subjects. Total lung water volume did not change significantly over time (767±122 mL at t = 3:54 min vs 736±137 mL at t = 25:24, p = 0.088). Vascular water volumes did not change significantly over time (107±30 mL at t = 3:54 vs 113±29 mL at t = 25:24 min, p = 0.216). Starting and final values for rLWD, lung volume, lung water volume and vascular water volume at the FRC+TV respiratory phase are shown in Table 2.3. rLWD values in the parenchyma region are summarized in Table 2.4.

Table 2.3 *Lung Volumes and Water Content at FRC+TV (Functional Residual Capacity + Tidal Volume)*

	rLWD (%)			***Lung Volume (L)***			***Lung Water Volume (mL)***			***Vascular Water Volume (mL)***		
Subject	***Start***	***End***	***Change***	***Start***	***End***	***Change***	***Start***	***End***	***Change***	***Start***	***End***	***Change***
1	25.8	27.7	1.86	3.22	2.87	-0.34	828	793	-35	137	131	-6
2	25.3	27.0	1.68	3.95	3.74	-0.21	996	1006	10	135	147	11
3	32.3	34.9	2.60	2.06	1.63	-0.43	659	564	-94	79	98	19
5	23.8	28.3	4.44	3.30	2.76	-0.54	782	775	-7	105	91	-14
6	24.4	25.6	1.26	3.02	2.87	-0.15	730	730	0	88	100	12
7	31.2	30.6	-0.55	2.40	2.15	-0.24	741	653	-88	84	113	29
8	25.2	29.4	4.19	2.34	2.07	-0.28	588	605	17	74	72	-3
9	24.9	27.8	2.93	3.27	2.76	-0.51	811	765	-46	151	155	4
Mean	*26.6*	*28.9**	*2.30*	*2.94*	*2.61**	*-0.34*	*767*	*736*	*-30*	*107*	*113*	*7*
STD	*3.2*	*2.8*	*1.62*	*0.63*	*0.64*	*0.14*	*122*	*137*	*43*	*30*	*29*	*14*

rLWD, Lung water density; *values are significantly different from the first time point (Start) to the last time point (End), p<0.05.

Table 2.4 *Lung Volumes and Water Content at FRC+TV (Functional Residual Capacity + Tidal Volume), Lung Parenchyma Only*

	rLWD (%)			***Lung Volume (L)***			***Lung Water Volume (mL)***		
Subject	***Start***	***End***	***Change***	***Start***	***End***	***Change***	***Start***	***End***	***Change***
1	23.5	25.2	1.75	2.95	2.63	-0.32	689	660	-28
2	23.5	25.0	1.46	3.67	3.45	-0.22	858	859	1
3	30.3	31.9	1.57	1.92	1.47	-0.45	577	465	-112
5	22.0	26.5	4.48	3.08	2.59	-0.50	675	683	8
6	22.7	23.7	1.01	2.84	2.66	-0.17	641	628	-12
7	29.3	27.8	-1.49	2.25	1.95	-0.30	655	538	-117
8	23.4	27.6	4.19	2.20	1.93	-0.26	513	532	19
9	22.3	24.7	2.41	2.97	2.48	-0.50	660	609	-52
Mean	*24.6*	*26.6**	*1.90*	*2.73*	*2.4**	*-0.34*	*658*	*622*	*-37*
STD	*3.3*	*2.6*	*1.90*	*0.57*	*0.60*	*0.13*	*99*	*120*	*53*

rLWD, Lung water density; *values are significantly different from the first time point (Start) to the last time point (End), $p<0.05$.

Changes in average rLWD, lung volume and whole lung water volume for all time points, relative to the first time point, show the time-course up to the 25-minute time point for the FRC+TV respiratory phase (Fig. 2.8). The normalized average rLWD had a logarithmic growth pattern with a total increase of ~10% while total lung volume decreased by ~12% with a similar pattern over time (Figs. 2.8A and B). Total water volume decreased by ~3% over the 25-minute interval (Fig. 2.8C). Over 95% of the change in rLWD and lung volumes was completed by 18 of the 25-minute time course.

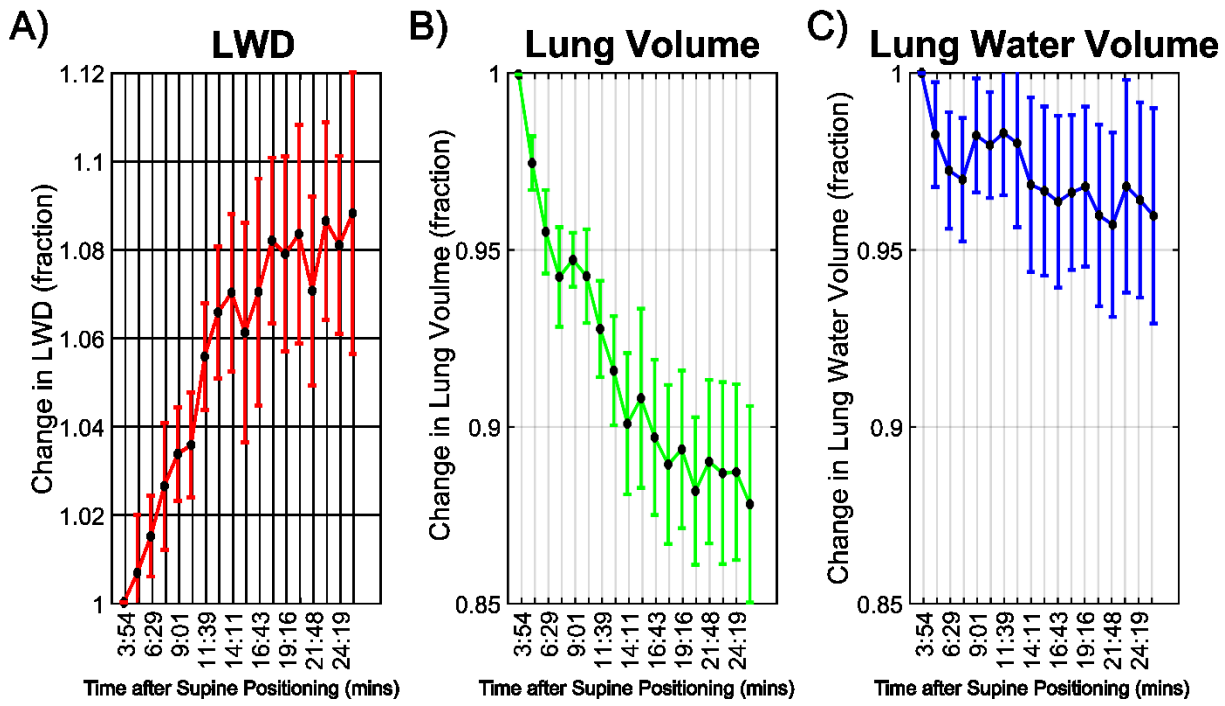

Figure 2.8: *Fractional change over time for **(A)** whole lung average rLWD **(B)** total lung volume and **(C)** total lung water volume at FRC+TV (maximum lung volume = FRC + tidal volume). All values are normalized to the first time point. Plots begin at time = 3:54 minutes to account for subject set-up time and time to complete first scan. Average values for all participants are shown with error bars for standard deviation of the mean.*

Lung volumes were significantly larger, and rLWD density values were significantly lower at FRC+TV as compared to FRC for all time points following supine positioning ($p<0.001$ for all). The lung water volume was significantly higher at the FRC+TV respiratory phase ($p<0.01$), by ~4%, at all time-points following supine positioning (Table 1 and 2).

Tidal volume, or the change in lung volume over a respiratory cycle, decreased significantly over time after supine positioning (474±89 mL at t = 3:54 vs 382±91 mL at t = 25:24, p = 0.018) as shown in Fig. 2.9. There were no significant changes in breathing rate over time, with average values of 13.3 ± 3.3 breaths per minute over the full study duration and less than 1 breath per minute change over time.

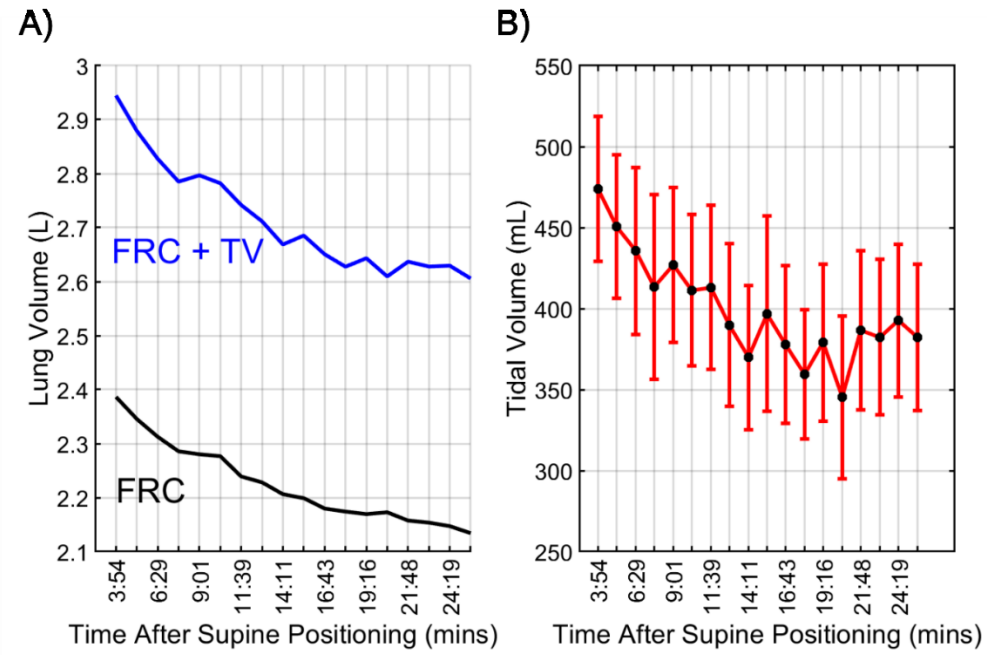

Figure 2.9: ***(A)*** *Lung volumes at FRC (functional residual capacity, minimum volume over the respiratory cycle) and FRC+TV (functional residual capacity plus tidal volume, maximum volume over the respiratory cycle) for the 25 minutes following supine body positioning. Average values from all subjects are shown.* ***(B)*** *Tidal volumes (mean ± standard deviation) for the 25 minutes following supine body positioning. Average values for all participants are shown with error bars for standard deviation of the mean.*

Bland and Altman plots display the percentage difference in rLWD, lung volume and lung water volumes between time-steps 17 and 18 for all subjects, and FRC and FRC+TV respiratory phases (Fig. 2.10). ICC>0.99 for comparisons.

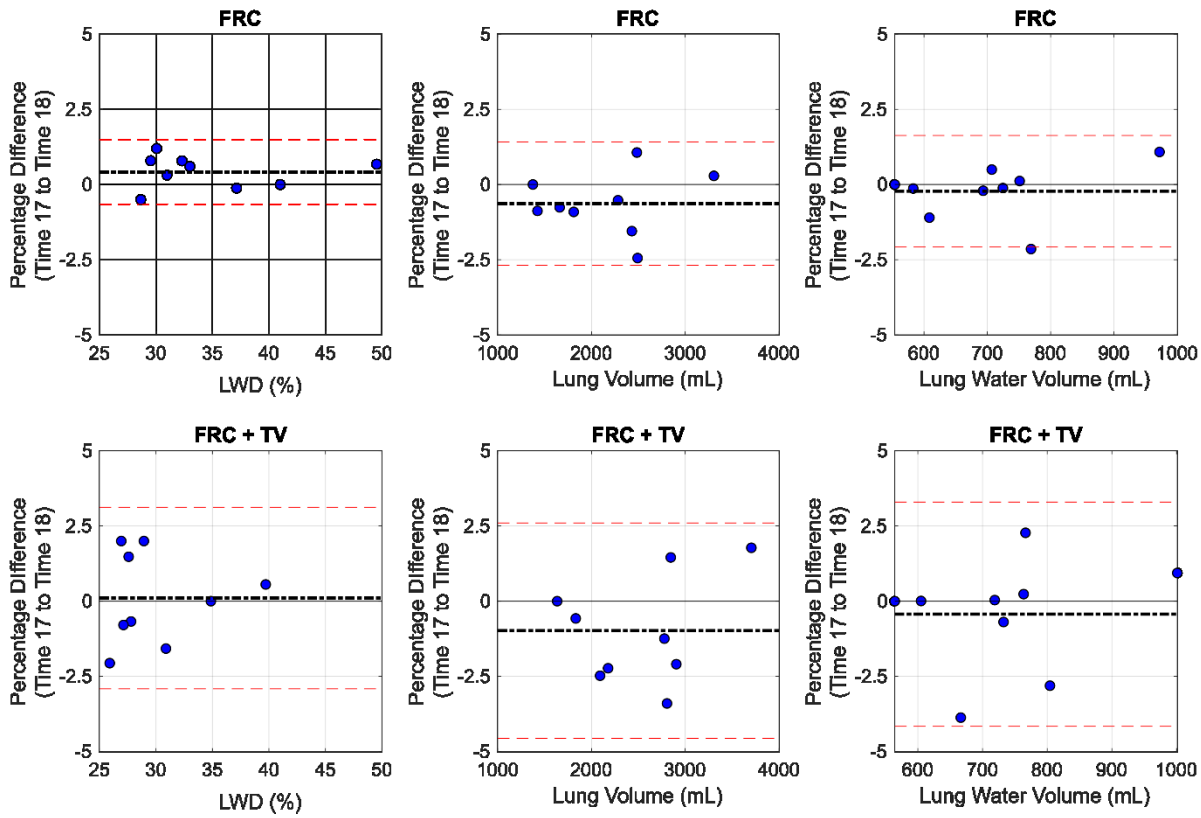

Figure 2.10: *Bland and Altman plots show the percentage difference in rLWD, lung volume and lung water volumes between the repeated scans at time-point 17 and time-point 18 at FRC (functional residual capacity) and FRC+TV (FRC + tidal volume) respiratory phases. ICC>0.99 for all cases.*

In additional studies, changes in rLWD, lung volume and total water volume following a total lung capacity inspiration breath-hold followed the same pattern as was observed following supine body positioning (Fig. 2.11). In particular, ~10% increase in rLWD was observed over 15 minutes after the breath-hold with a corresponding decrease in lung volume over the same interval.

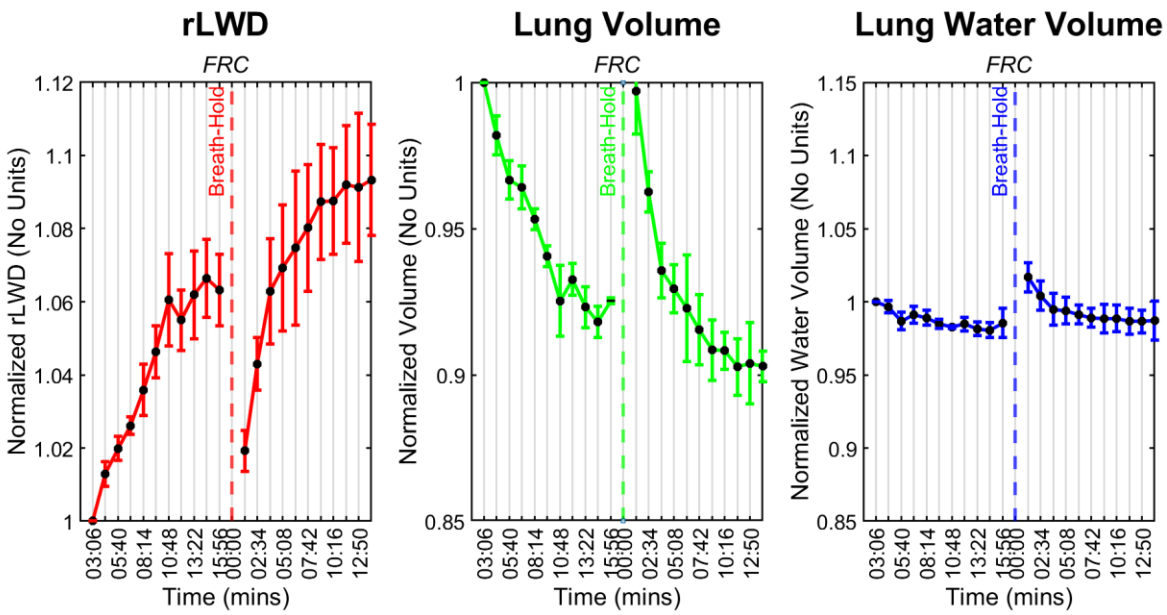

Figure 2.11: *Fractional change over time for* **A)** *whole lung average rLWD* **B)** *total lung volume and* **C)** *total lung water volume at FRC, following supine body positioning and sub-sequentially following a total lung capacity (end-inspiration) breath-hold (sub-group of 3 participants). All values are normalized to the first time point with a total of 11 time-points over 15 minutes after supine positioning and after the breath-hold maneuver. Average values for all participants are shown with error bars for standard deviation of the mean.*

Nitrogen washout studies further confirmed the MRI-derived changes in lung volume following supine body position with similar time-course and magnitude of volume changes (Fig. 2.12). Lung volumes decreased 27±6% from upright to the first supine time point (not shown in Fig. 2.12) with an additional ~12% over time from the onset of supine positioning.

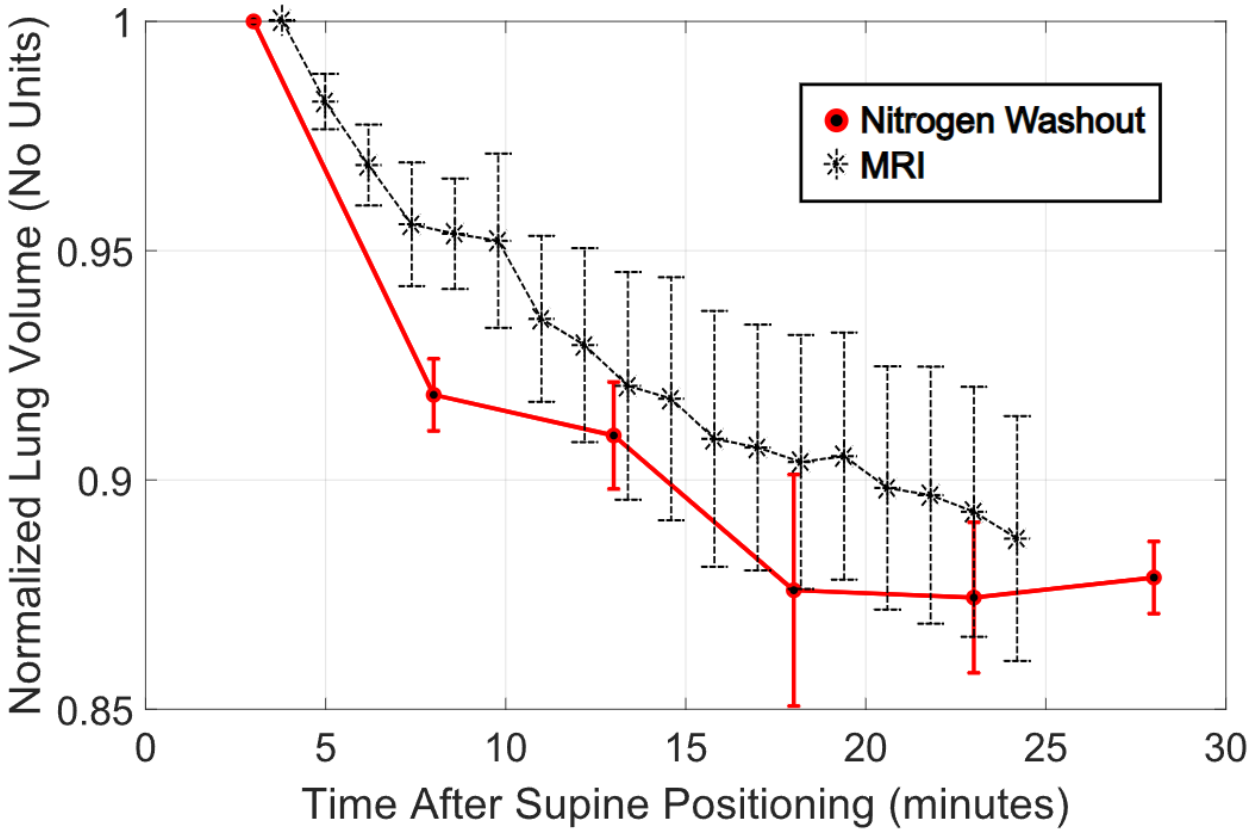

Figure 2.12: *Relative changes in lung volume at FRC measured with the nitrogen washout (red) method in three participants as a function of time following supine body positioning. There was an immediate 27 ± 6% drop in lung volumes from upright to supine positioning (not shown). The nitrogen washout method showed good agreement in changes in lung volume over time with the findings of UTE YB.*

2.4: Discussion

An efficient Yarnball k-space trajectory enabled relatively short scan times of 74 seconds per time point, with free-breathing acquisitions and 3D image reconstructions at minimum and maximum lung volumes with tidal breathing. The current study illustrated a dynamic increase in global lung water density (rLWD) following supine body positioning that approached but did not reach steady-state after 25 minutes, with a 9-10% relative increase in water density following a logarithmic pattern over time. The increased water density was primarily the result of an underlying decrease in total lung volume over time, during restful tidal breathing, and thus an increase in parenchyma tissue density but not a net movement of water into the lungs. In particular,

despite the increased rLWD, the global water volume was shown to decrease slightly over the 25-minute window following supine positioning. The expected increase in total thoracic blood volume with supine positioning[10,11,46,47,92] was not observed within the lungs, or may have occurred prior to the first imaging time-point at ~4 minutes after the change in body position. Breathing rates did not vary but tidal volumes dropped significantly over time following supine body positioning. The temporal evolution of each parameter (rLWD, lung volume, lung water volume, vascular water volume) was similar at minimum lung volume (FRC) and maximum lung volume (FRC+TV) with tidal breathing.

The decrease in lung volume following supine body positioning was validated using a nitrogen washout study, confirming the time course and magnitude of the volume changes at FRC (~12% change over 30 minutes). These slow changes followed the large drop in lung volume of ~27% from upright to the first supine data point, which was expected[24,98–100]. The decrease in lung volume following supine body positioning was further validated using a separate real-time imaging approach which illustrated a similar time course and magnitude of changes (10% reduction). Additional serial MRI experiments following a large inspiratory breath-hold at total lung capacity also confirmed the relatively slow dynamic reduction in lung volume and the associate increase in rLWD following large changes in lung volume (in this case, an end-inspiration breath-hold), suggesting relaxation of the respiratory muscles as a potential mechanism.

The reduction in lung volumes and tidal volumes from sitting to supine body position, in steady state conditions, are expected[24,100]. While the majority of lung volume reduction likely takes place immediately when laying down, with the change in body position relative to gravity[98,99], the current study shows that volumes continue to drop for tens of minutes following supine positioning, with direct effects on lung water density. In contrast, the majority of the gravity effects on the chest-to-back water density is completed prior to our earliest time point at ~4 minutes. In particular, all time-points following supine body positioning showed a similar characteristic chest-to-back gradient in water density (Fig. 2.4A), or the so-called slinky effect whereby the dependent lung regions (lowest in relation to gravity) are relatively compressed[7]. Regional analyses showed that the absolute change in rLWD over time was larger at the back as compared to chest and mid-lung positions, which is most likely due to the higher water content at

the back as opposed to a shift of water to the back. Future studies will require higher temporal resolution and earlier starting points following supine positioning to capture the dynamics of the direct effects of gravity on lung water density. A majority of the time required before the first time point was acquired was spent setting the chest coil into place on the subject's chest and properly localizing the scanner so that the whole torso is within the full FOV. Future studies could explore methods to reduce the delay to the initial time point such as acquiring a localization scan on a subject and sequentially removing them from the scanner, returning them to upright steady-state, and having them return to approximately the same location on the scanner bed, thus eliminating the time required to localize the subject.

A recent study of rLWD imaging study at 0.55T showed no significant changes in water density over time with changes between supine and prone body positioning, with 4 image volumes acquired over 10 minutes (2.5 minutes per image set), starting 6 minutes after positioning.[6] However, the timing from the upright to supine positioning was not directly reported and thus the larger volume changes that occur at the earlier time points following this particular positional change may not have been captured.

A small reduction in total lung water volume following supine positioning was measured in the current study but lung volume and inflation were shown to be the predominant physical factors with potential to strongly affect rLWD values following patient positioning. Longer and thus necessarily free-breathing studies, with some form of respiratory navigator, are commonly used for lung imaging in order to achieve the targeted spatial resolutions and sufficient signal to noise ratios, and thus image reconstruction at FRC is routine. The use of free-breathing acquisitions and reconstruction at FRC minimizes the dependence of lung volumes, and thus water density, on patient compliance. However, the observed reduction of FRC by ~10% over 25 minutes, with a corresponding increase in rLWD, indicates that the timing of the lung water density measurements should be considered, ideally with scans taking place later in the MRI exam if possible, or at the same time following positioning on the patient table. An end-inspiration breath-hold was shown to have a similar effect on lung volumes with a relatively long recovery of FRC volumes with tidal breathing following a single breath-hold again highlighting the variability of lung volumes even during resting breathing.

At the final study time-point, the FRC+TV volumes were ~18% larger than FRC (2.61 L versus 2.13 L), with a correspondingly lower rLWD of 28.9% at FRC+TV versus 34.8% at FRC (i.e. a 17% reduction in rLWD). These findings agree with the expected linear relationship between lung volume and water density[101], and highlight the extreme sensitivity of rLWD to the highly variable physiologic parameter of lung inflation. Breath-hold duration measurement of rLWD is also possible[5], but may be prone to larger variations in volume and thus larger variations in rLWD due to the subject-controlled breath-hold positioning and thus lung volume. Image registration has been shown to enable calculation of the Jacobian which can be used to correct the changes in rLWD with changes in lung inflation[6]. This approach has potential to detect changes in rLWD independent of lung inflation in an individual.

Limitations

The current study has several limitations. First, the use of all of the solid tissues surrounding the lungs as a signal reference will be prone to systematic errors, in particular, in cases of fluid accumulation in the reference tissues (e.g. heart failure, kidney failure) or fat accumulation, which would lead to underestimation of rLWD. rLWD and water volumes reported in the current study are calculated relative to the reference tissues (which are themselves 70-80% water content[79–81,102]), so overestimate the true densities and volumes. There are partial volume errors for the lung tissue regions with no discrimination of vascular and extravascular pools with only the largest blood vessels being visible. All measured values within the lungs (rLWD, volumes and water volumes) will depend on the machine learning masks used to identify parenchyma and vascular spaces, and could thus be a source of systematic errors. Corrections for coil shading effects (normalization) have not been validated in the chest to back direction and may be prone systematic errors in calculated of the chest to back rLWD gradient. The maximum lung volume over the respiratory cycle, FRC+TV, was approximated to occur at a respiratory phase of 50% which may underestimate the true maximum value if the peak volumes occur at an earlier or later phase. Finally, the study design included imaging to 25 minutes following supine body positioning which unfortunately was not sufficient to achieve steady state in lung volumes or rLWD.

2.5 Conclusions

Lung water density increases significantly over tens of minutes following supine body positioning (~9% relative increase) as a consequence of corresponding reductions in lung volume. The total volume of lung water is slightly reduced (~3% change). A rLWD% chest-to-back gradient was established before the first time point (<4 minutes), and became more pronounced over time after assuming supine positioning. Valuation of global and regional rLWD should take lung volumes and time after supine positioning into consideration in order to avoid significant bias of water density.

Acknowledgements

We are grateful for the help provided by Andrew Brotto and Dr. Michael Stickland for the determination of lung volumes with nitrogen washout studies.

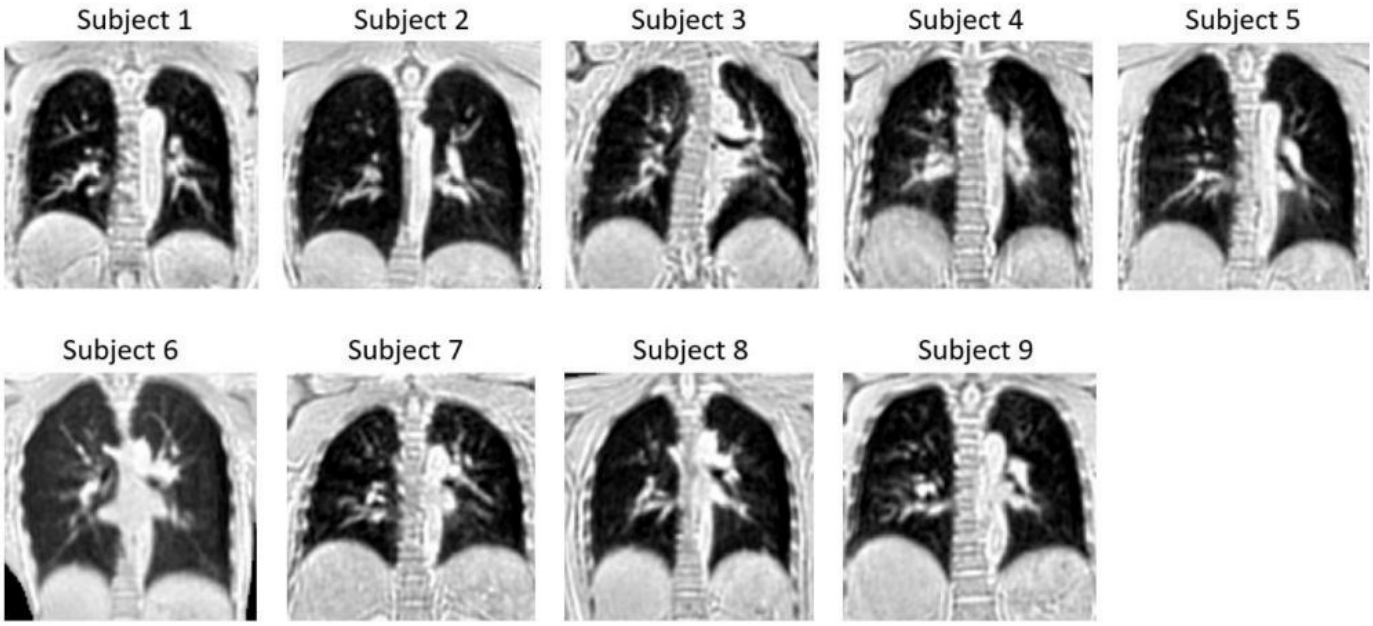

Figure 2.13: *Sample coronal images from the 3D Yarnball acquisitions from each study participant at FRC*

Chapter 3: Discussion

3.1: Future Direction of Dynamic Lung Water Density

With new MRI ideas and technologies giving rise to high-quality and quantifiable lung images, the ability to delve into the specific relationships and dynamics between LWD and known health metrics grows. As discussed in the introduction, elevated levels of LWD is closely related to pulmonary edema and poor health outcomes in heart failure patients[2–4]. These previously observed relationships, however, did not take into consideration any time-course changes in global or regional LWD after supine positioning, and the correlations are largely measured in end-expiration (breath-hold) procedures. It is currently unknown if there is a relationship between health outcomes and irregular patterns in the dynamic changes in LWD during free-breathing experiments. For instance: Could delayed or eliminated formation of the characteristic chest-to-back LWD gradient be indicative of cardiogenic PE vs. non-cardiogenic PE? If instead a significant reduction in global LWD was seen in a patient, could there a be a correlation to a clinical significant diagnosis (e.g. Pneumothorax[103]). Is there a ceiling to the expected increase in LWD over time before a clinically significant correlation can be made (e.g. Pneumonia[104] or Asthma[105])? Do patients suffering from long term respiratory problems such as ARDS have different patterns in dynamic changes in LWD and lung volumes? All of the above questions remain unstudied to date, but can be addressed knowing the expected dynamic patterns for a healthy person that are outlined in this study.

A major indicator of heart failure is a reduced exercise tolerance, and has been associated with increased LWD at rest[1]. A recent study performed by Seeman et al. (2023)[106] is the first lung MRI study to bring light to potential differences in dynamic responses of LWD over time during and after vigorous exercise between healthy subjects and heart failure patients. It was shown that heart failure patients have a slower than expected lung water accumulation rate during exercise, and a slower lung water clearance rate post-exercise during rest, suggesting that

monitoring time-course changes of lung water accumulation/clearance (and the subsequent changes in LWD that this would bring) during quantifiable lung MRI could be useful as a clinical parameter in characterization of potential heart failure patients. This study notes that the potential clinical findings serve only as a proof-of-concept due to low sample size of heart failure patients (n=2) and issues regarding image blurring and artifact-heavy ECG signals caused by excessive motion during exercise[106]. Further exploration into this topic as a clinical tool is clearly warranted, with a potential for the naturally occurring rise in LWD over time at rest noted in this study being referenced when examining the degree to which LWD accumulates over time during exercise.

3.2: Limitations

The major limitation within this study is the dependence upon the assumption that the reference tissue (skeletal muscle, liver, blood, myocardium) will always maintain at 70-80% lung water density. Thus our reported relative lung water density values (rLWD) are not absolute and the true water density is unknown. These evaluations of reference tissue density often do not delve into potential differences in density when disease such as pulmonary edema or heart failure is present. It is possible that in the presence of these diseases, an increase in water density in the reference tissues might be seen, causing systemic errors in the calculation of LWD. It is also noted here that the normalization process used does not directly measure B1 transmit/sensitivity field inhomogeneity, but rather estimates a minimum error normalization map that serves as an approximation for this field inhomogeneity. Though it would add time to complete each complete scan, future studies could prove more accurate results should they employ methods that could potentially provide a more accurate representation of "true" water density (such as performing fat imaging to generate a water density reference map) or B1 field mapping (such as double angle HASTE imaging, as is used in quantitative cardiovascular MRI).

As previously mentioned, SNR is not directly measured in this study, but acquired images are assumed as good SNR (≥ 10) due to the similarity in imaging procedure and resulting rLWD% calculations as Meadus et al (2021)[5]. Theoretically, the optimization process should have resulted in an increase in SNR when compared to the sequence used by Meadus et al, however, this cannot be stated with full certainty. Further attempts to optimize a YB sequence for lung MRI should consider adding a pre-scan image for the purposes of measuring noise and SNR.

The characteristic chest-to-back gradient was already established by the time the first YB scan was completed (~4 minutes). It cannot be stated for certainty then how long it takes for the gradient to appear. The subsequent validation GRE test would likely would have been fast enough to capture the formation of the gradient at 300 ms/image, however, the image quality and 2D nature of the images does not allow for regional rLWD% calculations to be done with any level of accuracy. The dramatic decrease in initial volumes immediately seen in the GRE testing would suggest that the formation of the gradient also occurs quite rapidly, likely in the range of a few seconds after supine positioning is assumed, however, this cannot be confirmed at this time.

The steady-state evolution of LWD and lung volume after supine positioning was not reached in this study. The increase in LWD and the decrease in lung volumes both appeared to be slowing greatly; time step 17-18 showed significantly smaller changes than time step 1-2 in both parameters, suggesting that by 25 minutes the lungs were approaching steady-state. Further studies that measure LWD and lung volumes for longer periods of time (likely 45 minutes – 1 hour) would be required to definitively say how long it typically takes a healthy individual to reach steady state after supine positioning is assumed.

3.3: Conclusions

An optimized version of a UTE YB MRI with machine learning lung segmentation showed excellent ability to provide 3D isotropic, respiratory resolved images in a free-breathing environment with accurate evaluation of lung volumes, lung water content and rLWD% both

globally and regionally. It was found that after supine positioning has occurred, global lung water volume and tidal volume decreased significantly, global lung water content remains constant, and rLWD% increases significantly over time. Larger decreases in lung volume and increases in rLWD% occur towards the back of the lungs than towards the chest. There is not an overall influx of water content into the lungs over time, and vascular blood volume remains relatively constant. The formation of the chest to back gradient in water density happen soon after supine positioning occurs (seconds), with additional global and regional changes evolving over tens of minutes, making the water density in the lungs a dynamic and complex feature.

As LWD becomes studied more closely as a clinical tool, important consideration needs to be placed into the timing of acquired images. Attempting to compare lung images acquired immediately after supine positioning vs. images acquired tens of minutes after supine positioning will introduce significant error into the results.

Bibliography

1. Thompson RB, Pagano JJ, Chow K, et al. Subclinical Pulmonary Edema Is Associated With Reduced Exercise Capacity in HFpEF and HFrEF. *J Am Coll Cardiol*. 2017;70(14):1827-1828. doi:10.1016/j.jacc.2017.07.787

2. Murray JF. Pulmonary edema: pathophysiology and diagnosis. *Int J Tuberc Lung Dis*. 2011;15(2):155-160, i.

3. Platz E, Jhund PS, Campbell RT, McMurray JJ. Assessment and prevalence of pulmonary oedema in contemporary acute heart failure trials: a systematic review. *Eur J Heart Fail*. 2015;17(9):906-916. doi:10.1002/ejhf.321

4. Thompson RB, Chow K, Pagano JJ, et al. Quantification of lung water in heart failure using cardiovascular magnetic resonance imaging. *J Cardiovasc Magn Reson*. 2019;21(1):58. doi:10.1186/s12968-019-0567-y

5. Meadus WQ, Stobbe RW, Grenier JG, Beaulieu C, Thompson RB. Quantification of lung water density with UTE Yarnball MRI. *Magnetic Resonance in Medicine*. 2021;86(3):1330-1344. doi:10.1002/mrm.28800

6. Seemann F, Javed A, Chae R, et al. Imaging gravity-induced lung water redistribution with automated inline processing at 0.55 T cardiovascular magnetic resonance. *J Cardiovasc Magn Reson*. 2022;24:35. doi:10.1186/s12968-022-00862-4

7. Hopkins SR, Henderson AC, Levin DL, et al. Vertical gradients in regional lung density and perfusion in the supine human lung: the Slinky effect. *J Appl Physiol (1985)*. 2007;103(1):240-248. doi:10.1152/japplphysiol.01289.2006

8. Nagaya N, Shimizu F, Kanayama M, et al. Movement of target organs and anatomical landmarks caused by body position change during urological laparoscopic surgery. *Asian Journal of Endoscopic Surgery*. 2020;13(1):65-70. doi:10.1111/ases.12699

9. Howes MK, Hardy WN, Beillas P. The Effects of Cadaver Orientation on the Relative Position of the Abdominal Organs. *Ann Adv Automot Med*. 2013;57:209-224.

10. Wieslander B, Ramos JG, Ax M, Petersson J, Ugander M. Supine, prone, right and left gravitational effects on human pulmonary circulation. *J Cardiovasc Magn Reson*. 2019;21:69. doi:10.1186/s12968-019-0577-9

11. Hagan RD, Diaz FJ, Horvath SM. Plasma volume changes with movement to supine and standing positions. *J Appl Physiol Respir Environ Exerc Physiol*. 1978;45(3):414-417. doi:10.1152/jappl.1978.45.3.414

12. Stobbe RW, Beaulieu C. Three-dimensional Yarnball k-space acquisition for accelerated MRI. *Magnetic Resonance in Medicine*. 2021;85(4):1840-1854. doi:10.1002/mrm.28536

13. Elster AD. Gradient-echo MR imaging: techniques and acronyms. *Radiology*. 1993;186(1):1-8. doi:10.1148/radiology.186.1.8416546

14. Wanger J, Clausen JL, Coates A, et al. Standardisation of the measurement of lung volumes. *European Respiratory Journal*. 2005;26(3):511-522. doi:10.1183/09031936.05.00035005

15. Chaudhry R, Bordoni B. Anatomy, Thorax, Lungs. In: *StatPearls*. StatPearls Publishing; 2023. Accessed May 22, 2023. http://www.ncbi.nlm.nih.gov/books/NBK470197/

16. Biga LM, Bronson S, Dawson S, et al. 22.4 Gas Exchange. Published online September 26, 2019. Accessed May 24, 2023. https://open.oregonstate.education/aandp/chapter/22-4-gas-exchange/

17. Beretta E, Romanò F, Sancini G, Grotberg JB, Nieman GF, Miserocchi G. Pulmonary Interstitial Matrix and Lung Fluid Balance From Normal to the Acutely Injured Lung. *Front Physiol*. 2021;12:781874. doi:10.3389/fphys.2021.781874

18. Hopkins E, Sharma S. Physiology, Functional Residual Capacity. In: *StatPearls*. StatPearls Publishing; 2023. Accessed May 22, 2023. http://www.ncbi.nlm.nih.gov/books/NBK500007/

19. Hallett S, Toro F, Ashurst JV. Physiology, Tidal Volume. In: *StatPearls*. StatPearls Publishing; 2023. Accessed May 22, 2023. http://www.ncbi.nlm.nih.gov/books/NBK482502/

20. Sharratt MT, Henke KG, Aaron EA, Pegelow DF, Dempsey JA. Exercise-induced changes in functional residual capacity. *Respir Physiol*. 1987;70(3):313-326. doi:10.1016/0034-5687(87)90013-2

21. Lum S, Stocks J, Stanojevic S, et al. Age and height dependence of lung clearance index and functional residual capacity. *Eur Respir J*. 2013;41(6):1371-1377. doi:10.1183/09031936.00005512

22. Littleton SW, Tulaimat A. The effects of obesity on lung volumes and oxygenation. *Respir Med*. 2017;124:15-20. doi:10.1016/j.rmed.2017.01.004

23. Morris MJ, Madgwick RG, Lane DJ. Difference between functional residual capacity and elastic equilibrium volume in patients with chronic obstructive pulmonary disease. *Thorax*. 1996;51(4):415-419. doi:10.1136/thx.51.4.415

24. Moreno F, Lyons HA. Effect of body posture on lung volumes. *J Appl Physiol*. 1961;16:27-29. doi:10.1152/jappl.1961.16.1.27

25. Effect of body posture on lung volumes. doi:10.1152/jappl.1961.16.1.27

26. Ventilation-perfusion matching and mismatching | Deranged Physiology. Accessed July 26, 2023. https://derangedphysiology.com/main/cicm-primary-exam/required-reading/respiratory-system/Chapter 073/ventilation-perfusion-matching-and-mismatching

27. Schraufnagel DE. Lung lymphatic anatomy and correlates. *Pathophysiology*. 2010;17(4):337-343. doi:10.1016/j.pathophys.2009.10.008

28. Zavorsky GS, Milne ENC, Lavorini F, et al. Interstitial lung edema triggered by marathon running. *Respiratory Physiology & Neurobiology*. 2014;190:137-141. doi:10.1016/j.resp.2013.10.007

29. Ware LB, Matthay MA. Acute Pulmonary Edema. *N Engl J Med*. 2005;353(26):2788-2796. doi:10.1056/NEJMcp052699

30. Kor DJ, Warner DO, Carter RE, et al. Extravascular Lung Water and Pulmonary Vascular Permeability Index as Markers Predictive of Postoperative Acute Respiratory Distress Syndrome: A Prospective Cohort Investigation*. *Critical Care Medicine*. 2015;43(3):665. doi:10.1097/CCM.0000000000000765

31. Berkowitz DM, Danai PA, Eaton S, Moss M, Martin GS. Accurate characterization of extravascular lung water in acute respiratory distress syndrome. *Crit Care Med*. 2008;36(6):1803-1809. doi:10.1097/CCM.0b013e3181743eeb

32. Martin GS, Eaton S, Mealer M, Moss M. Extravascular lung water in patients with severe sepsis: a prospective cohort study. *Crit Care*. 2005;9(2):R74-82. doi:10.1186/cc3025

33. Rasch S, Schmidle P, Sancak S, et al. Increased extravascular lung water index (EVLWI) reflects rapid non-cardiogenic oedema and mortality in COVID-19 associated ARDS. *Sci Rep*. 2021;11:11524. doi:10.1038/s41598-021-91043-3

34. Sibbald WJ, Cunningham DR, Chin DN. Non-Cardiac Or Cardiac Pulmonary Edema?: A Practical Approach to Clinical Differentiation in Critically III Patients. *Chest*. 1983;84(4):452-461. doi:10.1378/chest.84.4.452

35. Edoute Y, Roguin A, Behar D, Reisner SA. Prospective evaluation of pulmonary edema. *Crit Care Med*. 2000;28(2):330-335. doi:10.1097/00003246-200002000-00007

36. Sweeney RM, McAuley DF. Acute respiratory distress syndrome. *Lancet*. 2016;388(10058):2416-2430. doi:10.1016/S0140-6736(16)00578-X

37. Sarkar M, Madabhavi I, Niranjan N, Dogra M. Auscultation of the respiratory system. *Ann Thorac Med*. 2015;10(3):158-168. doi:10.4103/1817-1737.160831

38. Thoracic CT in detecting occult disease in critically ill patients. doi:10.2214/ajr.148.4.685

39. Saugel B, Holzapfel K, Stollfuss J, et al. Computed tomography to estimate cardiac preload and extravascular lung water. A retrospective analysis in critically ill patients. *Scand J Trauma Resusc Emerg Med*. 2011;19:31. doi:10.1186/1757-7241-19-31

40. Messerli M, Kluckert T, Knitel M, et al. Ultralow dose CT for pulmonary nodule detection with chest x-ray equivalent dose – a prospective intra-individual comparative study. *Eur Radiol*. 2017;27(8):3290-3299. doi:10.1007/s00330-017-4739-6

41. Picano E, Frassi F, Agricola E, Gligorova S, Gargani L, Mottola G. Ultrasound lung comets: a clinically useful sign of extravascular lung water. *J Am Soc Echocardiogr*. 2006;19(3):356-363. doi:10.1016/j.echo.2005.05.019

42. Dicker SA. Lung Ultrasound for Pulmonary Contusions. *Veterinary Clinics of North America: Small Animal Practice*. 2021;51(6):1141-1151. doi:10.1016/j.cvsm.2021.07.001

43. Tagami T, Kushimoto S, Yamamoto Y, et al. Validation of extravascular lung water measurement by single transpulmonary thermodilution: human autopsy study. *Crit Care*. 2010;14(5):R162. doi:10.1186/cc9250

44. Tagami T, Ong MEH. Extravascular lung water measurements in acute respiratory distress syndrome: why, how, and when? *Curr Opin Crit Care*. 2018;24(3):209-215. doi:10.1097/MCC.0000000000000503

45. Tran MP. 3D image analysis with variational methods and wavelets : applications to medical image processing. Published online September 28, 2012.

46. Fournier P, Mensch-Dechène J, Ranson-Bitker B, Valladares W, Lockhart A. Effects of sitting up on pulmonary blood pressure, flow, and volume in man. *J Appl Physiol Respir Environ Exerc Physiol*. 1979;46(1):36-40. doi:10.1152/jappl.1979.46.1.36

47. Coonan TJ, Hope CE. Cardio-respiratory effects of change of body position. *Can Anaesth Soc J*. 1983;30(4):424-437. doi:10.1007/BF03007869

48. Principles of Magnetic Resonance Imaging: A Signal Processing Perspective | IEEE eBooks | IEEE Xplore. Accessed August 17, 2023. https://ieeexplore.ieee.org/book/5264284

49. Wild JM, Marshall H, Bock M, et al. MRI of the lung (1/3): methods. *Insights Imaging*. 2012;3(4):345-353. doi:10.1007/s13244-012-0176-x

50. Pleil JD, Wallace MAG, Davis MD, Matty CM. The physics of human breathing: flow, timing, volume, and pressure parameters for normal, on-demand, and ventilator respiration. *J Breath Res*. 2021;15(4):10.1088/1752-7163/ac2589. doi:10.1088/1752-7163/ac2589

51. Pusey E, Yoon C, Anselmo ML, Lufkin RB. Aliasing artifacts in mr imaging. *Computerized Medical Imaging and Graphics*. 1988;12(4):219-224. doi:10.1016/0895-6111(86)90003-0

52. Vachha B, Huang SY. MRI with ultrahigh field strength and high-performance gradients: challenges and opportunities for clinical neuroimaging at 7 T and beyond. *Eur Radiol Exp*. 2021;5:35. doi:10.1186/s41747-021-00216-2

53. Pohmann R, Speck O, Scheffler K. Signal-to-noise ratio and MR tissue parameters in human brain imaging at 3, 7, and 9.4 tesla using current receive coil arrays. *Magnetic Resonance in Medicine*. 2016;75(2):801-809. doi:10.1002/mrm.25677

54. Hatabu H, Chen Q, Stock KW, Gefter WB, Itoh H. Fast magnetic resonance imaging of the lung. *European Journal of Radiology*. 1999;29(2):114-132. doi:10.1016/S0720-048X(98)00174-0

55. Chang S, Park J, Yang YJ, et al. Myocardial T2* Imaging at 3T and 1.5T: A Pilot Study with Phantom and Normal Myocardium. *J Cardiovasc Dev Dis*. 2022;9(8):271. doi:10.3390/jcdd9080271

56. Zaeske C, Brueggemann GP, Willwacher S, Maehlich D, Maintz D, Bratke G. The behaviour of T2* and T2 relaxation time in extrinsic foot muscles under continuous exercise: A prospective analysis during extended running. *PLoS One*. 2022;17(2):e0264066. doi:10.1371/journal.pone.0264066

57. Hargreaves B. Rapid Gradient-Echo Imaging. *J Magn Reson Imaging*. 2012;36(6):1300-1313. doi:10.1002/jmri.23742

58. Buxton RB, Edelman RR, Rosen BR, Wismer GL, Brady TJ. Contrast in Rapid MR Imaging: T1− and T2-Weighted Imaging. *Journal of Computer Assisted Tomography*. 1987;11(1):7.

59. Bruegel M, Gaa J, Woertler K, et al. MRI of the lung: Value of different turbo spin-echo, single-shot turbo spin-echo, and 3D gradient-echo pulse sequences for the detection of pulmonary metastases. *Journal of Magnetic Resonance Imaging*. 2007;25(1):73-81. doi:10.1002/jmri.20824

60. Leutner CC, Gieseke J, Lutterbey G, et al. MR Imaging of Pneumonia in Immunocompromised Patients. *American Journal of Roentgenology*. 2000;175(2):391-397. doi:10.2214/ajr.175.2.1750391

61. Patel MR, Klufas RA, Alberico RA, Edelman RR. Half-fourier acquisition single-shot turbo spin-echo (HASTE) MR: comparison with fast spin-echo MR in diseases of the brain. *AJNR Am J Neuroradiol*. 1997;18(9):1635-1640.

62. Pipe JG. Motion correction with PROPELLER MRI: Application to head motion and free-breathing cardiac imaging. *Magnetic Resonance in Medicine*. 1999;42(5):963-969. doi:10.1002/(SICI)1522-2594(199911)42:5<963::AID-MRM17>3.0.CO;2-L

63. Ferreira PF, Gatehouse PD, Mohiaddin RH, Firmin DN. Cardiovascular magnetic resonance artefacts. *J Cardiovasc Magn Reson*. 2013;15(1):41. doi:10.1186/1532-429X-15-41

64. Beatty PJ, Nishimura DG, Pauly JM. Rapid gridding reconstruction with a minimal oversampling ratio. *IEEE Trans Med Imaging*. 2005;24(6):799-808. doi:10.1109/TMI.2005.848376

65. Mezrich R. A perspective on K-space. *Radiology*. 1995;195(2):297-315. doi:10.1148/radiology.195.2.7724743

66. Themes UFO. MR Image Reconstruction. Radiology Key. Published October 7, 2018. Accessed October 16, 2023. https://radiologykey.com/mr-image-reconstruction/

67. Herrmann KH, Krämer M, Reichenbach JR. Time Efficient 3D Radial UTE Sampling with Fully Automatic Delay Compensation on a Clinical 3T MR Scanner. *PLoS One*. 2016;11(3):e0150371. doi:10.1371/journal.pone.0150371

68. Gibiino F, Sacolick L, Menini A, Landini L, Wiesinger F. Free-breathing, zero-TE MR lung imaging. *Magn Reson Mater Phy*. 2015;28(3):207-215. doi:10.1007/s10334-014-0459-y

69. Gurney PT, Hargreaves BA, Nishimura DG. Design and analysis of a practical 3D cones trajectory. *Magnetic Resonance in Medicine*. 2006;55(3):575-582. doi:10.1002/mrm.20796

70. Robson MD, Gatehouse PD, Bydder M, Bydder GM. Magnetic Resonance: An Introduction to Ultrashort TE (UTE) Imaging. *Journal of Computer Assisted Tomography*. 2003;27(6):825.

71. Glover PM. Interaction of MRI field gradients with the human body. *Phys Med Biol*. 2009;54(21):R99-R115. doi:10.1088/0031-9155/54/21/R01

72. Tibiletti M, Paul J, Bianchi A, et al. Multistage three-dimensional UTE lung imaging by image-based self-gating. *Magn Reson Med*. 2016;75(3):1324-1332. doi:10.1002/mrm.25673

73. Feng L. Golden-Angle Radial MRI: Basics, Advances, and Applications. *Journal of Magnetic Resonance Imaging*. 2022;56(1):45-62. doi:10.1002/jmri.28187

74. Beattie JR, Esmonde-White FWL. Exploration of Principal Component Analysis: Deriving Principal Component Analysis Visually Using Spectra. *Appl Spectrosc*. 2021;75(4):361-375. doi:10.1177/0003702820987847

75. Pipe JG, Menon P. Sampling density compensation in MRI: rationale and an iterative numerical solution. *Magn Reson Med*. 1999;41(1):179-186. doi:10.1002/(sici)1522-2594(199901)41:1<179::aid-mrm25>3.0.co;2-v

76. Pruessmann KP, Weiger M, Scheidegger MB, Boesiger P. SENSE: sensitivity encoding for fast MRI. *Magn Reson Med*. 1999;42(5):952-962.

77. Bydder M, Larkman DJ, Hajnal JV. Combination of signals from array coils using image-based estimation of coil sensitivity profiles. *Magn Reson Med*. 2002;47(3):539-548. doi:10.1002/mrm.10092

78. Roemer PB, Edelstein WA, Hayes CE, Souza SP, Mueller OM. The NMR phased array. *Magnetic Resonance in Medicine*. 1990;16(2):192-225. doi:10.1002/mrm.1910160203

79. Forbes RM, Cooper AR, Mitchell HH. The composition of the adult human body as determined by chemical analysis. *J Biol Chem*. 1953;203(1):359-366.

80. Ward SR, Lieber RL. Density and hydration of fresh and fixed human skeletal muscle. *J Biomech*. 2005;38(11):2317-2320. doi:10.1016/j.jbiomech.2004.10.001

81. Bhave G, Neilson EG. Body fluid dynamics: back to the future. *J Am Soc Nephrol*. 2011;22(12):2166-2181. doi:10.1681/ASN.2011080865

82. Surface Fitting using gridfit. Published October 24, 2023. Accessed October 24, 2023. https://www.mathworks.com/matlabcentral/fileexchange/8998-surface-fitting-using-gridfit

83. Solutions of Ill-Posed Problems (A. N. Tikhonov and V. Y. Arsenin). doi:10.1137/1021044

84. The Use of the L-Curve in the Regularization of Discrete Ill-Posed Problems. doi:10.1137/0914086

85. Isensee F, Jaeger PF, Kohl SAA, Petersen J, Maier-Hein KH. nnU-Net: a self-configuring method for deep learning-based biomedical image segmentation. *Nat Methods*. 2021;18(2):203-211. doi:10.1038/s41592-020-01008-z

86. Satpute N, Gómez-Luna J, Olivares J. Accelerating Chan–Vese model with cross-modality guided contrast enhancement for liver segmentation. *Computers in Biology and Medicine*. 2020;124:103930. doi:10.1016/j.compbiomed.2020.103930

87. Keen C, Seres P, Grenier J, et al. Deep Learning Segmentation of Lung Parenchyma for UTE Proton MRI. In: *Proceedings of the International Society for Magnetic Resonance in Medicine*. ; :Abstract 4897.

88. Kellman P, McVeigh ER. Image Reconstruction in SNR Units: A General Method for SNR Measurement. *Magn Reson Med*. 2005;54(6):1439-1447. doi:10.1002/mrm.20713

89. Zafar W, Masood A, Iqbal B, Murad S. Resolution, SNR, signal averaging and scan time in mri formetastatic lesion in spine. A case report.

90. Krupa K, Bekiesińska-Figatowska M. Artifacts in Magnetic Resonance Imaging. *Pol J Radiol*. 2015;80:93-106. doi:10.12659/PJR.892628

91. Meadus WQ, Stobbe RW, Grenier JG, Beaulieu C, Thompson RB. Quantification of lung water density with UTE Yarnball MRI. *Magnetic Resonance in Medicine*. 2021;86(3):1330-1344. doi:10.1002/mrm.28800

92. Goner O, Thron H. Postural Changes in the Circulation. In: *Handbook of Physiology*. Vol 3. Hamiton WF, Dew P, American Physiological Society; 1965:Ch. 67, 2409-2439.

93. Almquist HM, Palmer J, Jonson B, Wollmer P. Pulmonary Perfusion and Density Gradients in Healthy Volunteers. *Journal of Nuclear Medicine*. 1997;38(6):962-966.

94. Millar AB, Denison DM. Vertical gradients of lung density in healthy supine men. *Thorax*. 1989;44(6):485-490. doi:10.1136/thx.44.6.485

95. Theilmann RJ, Arai TJ, Samiee A, et al. Quantitative MRI measurement of lung density must account for the change in T(2) (*) with lung inflation. *J Magn Reson Imaging*. 2009;30(3):527-534. doi:10.1002/jmri.21866

96. Tawhai MH, Nash MP, Lin CL, Hoffman EA. Supine and prone differences in regional lung density and pleural pressure gradients in the human lung with constant shape. *J Appl Physiol (1985)*. 2009;107(3):912-920. doi:10.1152/japplphysiol.00324.2009

97. Mayo JR, MacKay AL, Whittall KP, Baile EM, Paré PD. Measurement of lung water content and pleural pressure gradient with magnetic resonance imaging. *J Thorac Imaging*. 1995;10(1):73-81. doi:10.1097/00005382-199501010-00007

98. Dean E. Effect of body position on pulmonary function. *Phys Ther*. 1985;65(5):613-618. doi:10.1093/ptj/65.5.613

99. Castile R, Mead J, Jackson A, Wohl ME, Stokes D. Effects of posture on flow-volume curve configuration in normal humans. *J Appl Physiol Respir Environ Exerc Physiol*. 1982;53(5):1175-1183. doi:10.1152/jappl.1982.53.5.1175

100. Lumb AB, Nunn JF. Respiratory function and ribcage contribution to ventilation in body positions commonly used during anesthesia. *Anesth Analg*. 1991;73(4):422-426. doi:10.1213/00000539-199110000-00010

101. Bankier AA, O'Donnell CR, Mai VM, et al. Impact of lung volume on MR signal intensity changes of the lung parenchyma. *J Magn Reson Imaging*. 2004;20(6):961-966. doi:10.1002/jmri.20198

102. Lijnema TH, Huizenga JR, Jager J, Mackor AJ, Gips CH. Gravimetric determination of the water concentration in whole blood, plasma and erythrocytes and correlations with hematological and clinicochemical parameters. *Clin Chim Acta*. 1993;214(2):129-138. doi:10.1016/0009-8981(93)90105-d

103. McKnight CL, Burns B. Pneumothorax. In: *StatPearls*. StatPearls Publishing; 2023. Accessed November 25, 2023. http://www.ncbi.nlm.nih.gov/books/NBK441885/

104. Torres A, Cilloniz C, Niederman MS, et al. Pneumonia. *Nat Rev Dis Primers*. 2021;7(1):1-28. doi:10.1038/s41572-021-00259-0

105. Hashmi MF, Tariq M, Cataletto ME. Asthma. In: *StatPearls*. StatPearls Publishing; 2023. Accessed November 25, 2023. http://www.ncbi.nlm.nih.gov/books/NBK430901/

106. Seemann F, Javed A, Khan JM, et al. Dynamic lung water MRI during exercise stress. *Magnetic Resonance in Medicine*. 2023;90(4):1396-1413. doi:10.1002/mrm.29716